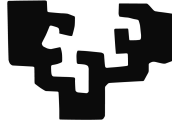eman ta zabal zazu

Universidad del País Vasco   Euskal Herriko Unibertsitatea

Hydrogen and lithium under high pressure

Superconductivity and other emerging properties

Miguel Borinaga Treviño

Supervised by Aitor Bergara and Ion Errea

Donostia/San Sebastián, July 2018

Contents

Introduction

Hydrogen, consisting of just a proton and an electron, is the simplest and most abundant element in the Universe. It is well known at ambient conditions, where it forms a diatomic molecule. Lithium, with only three protons, is the lightest metal in the periodic table. It is indeed a good representative of metals, since its normal condition properties can be explained with the free-electron model thanks to its almost perfectly spherical Fermi surface. These two elements are deeply understood at the pressure (P) and temperatures (Ts) we usually find on the surface of the Earth. However, they still capture the attention of the scientific community, as they display extraordinary properties once they are brought under extreme conditions.

The physical changes pressure and temperature promote in matter can be seen in everyday life. Water, for example, transforms to vapor when heated to 100 ºC at fixed ambient pressure. However, one can also convert water into vapor by reducing pressure at a fixed lower temperature. Similarly, water transforms to solid ice when cooled to temperatures below 0 ºC or at pressures higher than roughly 10.000 atm. These phase transitions obey the general intuition considering they are a consequence of minimizing the so-called Gibbs free energy

$$G = E - TS + PV, \tag{1}$$

where E is the internal energy (or just the energy, for simplicity), S is the entropy and V is the volume of the piece of matter. According to Eq. (1), compact and ordered phases (solids) are favored at low temperatures and/or at high pressures, while less dense and disordered structures (gases) will be favored at opposite conditions. Liquids will be favored at intermediate regimes.

When the TS and PV terms of the Gibbs free energy are comparable to chemical bonding energies, temperature and pressure can induce chemical and structural changes which may lead to physical properties not expected *a priori*. In the solid state, while some famous and extraordinary temperature induced transformations occur, like the martensitic transition of lithium [1], pressure is usually a more powerful tool for tuning the crystal structure and, as a consequence, the properties of materials. This is because pressure alters the energy of atomic bonds by forcing atoms closer together in a smaller volume.

One of the physical properties showing exceptional changes associated to pressure is superconductivity. According to simple electronic and vibrational theories like Hartree-Fock and the quasi-harmonic approximation, electron-phonon coupling mediated superconductors are expected to reduce their superconducting critical temperature (T_c) as the applied pressure is increased [2, 3]. While this is true for most simple conventional superconductors [4, 5], some elements have their T_cs increased by orders of magnitude under compression. Lithium is in fact a

great example as, while at ambient pressure it superconducts below 0.4 mK [6], T_c escalates to almost 20 K at 48 GPa [7–12], an astonishing enhancement of five orders of magnitude. This phenomenon is even more striking when a material is not a superconductor (in some cases neither a metal) at ambient pressure but becomes a superconductor after being squeezed to high pressure. Just considering single-element materials, pressure raises the total number of superconducting elements from 29 at ambient pressure to 52, including non-metallic elements like sulfur or oxygen [13]. Actually, even though it has not been experimentally confirmed yet, this is expected for hydrogen as well. Metallization of hydrogen under pressure was predicted by Wigner and Huntington in 1935 [14] and later Ashcroft predicted it would be an extremely high temperature superconductor [15]. The measurement of a record T_c of 203 K after compressing hydrogen sulfide to 150 GPa [16] suggests Ashcroft's prediction may be on-track.

Superconductivity is not the only counter-intuitive or unexpected phenomenon emerging under compression in single-element materials. While the PV term of the Gibbs free energy favors compact structures at high pressure, some materials display the opposite behavior [17–22]. Lithium, along with other alkali metals, is one of the elements showing this behavior. Associated to their rich phase-transition sequence, they show metal-insulator transitions [23, 24] and low temperature melting [25, 26]. Some of the structural transitions are induced by phonon instabilities, which are caused by the deviation of the Fermi surface from the free-electron sphere to more complex shapes. The loop closes back to superconductivity as these phonon softenings often enhance the electron-phonon coupling and, consequently, drive the increase of T_c [27–33].

Pressure covers probably the greatest range of orders of magnitude of all physical magnitudes. From the almost perfect vacuum of outer space to the enormous atomic-nuclei-like density of neutron stars there are sixty orders of magnitude. To put it in numbers, any object in the Mariana trench in the Pacific Ocean, the deepest point on Earth, is subject to a pressure of about 0.1 GPa (roughly 1,000 atm). Pressure at the center of the Earth exceeds 300 gigapascal (GPa), with large gaseous planets as Saturn and Jupiter reaching estimated pressures of several terapascal. At the not ultimate but quite upper part of the range, the pressure inside of the Sun is expected to be around 26 petapascal. In the context of materials research, as it is the case of the examples given in the previous paragraphs, "high pressure" commonly refers to pressures in the range of thousands to millions atmospheres. The common unit of choice in the field and in this thesis is the GPa, which is approximately 10000 times larger than the atmospheric pressure.

In order to study materials at pressures up to hundreds of GPa experimentalists confine the samples in specially designed machines that apply a force to the small
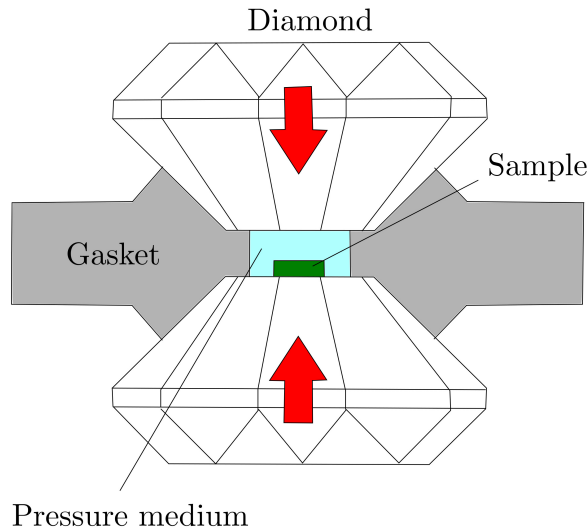
Figure 1: Schematic sketch of a diamond anvil cell. The red arrows indicate the direction in which the force is applied.

sample area. Laser shock-wave experiments are able to reach the terapascal regime for a limited short time, but with accordingly high temperatures of hundreds or thousands of Kelvins. When low temperature material properties, as superconductivity, need to be probed static experiments are required, for which the diamond anvil cell (DAC) is the most commonly used device. In the DAC two gem-quality diamonds apply a force to a metallic gasket in such a way that the sample chamber is defined by the cylindrical gasket wall and the flat diamond ends (see Fig. 1). For solid samples a non-reactive pressure transmitting fluid is usually introduced to guarantee the pressure acting on the sample is isotropic. State of the art DACs are able to reach pressures up to 600 GPa [34], but experiments at these extreme pressures are extremely challenging. Even though the employed high-quality diamonds show very few impurities, they make diamonds vulnerable to breaking and losing their broad spectrum transparency, which is vital for analyzing the samples.

The technical difficulty and high economical cost of high pressure experiments make theoretical approaches specially necessary. Fortunately, in the framework of density functional theory (DFT), the theory of choice in this thesis, dealing with pressure is quite straightforward, since the unit-cell volume can be chosen on demand. Pressure can be determined either by calculating the stress tensor of the system via the Hellmann-Feynman theorem from a ground-state energy calculation, or by calculating the total energy of the system for several volumes

and fitting an equation of state. Combination of theory with experiments has led to fast advances in the high-pressure science field [35–37], with theory being able to make predictions as important as the high superconducting T_c of hydrogen sulfide at high pressures [38, 39].

In this thesis we present a first-principles analysis of the electronic, vibrational and superconducting properties of solid hydrogen and lithium under high pressure based on DFT. This thesis consists of three distinct parts. In part I, we summarize the theoretical framework used to perform the calculations. Solid hydrogen is exhaustively analyzed around its expected metallization pressure of 400-600 GPa in part II. Part III is devoted to the analysis of the high pressure superconducting behavior of lithium, motivated by the recent measurement of an inverse isotope effect in its superconductivity [9].

Part I

Theoretical background

Chapter 1

The adiabatic Born-Oppenheimer approximation

Matter can be described as a set of electrons and nuclei interacting via the Coulomb inverse square law. Matter can form a plasma, where the charged particles move so fast that they are not able to bond. It can appear in gaseous state, where electrons bond to nuclei and form atoms which may be alone or joint into molecules. It can also condense and form both disordered, as liquids and amorphous solids, and ordered materials as crystalline solids, surfaces, etc. Whatever the case, the proper framework to describe a piece of matter is quantum mechanics and, in the absence of external potentials acting on the system under analysis, the problem reduces to solving the time-independent Schrödinger equation

$$H \left| \Psi_A \right\rangle = E_A \left| \Psi_A \right\rangle, \tag{1.1}$$

where E_A is an eigenvalue with quantum number A and

$$\langle \mathbf{r} | \Psi_A \rangle = \Psi_A(\mathbf{r}_1, ..., \mathbf{r}_N, \mathbf{R}_1, ..., \mathbf{R}_M) = \Psi_A(\mathbf{r}, \mathbf{R}) \tag{1.2}$$

its corresponding eigenfunction of the quantum mechanical system consisting of N electrons at positions $\mathbf{r} \equiv \mathbf{r}_1, ..., \mathbf{r}_N$ and M nuclei of atomic number Z_j at $\mathbf{R} \equiv \mathbf{R}_1, ..., \mathbf{R}_M$. The Hamiltonian that governs this equation is, for the non-relativistic case[1],

$$H = \frac{1}{2} \sum_{i}^{N} \mathbf{p}_i^2 + \frac{1}{2} \sum_{j}^{M} \frac{\mathbf{P}_j^2}{m_j} - \sum_{i}^{N} \sum_{j}^{M} \frac{Z_j}{|\mathbf{r}_i - \mathbf{R}_j|} + \frac{1}{2} \sum_{i \neq j}^{N} \frac{1}{|\mathbf{r}_i - \mathbf{r}_j|}$$

$$+ \frac{1}{2} \sum_{i \neq j}^{M} \frac{1}{|\mathbf{R}_i - \mathbf{R}_j|} = T_e + T_I + V_{e,I} + V_{e,e} + V_{I,I}, \tag{1.3}$$

---

[1]Here and on, we will use atomic units ($\hbar = e = m_e = 1$)

where $\mathbf{p}_i$ and $\mathbf{P}_j$ are electronic and nuclear momentum operators and m_j is the nuclear mass. T_e and T_I are the electronic and nuclear kinetic energy operators, respectively, and $V_{e,I}$, $V_{e,e}$ and $V_{I,I}$ account for electron-nuclei, electron-electron and nuclei-nuclei Coulomb interactions.

As we can see, we are dealing with a system of $3(N + M)$ degrees of freedom where the Coulombic terms make impossible to separate the many-body Hamiltonian into single-particle ones. Due to such complexity an analytical solution for macroscopic systems ($N, M \sim 10^{23}$) is impossible. However, the eigenfunctions $\Psi_A(\mathbf{r}, \mathbf{R})$ contain all the relevant information of the material, including the positions of the nuclei and, therefore, its structure. Interestingly, from these equations one can deduce that every property of a material is a consequence of the fairly simple Coulomb pair potential and the quantum many body character of matter.

The mathematical complexity of the problem makes the use of approximations imperative right from the beginning. Due to the huge difference of masses between nuclei and electrons ($m_j \sim 10^3$), the latter move much faster than the nuclei[2]. In the Born-Oppenheimer Approximation (BOA) electrons are assumed to adapt instantaneously to the nuclear position changes. As we will see, this will allow us to treat the electrons and nuclei as separate quantum mechanical systems.

Let us assume the total Hamiltonian is separable into electronic (H^e) and nuclear (H^I) parts. As we consider nuclei frozen from the electronic point of view, we first get rid of nuclear degrees of freedom in the electronic problem. Thus, we can solve the electronic problem by building H^e only with the terms from the total Hamiltonian that depend on electronic degrees of freedom

$$H^e(\mathbf{R}) = T_e + V_{e,I}(\mathbf{R}) + V_{e,e} + V_{I,I}(\mathbf{R}), \qquad (1.4)$$

where we include the nuclei-nuclei term as it reduces to a constant and the $\mathbf{R}$ dependence is parametric. We assume the following eigenvalue problem holds:

$$H^e |\psi_\alpha^e\rangle = E_\alpha^e |\psi_\alpha^e\rangle, \qquad (1.5)$$

where α is a quantum number which fully describes the electronic system. Now, the electronic eigenvalues E_α^e and eigenfunctions

$$\langle \mathbf{r}|\psi_\alpha^e\rangle = \psi_\alpha^e(\mathbf{r}; \mathbf{R}) \qquad (1.6)$$

depend on the nuclear positions only parametrically.

---

[2]Classical theory of harmonic crystals predicts velocities of 10^8cm/s and 10^5cm/s for electrons and nuclei, respectively.

Since the electronic eigenfunctions form a complete set in $\mathbf{r}$ space, we can always write any state of the total system as a linear combination of vectorial products expanded only in the electronic degrees of freedom[3]:

$$|\Psi_{\alpha\beta}\rangle = \sum_{\alpha'} C_{\alpha'\alpha\beta} |\psi^I_{\alpha'\beta}\rangle \otimes |\psi^e_{\alpha'}\rangle, \qquad (1.7)$$

where $C_{\alpha'\alpha\beta}$ is a complex tensor and $|\psi^I_{\alpha\beta}\rangle$ are eigenstates of the still unknown H^I. If we project Eq. (1.7) with $\langle\mathbf{r}|$ from the left we can see that the total wavefunction is an expansion of products of nuclear and electronic counterparts:

$$\Psi_{\alpha\beta}(\mathbf{r}, \mathbf{R}) = \sum_{\alpha'} C_{\alpha'\alpha\beta} \psi^I_{\alpha'\beta}(\mathbf{R}) \psi^e_{\alpha'}(\mathbf{r}; \mathbf{R}). \qquad (1.8)$$

The α index of the nuclear eigenstates points out that nuclear states still depend on electronic degrees of freedom. For determining H^I, we plug $|\Psi_{\alpha\beta}\rangle$ in the Schrödinger equation (Eq. (1.1)) and project it on $\langle\psi^e_{\alpha'}|$:

$$\langle\psi^e_{\alpha'}|H|\Psi_{\alpha\beta}\rangle = E_{\alpha\beta} \langle\psi^e_{\alpha'}|\Psi_{\alpha\beta}\rangle. \qquad (1.9)$$

By plugging Eq. (1.7) in Eq. (1.9) it is straightforward to obtain

$$C_{\alpha'\alpha\beta}E^e_{\alpha'} |\psi^I_{\alpha'\beta}\rangle + \sum_{\alpha''} C_{\alpha''\alpha\beta} \langle\psi^e_{\alpha'}| T_I \left[|\psi^e_{\alpha''}\rangle \otimes |\psi^I_{\alpha''\beta}\rangle\right] = C_{\alpha\alpha\beta}E_{\alpha\beta} |\psi^I_{\alpha\beta}\rangle, \quad (1.10)$$

where[4]

$$T_I = \sum_j \frac{\mathbf{P}^2_j}{2m_j} = \sum_j \frac{1}{2m_j}[\mathbf{P}^2_j]_I + \sum_j \frac{1}{2m_j} \left(2 [\mathbf{P}_j]_I[\mathbf{P}_j]_e + [\mathbf{P}^2_j]_e\right) = [T_I]_I + \Delta H. \qquad (1.11)$$

So far, everything is exact. In the adiabatic approximation we assume no electronic excitations are created due to nuclear motion, so we only consider $\alpha' = \alpha$ and neglect ΔH. This way Eq.(1.10) is simplified and we end up with a Schrödinger equation for the nuclei

$$H^I |\psi^I_{\alpha\beta}\rangle = E_{\alpha\beta} |\psi^I_{\alpha\beta}\rangle, \qquad (1.12)$$

where

$$H^I \equiv H^I_\alpha = [T_I]_I + E^e_\alpha. \qquad (1.13)$$

---

[3]From now on, α and β (and their primed versions) will be quantum numbers that account for electronic and nuclear degrees of freedom, respectively. Combined, they will fully define any $A = \alpha\beta$ state of the total system.

[4]Writing operators as $[O]_I$ and $[O]_e$ indicates they act exclusively on $|\psi^e\rangle$ and $|\psi^I\rangle$ states, respectively.

This means nuclei move in effective potential energy surfaces $U_\alpha(\mathbf{R}) = E^e_\alpha(\mathbf{R})$ with α reminding us this surface can in principle be different for different electronic eigenstates. For most crystals at normal and low temperatures, which is the case throughout this thesis, α can be dropped from the nuclear problem and just consider the electronic ground state $E^e(\mathbf{R}) \equiv E^e_0(\mathbf{R})$, successfully splitting the electronic and nuclear problems. Ionic eigenstates not depending on electronic degrees of freedom anymore, we can write any eigenstate of the Born-Oppenheimer Hamiltonian $(H_{BO} = H^e + H^I)$ as a tensorial product of individual electronic and nuclear eigenstates:

$$|\Psi_{\alpha\beta}\rangle = |\psi^e_\alpha\rangle \otimes |\psi^I_\beta\rangle \equiv |\alpha, \beta\rangle . \tag{1.14}$$

In this basis, of course, H_{BO} is diagonal

$$\langle \alpha', \beta' | H_{BO} | \alpha, \beta \rangle = E_{\alpha\beta} \delta_{\alpha,\alpha'} \delta_{\beta,\beta'}. \tag{1.15}$$

The BOA is an excellent approximation for understanding and predicting many properties of diverse materials by analyzing their electronic structure and lattice vibrations (phonons), e.g., when we calculate the sound velocity, heat capacity or the stable geometry of a crystal. However, the assumption of nuclear kinetic energy not affecting electronic states is not always valid and even some basic properties are a consequence of non-diagonal elements in the Hamiltonian arising from the previously neglected ΔH term (i.e. the electrical resistivity in metals is a straightforward example). Still, even when this approach does not fully hold and one needs to go beyond, the picture of electrons and phonons being almost separate systems remains in most cases and, as we will see in Chapter 4, their coupling is commonly treated as a perturbation.

Chapter 2

The electronic problem

Once successfully separated the electronic and nuclear degrees of freedom, we will start solving the electronic problem, which still constitutes a challenge as $V_{e,e}$ (the electron-electron interaction term of the electronic Hamiltonian) couples the equations via the two-body $\frac{1}{|\mathbf{r}_i - \mathbf{r}_j|}$ operator. Actually, the way one deals with that operator makes the distinction from a solving method to another.

2.1 Independent electron approximation

If one neglects $V_{e,e}$ and, thus, adopts the so-called independent electron approximation, the system now is formed by N noninteracting electrons under an external potential

$$V_{ext}(\mathbf{x}) = \sum_j^M \frac{Z_j}{|\mathbf{x} - \mathbf{R}_j|}, \tag{2.1}$$

where $\mathbf{x}$ denotes any electronic position. Since the Hamiltonian is now separable, $H^e(\mathbf{r}) = \sum_i T_e(\mathbf{r}_i) + V_{ext}(\mathbf{r}_i)$, single electron states $|\phi_{\alpha_i}\rangle$ would be obtained from

$$\left(-\frac{\nabla^2}{2} + V_{ext} \right) |\phi_{\alpha_i}\rangle = \varepsilon_{\alpha_i} |\phi_{\alpha_i}\rangle \,, \tag{2.2}$$

with all the electrons having an identical set of eigenfunctions $\langle \mathbf{x}|\phi_{\alpha_i}\rangle = \phi_{\alpha_i}(\mathbf{x})$ and eigenvalues ε_{α_i}. Any total electronic wavefunction of such hypothetical system

could be given by a Slater determinant [40]:

$$
\psi_\alpha^e(\mathbf{r}) = \frac{1}{\sqrt{N!}}
\begin{vmatrix}
\phi_{\alpha_1}(\mathbf{r}_1) & \phi_{\alpha_1}(\mathbf{r}_2) & ... & \phi_{\alpha_1}(\mathbf{r}_N) \\
\phi_{\alpha_2}(\mathbf{r}_1) & \phi_{\alpha_2}(\mathbf{r}_2) & ... & \phi_{\alpha_2}(\mathbf{r}_N) \\
. & . & ... & . \\
. & . & ... & . \\
\phi_{\alpha_N}(\mathbf{r}_1) & \phi_{\alpha_N}(\mathbf{r}_2) & ... & \phi_{\alpha_N}(\mathbf{r}_N)
\end{vmatrix},
\tag{2.3}
$$

with $\alpha \equiv \alpha_1, \alpha_2...\alpha_N$ and $\langle \mathbf{r}_j | \phi_{\alpha_i} \rangle = \phi_{\alpha_i}(\mathbf{r}_j)$ being the single-electron wavefunction of jth electron at the α_i^{th} state.

One can think that neglecting the electron-electron interaction is quite a rough approach, which is true indeed; many properties of materials are precisely a consequence of such interaction. However, solving a single-body problem is substantially easier than a many-body one. Therefore, different mean field theories have been developed to turn the many-body electron-electron pair-potential into a single-body operator that acts as an external potential as the electron-nuclei interaction does. The theory of our choice will be density functional theory (DFT).

2.2   Density functional theory

Density functional theory is a mean field theory formulated in the 60's by Kohn, Hohenberg and Sham [41, 42]. In spite of being nowadays highly popular and successful in solid state physics as well as in molecular chemistry, the lack of computational power at the time it was developed made Kohn wait for more than 30 years to obtain the Nobel Prize.

As the name of the theory may suggest, the main ingredient of this formalism is the electronic density:

$$
n_\alpha(\mathbf{x}) = \langle \psi_\alpha^e | n(\mathbf{x}) | \psi_\alpha^e \rangle = \langle \psi_\alpha^e | \sum_i^N \delta(\mathbf{x} - \mathbf{r}_i) | \psi_\alpha^e \rangle =
$$
$$
= N \int (...) \int d\mathbf{r}_2...d\mathbf{r}_N \psi_\alpha^{e*}(\mathbf{x}, \mathbf{r}_2, ..., \mathbf{r}_N) \psi_\alpha^e(\mathbf{x}, \mathbf{r}_2, ..., \mathbf{r}_N).
\tag{2.4}
$$

DFT is composed by two theorems; the first theorem establishes a one to one relationship between the ground state density ($\alpha = 0$) and the Hamiltonian which governs a system of electrons; the second states the total energy of the system can be written as a functional of the density ($E[n_\alpha]$) for any external potential $V_{ext}(\mathbf{x})$, where the exact ground state energy is the global minimum of this functional, and

the density that minimizes it is the exact ground state density $n_0(\mathbf{x})$. Bringing it to our case, we see that the mentioned external potential is the electron-nuclei interaction:

$$V_{ext}(\mathbf{x}) = \sum_j^M \frac{Z_j}{|\mathbf{x} - \mathbf{R}_j|} = \sum_j^M v_{ext}(\mathbf{x} - \mathbf{R}_j). \tag{2.5}$$

In order to implement DFT to a system, Kohn and Sham proposed a new way of interpreting an electronic system. Instead of solving the actual interacting electronic system, they replaced it with another non-interacting one that would have exactly the same ground state density. The Hamiltonian of the non-interacting electronic system is now separable:

$$H^e(\mathbf{r}) = \sum_i^N \left[-\frac{1}{2} \nabla_{\mathbf{r}_i}^2 + V^{KS}(\mathbf{r}_i) \right] = \sum_i^N H^{KS}(\mathbf{r}_i), \tag{2.6}$$

where the Kohn-Sham one-electron states $|\phi_{\alpha_i}\rangle$ (Kohn-Sham states) fulfill

$$H^{KS} |\phi_{\alpha_i}\rangle = \varepsilon_{\alpha_i} |\phi_{\alpha_i}\rangle. \tag{2.7}$$

and the total Kohn-Sham state of this non-interacting system $|\psi_\alpha^{KS}\rangle$ is built with a single Slater determinant exactly as in Eq. (2.3). This way, the density can be written in terms of the single-particle wavefunctions as

$$n_\alpha(\mathbf{x}) = \sum_i^N |\phi_{\alpha_i}(\mathbf{x})|^2. \tag{2.8}$$

Eq. 2.6 is equivalent to Eq. (2.2) in the independent electron approximation, except for in this case the effective Hamiltonian H^{KS} does include the electron-electron interaction contribution. However, we do not know the functional form of V^{KS} yet.

The electronic energy functional can be written as

$$E^e[n_\alpha] = T_e[n_\alpha] + E_{e,e}[n_\alpha] + E_{ext}[n_\alpha], \tag{2.9}$$

with the electron-nuclei interaction energy adopting the following form:

$$E_{ext}[n_\alpha] = \int d\mathbf{x} \ n_\alpha(\mathbf{x}) V_{ext}(\mathbf{x}). \tag{2.10}$$

The terms $T_e[n_\alpha]$ and $E_{e,e}[n_\alpha]$ cannot be expressed in such a straightforward form as $E_{ext}[n_\alpha]$. Thus, it is useful to write the non-interacting kinetic energy, $T_e^{KS}[n_\alpha]$,

by evaluating the electronic kinetic energy operator with $|\psi_\alpha^{KS}\rangle$

$$
\begin{aligned}
T_e^{KS}[n_\alpha] &= \langle \psi_\alpha^{KS}| \, T_e \, |\psi_\alpha^{KS}\rangle = \\
&= -\frac{1}{2}\sum_i^N \langle \phi_{\alpha_i}| \, \nabla^2 \, |\phi_{\alpha_i}\rangle = -\frac{1}{2}\sum_i^N \int d\mathbf{x} \; \phi_{\alpha_i}^*(\mathbf{x})\nabla^2\phi_{\alpha_i}(\mathbf{x}).
\end{aligned} \quad (2.11)
$$

Note the density dependence of $T_e^{KS}[n_\alpha]$ is implicit, as it comes from the density dependence of the single-electron wavefunctions $\phi_{\alpha_i}(\mathbf{x})$. Additionally, it is important to point out $T_e^{KS}[n_\alpha]$ accounts for most but not all the kinetic energy of the electrons and it is consequently different from $T_e[n_\alpha]$. As $|\psi_\alpha^{KS}\rangle$ is built by vectorial products of independent single-particle states $|\phi_{\alpha_i}\rangle$ with the momentum operator $\mathbf{p}_i$ acting only in its corresponding electronic state, $T_e^{KS}[n_\alpha] = T_e[n_\alpha] - T_c[n_\alpha]$ lacks of the electronic correlation component of the kinetic energy $T_c[n_\alpha]$, which precisely considers how the motion of one electron affects the motion of another. For dealing with $E_{e,e}[n_\alpha]$ we proceed in the same way and write the non-interacting electron-electron interaction energy functional

$$
E_{e,e}^{KS}[n_\alpha] = \langle \psi_\alpha^{KS}| \, E_{e,e} \, |\psi_\alpha^{KS}\rangle = E_H[n_\alpha] + E_X[n_\alpha] \qquad (2.12)
$$

where

$$
E_H[n_\alpha] = \frac{1}{2}\iint d\mathbf{x} \; d\mathbf{x}' \; \frac{n_\alpha(\mathbf{x})n_\alpha(\mathbf{x}')}{|\mathbf{x}-\mathbf{x}'|} \qquad (2.13)
$$

is the Hartree energy which corresponds to an electronic density interacting with itself and

$$
E_X[n_\alpha] = -\frac{1}{2}\sum_{i,j}\iint d\mathbf{x} \; d\mathbf{x}' \; \frac{\phi_{\alpha_i}^*(\mathbf{x})\phi_{\alpha_i}(\mathbf{x}')\phi_{\alpha_j}^*(\mathbf{x}')\phi_{\alpha_j}(\mathbf{x})}{|\mathbf{x}-\mathbf{x}'|} \qquad (2.14)
$$

is the electronic exchange energy which accounts for the antisymmetric nature of the wavefunction with respect to the exchange of any two particles' coordinates and the quantized nature of electrons, meaning it corrects the self-interaction of each electron wrongly included in $E_H[n_\alpha]$. However, as it happened for the kinetic energy, $E_{e,e}^{KS}[n_\alpha] = E_{e,e}[n_\alpha] - E_{e,e,C}[n_\alpha]$ lacks of the correlation contribution $E_{e,e,C}[n_\alpha]$ to the electron-electron interaction energy.

We shall rewrite the total energy functional as

$$
E^e[n_\alpha] = T_e^{KS}[n_\alpha] + E_{ext}[n_\alpha] + E_H[n_\alpha] + E_X[n_\alpha] + T_C[n_\alpha] + E_{e,e,C}[n_\alpha]. \qquad (2.15)
$$

Correlation properties are purely many-body properties and can only be calculated exactly by solving the many-body Schrödinger equation, i.e. by quantum Monte Carlo methods [43]. In mean-field theories as in DFT $T_C[n_\alpha]$ and $E_{e,e,C}[n_\alpha]$ are

always approximated to some degree. Besides, while easily accessible in principle, $E_X[n_\alpha]$ is considerably more expensive to evaluate computationally than $T_e^{KS}[n_\alpha]$, $E_{e,I}[n_\alpha]$ and $E_H[n_\alpha]$. Thus, it is common to approximate the exchange energy as well, leading to the usual grouping together of the exchange and correlation energies into the exchange-correlation energy $E_{xc}[n_\alpha]$. Thus, our final energy functional has the form

$$E^e[n_\alpha] = T_e^{KS}[n_\alpha] + E_{ext}[n_\alpha] + E_H[n_\alpha] + E_{xc}[n_\alpha]. \tag{2.16}$$

We minimize the energy with respect to $\phi_{\alpha_i}^*(\mathbf{x})$ using the variational method:

$$\frac{\delta}{\delta\phi_{\alpha_i}^*(\mathbf{x})} \left(E^e[n_\alpha] - \sum_j \varepsilon_j (\int d\mathbf{x}\ \phi_{\alpha_j}^*(\mathbf{x})\phi_{\alpha_j}(\mathbf{x}) - 1) \right) = 0, \tag{2.17}$$

where ε_j are Lagrange multipliers related to the normalization condition of the single-particle wave functions. Using Eq. (2.8) it is straightforward to obtain

$$-\frac{1}{2}\nabla^2\phi_{\alpha_i}(\mathbf{x}) + \left(\frac{\delta E_{ext}[n_\alpha]}{\delta n_\alpha(\mathbf{x})} + \frac{\delta E_H[n_\alpha]}{\delta n_\alpha(\mathbf{x})} + \frac{\delta E_{xc}[n_\alpha]}{\delta n_\alpha(\mathbf{x})} \right) \phi_{\alpha_i}(\mathbf{x}) = \varepsilon_i\phi_{\alpha_i}(\mathbf{x}). \tag{2.18}$$

As we know from the second Hohenberg and Kohn theorem, the density that minimizes the energy functional is the exact ground state energy. Since electrons are fermions, the ground-state density is calculated filling the electronic states of energy ε by following the zero temperature Fermi-Dirac distribution $2[\theta(\varepsilon_F - \varepsilon)]$, where the factor of 2 accounts for spin-degeneracy and ε_F is the Fermi energy of the system, which indicates the highest energy occupied electronic state in a metal[1]. Thus, the ground-state density reads

$$n_0(\mathbf{x}) = \sum_{i=0}^{\infty} 2\theta(\varepsilon_F - \varepsilon_i)|\phi_i(\mathbf{x})|^2 = 2\sum_{i=0}^{\frac{N}{2}-1} |\phi_i(\mathbf{x})|^2, \tag{2.19}$$

with ε_0 being the lowest single-electron eigenvalue. By comparing Eq. (2.18) to Eq. (2.7) and plugging the expressions in Eqs. (2.12) and (2.10) we obtain

$$\begin{aligned} V^{KS}(\mathbf{x}) &= V_{ext}(\mathbf{x}) + \int d\mathbf{x}\frac{n_0(\mathbf{x})}{|\mathbf{x} - \mathbf{x}'|} + \left| \frac{\delta E_{xc}[n_0]}{\delta n_0(\mathbf{x})} \right|_{\alpha=0} = \\ &= V_{ext}(\mathbf{x}) + V_H(\mathbf{x}) + V_{xc}(\mathbf{x}). \end{aligned} \tag{2.20}$$

If we knew the functional form of E_{xc} we would be able to solve the ground state of the system exactly. However, this is not possible and approximations are necessary.

---

[1]The Fermi-Dirac distribution at finite temperature is given as $f_\varepsilon(T) = \frac{2}{e^{(\varepsilon-\varepsilon_F)/\kappa_B T}-1}$, where T is temperature and κ_B the Boltzmann constant.

Many E_{xc} functionals have been proposed in the last years, each of them with some benefits and pathologies [44–46]. As deep theoretical analysis and development of E_{xc} functionals lay far from the objectives of this thesis, we will briefly describe those that have been used in our calculations.

2.2.1 LDA and GGA functionals

By far the most famous E_{xc} approximation is the Local Density Approximation (LDA) [42], which assumes this energy contribution is just a functional of the ground state density in each point of the system[2]:

$$E_{xc}^{LDA}[n] = \int d\mathbf{x} \; n(\mathbf{x})\varepsilon_{xc}^{HEG}[n(\mathbf{x})]. \tag{2.21}$$

The upper HEG index holds for homogeneous electron gas [47], where the density is constant throughout space. Here, we assume the expression is still valid when the density varies from point to point. In most solids the behavior of electrons is quite close to the one in a HEG and one may assume the functional form is the same. Moreover, this assumption is justified due to the fact that one recovers the same analytical form at high densities and slowly-varying ones.

The LDA energy is parametrized as follows [48]:

$$\varepsilon_{xc}^{LDA}[n] = \varepsilon_{x}^{HEG}[n] + \varepsilon_{c}^{HEG}[n], \tag{2.22}$$

where the exchange term reads as

$$\varepsilon_{x}^{HEG}[n] = -\frac{3}{4}\left(\frac{3}{\pi}\right)^{1/3} n^{1/3}. \tag{2.23}$$

Various parametrizations of this correlation term have been tabulated for different densities [49–52]. In this thesis we will use two of the most typical parametrizations for the correlation, given by Perdew and Zunger [52] and Perdew and Wang [53].

Looking at the nature of the approximation one can see that it will work reasonably well unless the inhomogeneities are high, as in isolated atoms. Even though it seems a too simple or rough approximation it is able to give much better results than expected. However, it has some known pathologies that are usually general. For instance, the most remarkable is the overestimation of binding energies and its consequent underestimation of bond lengths.

---

[2]We drop the 0 indices for simplicity.

Taking advantage of the good behavior and results obtained within the LDA, semilocal approximations have been developed in order to take into account the inhomogeneities $n(\mathbf{x})$ may have. This is performed including non-local terms as it is done in the Generalized Gradient Approximation (GGA), which introduces a correction with the gradient of the density:

$$E_{xc}^{GGA}[n] = \int d\mathbf{x} \; n(\mathbf{x})\varepsilon_{xc}[n(\mathbf{x}), |\nabla n(\mathbf{x})|]. \qquad (2.24)$$

In our calculations we used the PBE parametrization of the E_{xc} [45]:

$$E_{xc}^{GGA}[n] = E_x^{GGA}[n] + E_c^{GGA}[n]. \qquad (2.25)$$

The exchange term reads

$$E_x^{GGA}[n] = \int d\mathbf{x} \; n(\mathbf{x})\varepsilon_x^{HEG}[n(\mathbf{x})]F_x(s), \qquad (2.26)$$

where ε_x^{HEG} is the one used in the LDA and $F_x(s) = 1 + 0.804(1 - [1 + 0.273s^2]^{-1})$ introduces the gradient correction to the density via the dimensionless parameter $s = 0.1616|\nabla n|/n^{4/3}$. It is straightforward to see that one obtains the LDA limit for vanishing gradient. E_C is constructed using the dimensionless parameter $t = 0.9669|\nabla n|/n^{3/2}$,

$$E_c^{GGA}[n] = \int d\mathbf{x} \; n(\mathbf{x})(\varepsilon_c^{HEG}[n(\mathbf{x})] + F_c[n(\mathbf{x}), t]). \qquad (2.27)$$

$F_c[n(\mathbf{x}), t]$ is built to fit some specific limiting values [45, 54, 55].

Unfortunately, some solids show sharp density inhomogeneities making the gradient expansion break down. Moreover, LDA fulfills several sum rules that are violated by the GGA [56]. Thus, GGA does not necessarily improve LDA results, being the choice of one or another approximation system dependent. In this work we have mostly used the PBE-GGA approximation [45], even though PZ-LDA [52], PW-LDA [53] and other approximations have also been used for comparison with other works and for testing. Testing different functionals helps in order to differentiate real physical properties from artifacts coming from inappropriate choices of the exchange-correlation functional approximation.

2.3   Bloch's theorem and plane-wave basis sets

As our analyzed systems have crystalline structures, we will take advantage of their periodicity. Due to the periodic structure of a crystal lattice the Hamiltonian is

periodic. That has straightforward implications in the wavefunctions that will make our work easier.

For any $\mathbf{T}$ lattice vector

$$H^e(\mathbf{r}) = H^e(\mathbf{r} + \mathbf{T}), \tag{2.28}$$

which also holds for any effective single-electron Hamiltonian and potential. In this section we will write them as $H^{KS}(\mathbf{x})$ and $V^{KS}(\mathbf{x})$, respectively, for notation simplicity as our main mean field theory of choice will be DFT. However, Bloch's theorem is valid at any theory.

Bloch's theorem proves that one-electron solutions (Bloch states) must be of the following form [48]:

$$\phi_{n\mathbf{k}}(\mathbf{x}) = e^{i\mathbf{k}\cdot\mathbf{x}}u_{n\mathbf{k}}(\mathbf{x})$$
$$\phi_{n\mathbf{k}}(\mathbf{x} + \mathbf{T}) = e^{i\mathbf{k}\cdot\mathbf{T}}\phi_{n\mathbf{k}}(\mathbf{x}), \tag{2.29}$$

where $u_{n\mathbf{k}}(\mathbf{x})$ has the periodicity of the lattice. n is the band index and $\mathbf{k}$ is the wave vector of the electron. Applying Born-Von Karman boundary conditions the possible values of $\mathbf{k}$ reduce to the number of unit cells $N_{\mathbf{k}} \propto 10^{23}$:

$$\mathbf{k}_{m_{\mathbf{b}_i}} = \sum_{\mathbf{b}_i} m_{\mathbf{b}_i}/N_{\mathbf{b}_i}\mathbf{b}_i \qquad m_{\mathbf{b}_i} \in [0, N_{\mathbf{b}_i} - 1]. \tag{2.30}$$

$\mathbf{b}_i$, $i = 1, 2, 3$ are the three basis vectors of the reciprocal lattice, $N_{\mathbf{b}_i}$ is the number of unit cells in the direction of $\mathbf{b}_i$ and, therefore, $N_{\mathbf{k}} = N_{\mathbf{b}_1}N_{\mathbf{b}_2}N_{\mathbf{b}_3}$. In this new notation the eigenenergies are $\varepsilon_{n\mathbf{k}}$ and the electronic structure is obtained plotting the energy for different wave vectors in the first Brillouin Zone (BZ) consisting of all the independent wavevectors.

Looking at the wavefunctions in Eq. (2.29) one can think of plane waves as a good basis set for writing our one-electron eigenstates [48]:

$$|\phi_{n\mathbf{k}}\rangle = \sum_{\mathbf{k}'} c^n_{\mathbf{k}\mathbf{k}'} |\mathbf{k}'\rangle, \tag{2.31}$$

where $\langle\mathbf{x}|\mathbf{k}\rangle = 1/\sqrt{N_{\mathbf{k}}\Omega_{BZ}}e^{i\mathbf{k}\cdot\mathbf{x}}$, Ω_{BZ} is the first BZ volume and $c^n_{\mathbf{k}\mathbf{k}'}$ is a complex tensor tensor containing the coefficients of the expansion. The coefficients can be obtained by diagonalizing H^{KS} written in the plane-wave basis, which reads

$$\langle\mathbf{k}| H^{KS} |\mathbf{k}'\rangle = -\frac{1}{2} \langle\mathbf{k}|\nabla^2|\mathbf{k}'\rangle + \langle\mathbf{k}| V^{KS} |\mathbf{k}'\rangle. \tag{2.32}$$

Since H^{KS} is periodic, being $\tau(\mathbf{T})$ the translation operator:

$$\langle\mathbf{k}| H^{KS} |\mathbf{k}'\rangle = \langle\mathbf{k}|\tau^{-1}(\mathbf{T})H^{KS}\tau(\mathbf{T})|\mathbf{k}'\rangle = e^{i(\mathbf{k}'-\mathbf{k})\cdot\mathbf{T}} \langle\mathbf{k}|H^{KS}|\mathbf{k}'\rangle \tag{2.33}$$

Therefore, holding the equality

$$e^{i(\mathbf{k}-\mathbf{k}')\cdot\mathbf{T}} = 1 \Rightarrow \mathbf{k} - \mathbf{k}' = \mathbf{G} \tag{2.34}$$

where $\mathbf{G}$ is any reciprocal lattice vector, we have arrived to the conclusion that the Hamiltonian couples only wave vectors differing just by a reciprocal lattice vector. As we have obtained a block diagonal Hamiltonian we can diagonalize each block associated to different $\mathbf{k}$ vectors just in the first BZ independently:

$$\langle \mathbf{k} - \mathbf{G} | H^{KS} | \mathbf{k} - \mathbf{G}' \rangle = -\frac{\mathbf{k} - \mathbf{G}^2}{2} \delta_{\mathbf{G}\mathbf{G}'} + V^{KS}(\mathbf{G}' - \mathbf{G}). \tag{2.35}$$

Since the kinetic operator is diagonal in the momentum representation, the equation above means the coupling values are just the Fourier components of the also periodic effective potential

$$V^{KS}(\mathbf{G}) = \langle \mathbf{k} | V^{KS} | \mathbf{k} - \mathbf{G} \rangle = \int_{\Omega_{BZ}} d\mathbf{x} \, V^{KS}(\mathbf{x}) e^{-i\mathbf{G}\cdot\mathbf{x}}. \tag{2.36}$$

This way, the final single-electron eigenstates will have the form

$$|\phi_{n\mathbf{k}}\rangle = \sum_{\mathbf{G}} c^n_{\mathbf{k}\text{-}\mathbf{G}} |\mathbf{k} - \mathbf{G}\rangle \tag{2.37}$$

$$\phi_{n\mathbf{k}}(\mathbf{x}) = \langle \mathbf{x} | \phi_{n\mathbf{k}} \rangle = \frac{1}{\sqrt{N_{\mathbf{k}}\Omega_{BZ}}} \sum_{\mathbf{G}} c^n_{\mathbf{k}\text{-}\mathbf{G}} e^{i(\mathbf{k}-\mathbf{G})\cdot\mathbf{x}} \tag{2.38}$$

It is straightforward to see that the obtained eigenfunctions are Bloch wavefunctions.

2.4 Pseudopotentials

In the beginning of this chapter we described a piece of matter as a system composed by nuclei and electrons. However, in some cases it is much more convenient to treat valence electrons and core electrons separately. This way, matter would be composed by ions (each of them composed by a nucleus and core electrons) and valence electrons, the outermost layers' electrons of the atoms that are responsible for chemical interactions.

However, considering ions as fixed point charges with frozen core electrons is a very rough and inaccurate approximation. Electronic wavefunctions must be orthogonal

and Pauli exclusion principle rules the level filling. Taking a bare ionic potential as v_{ext} and plugging it into Eq. (2.5) one would neglect the consequences of core electrons in the valence electrons' wavefunctions. In order to properly take the inner structure of the ions into account while reducing computational costs pseudopotentials are constructed, which smooth out the oscillatory core part of the potential and the corresponding wavefunction while the valence part remains essentially unaltered [47, 57]. Even though pseudopotential development lays far from this thesis' objectives, we will briefly explain how they are built.

First of all, the whole electronic configuration of the isolated atom is calculated, in our particular case using DFT with the desired E_{xc} approximation. Once all the wavefunctions are obtained the valence electrons are chosen. Which and how many valence electrons to chose is optional and depends on the desired accuracy and the nature of the system one wants to analyze. As a consequence of orthogonality, valence electrons' wavefunctions oscillate locally near the nucleus. These oscillations are very expensive to compute[3]. Therefore, we assume that the closest part to the nucleus of the wave function has little influence in our system and we create a so-called pseudo-wavefunction $\phi_i^{ps}(\mathbf{x})$ for each orbital i which replaces the oscillations by a smooth function $\phi_i^{smooth}(\mathbf{x})$, and coincides with the original all-electron wave function ϕ_i^{ae} outside a radius known as the cutoff radius R_c:

$$\phi_i^{ps}(\mathbf{x}) = \begin{cases} \phi_i^{smooth}(\mathbf{x}), & \text{, for } |\mathbf{x}| < R_c \\ \phi_i^{ae}(\mathbf{x}), & \text{, for } |\mathbf{x}| \geq R_c \end{cases}. \tag{2.39}$$

Once we have the pseudo-wave functions of the valence electrons, solving

$$\left(-\frac{1}{2}\nabla^2 + v_i^{ps}(\mathbf{x})\right)\phi_i^{ps}(\mathbf{x}) = \varepsilon_i\phi_i^{ps}(\mathbf{x}). \tag{2.40}$$

we obtain $v_i^{ps}(\mathbf{x})$ for each orbital channel. That pseudopotential is the one we will use to build v_{ext}, which will take into account the inner electrons of the ion. A schematic illustration of the procedure is shown in Fig. 2.1.

While the energy and the valence electron density produced by the pseudo-wave-function must be the same as the all-electron wavefunction, ϕ_i^{smooth} is non-unique; how one builds this smooth part, along with which electrons are considered as valence electrons, differentiates one pseudopotential from another. In this thesis we have mostly used norm-conserving [58, 59] and ultrasoft [60] pseudopotentials. In norm-conserving pseudopotentials the charge enclosed by the core radius in the all-electron wavefunction is preserved in the pseudo-wavefunction. Ultrasoft

---

[3]Using a plane-wave basis this implies the need of more wavefunctions to describe them properly, thus, requiring more time and memory.
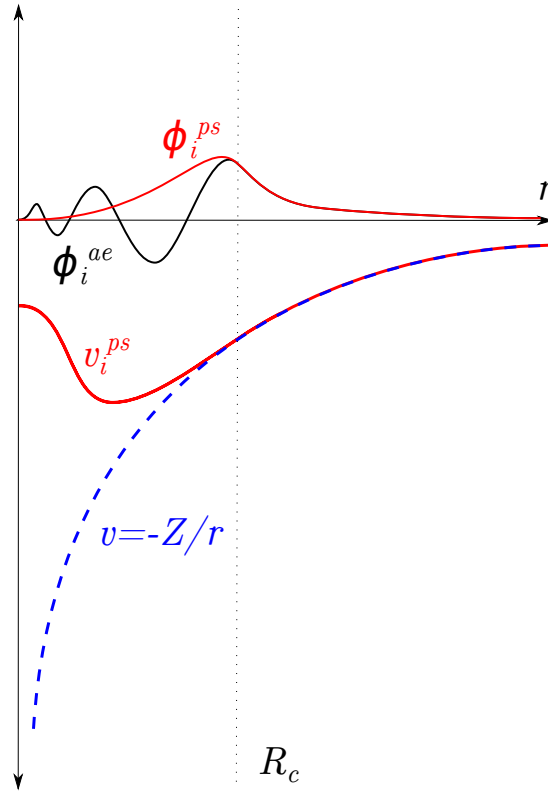
Figure 2.1:   Simplified qualitative representation of a pseudopotential and a pseudo-wavefunction (radial dependence shown only). The dashed blue curve shows the bare Coulomb potential of an ion seen by an electron, considering the core electrons are frozen. The black curve displays the "exact" wavefunction ϕ_i^{ae} of the valence electron obtained from the all-electron calculation. Red curves show the constructed pseudo-wavefunction ϕ_i^{ps} and its associated pseudopotential v_i^{ps} obtained by inverting the Schrödinger equation.

pseudopotentials relax the norm-conserving constraint allowing for a smoother core part of the wavefunction and, thus, requiring less plane waves, yet compromising transferability from one system to another and making more testing necessary to avoid spurious results.

In this work, some of the calculations will be performed in hydrogen crystals. One could think that using pseudopotentials in hydrogen is a nonsense; nevertheless, in spite of the lack of nodes of the occupied $1s$ state, its wavefunction is quite sharp around the maximum, and smoothing it can speed up calculations by reducing the amount of plane waves. Besides, the inclusion of additional unoccupied channels is often necessary and the need of pseudopotentials in hydrogen becomes more evident.
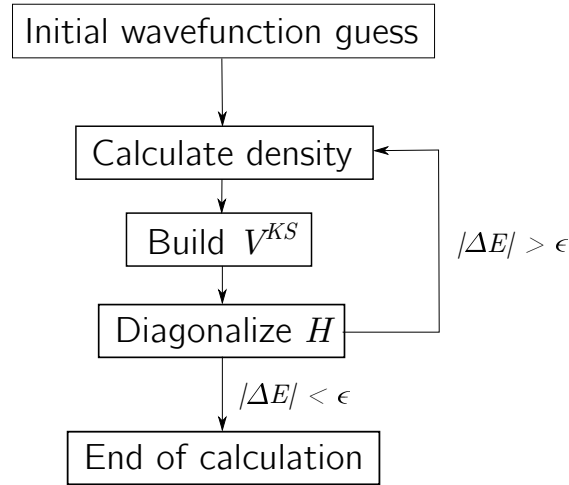
Figure 2.2: Flowchart of the self-consistent cycle for solving the Kohn-Sham equation. ΔE and ε are the energy difference between the current cycle and the previous one and the chosen threshold, respectively.

2.5 Computational method

Now that we have all the theoretical ingredients to perform an electronic structure calculation we are ready to implement it computationally. We have made all our electronic structure calculations using the software suite QUANTUM ES-PRESSO [61].

The procedure of the self-consistent calculation is shown in Fig. 2.2. For the first cycle a guess of the total wavefunction is introduced built by the superposition of individual atom's valence electrons wavefunctions, which provides an initial electronic ground state density. With this density we are able to construct the whole V^{KS} potential and therefore to solve the Kohn-Sham eigenvalue equation (2.7). The eigenfunctions provide a new electronic density to start over a cycle. One stops this self-consistent loop when the chosen accuracy (defined by a threshold value) is reached for the total energy.

If we look at equation (2.37) we see that in order to obtain the exact Kohn-Sham state the sum should be extended to infinity. As this is practically impossible, one must fix an energy cutoff $(E_{cutoff} \geq 1/2|\mathbf{k} + \mathbf{G}|^2)$ for the plane waves in order to truncate the sum. The value of this cutoff determines the number of $\mathbf{G}$ vectors in the expansion and needs to be chosen to satisfy the desired accuracy. E_{cutoff} depends on both the system to analyze and the pseudopotentials.

On the other hand, for an ideal infinite crystal the number of $\mathbf{k}$ vectors in the

first Brillouin zone is also infinite. Instead, we divide it in a finite Monkhorst-Pack grid [62] that has also to be chosen and optimized. For a better and faster convergence in metals, the step function in Eq. (2.19) is commonly substituted by a smoother or a smeared out function, effectively introducing a low electronic temperature. We have used the Methfessel-Paxton smearing for such purpose [63].

Electronic structure calculations are easily parallelized taking advantage of the independence of the wave vectors. We have used computer clusters to run all the calculations in many interconnected processors in order to speed them up.

Chapter 3

The nuclear problem

The adiabatic Born-Oppenheimer approximation left us with two equations to solve. So far, we have shown how to solve the first one corresponding to the electronic part. Even though electronic degrees of freedom are responsible of many properties of solids, many others, such as thermal conductivity and superconductivity, arise due to nuclear (or ionic) degrees of freedom.

In order to know about the nuclear motion we have to solve the nuclear Schrödinger equation (1.12). As we can see, ions move in a potential that is just the electronic energy obtained in the previously solved equation (1.5). This potential is usually referred to as the Born-Oppenheimer Energy Surface (BOES) and it is different for each electronic energy state. In our case, we will focus on solving the one corresponding to the electronic ground state ($\alpha = 0$), as it is done in the adiabatic approximation.

From Eq. (1.13) we see that the nuclear potential is $U(\mathbf{R}) \equiv E_0^e(\mathbf{R})$, where the nuclear positions are not fixed parameters anymore. We are dealing with a many-body problem and a BOES of $\sim 10^{23}$ degrees of freedom, meaning the system is unsolvable unless some approximation is considered. When displacements are much smaller than the interatomic distances a low-order Taylor expansion of the potential may often be a valid approximation.

3.1   The harmonic approximation

In a crystal ions move around their equilibrium lattice sites, which are defined as the positions of the nuclei at the local minimum of the BOES corresponding to

the crystal structure under analysis. This way, we can define the position of the sth nucleus in the mth unit cell as

$$\mathbf{R}_{ms} = \mathbf{T}_m + \boldsymbol{\tau}_s + \mathbf{u}_{ms} = \mathbf{R}^0_{ms} + \mathbf{u}_{ms}, \tag{3.1}$$

where $\mathbf{u}_{ms}$ is the displacement of this atom from its equilibrium position $\mathbf{R}^0_{ms}$, $\mathbf{T}_m$ is a lattice vector from the origin to the origin of the mth cell and $\boldsymbol{\tau}_s$ is a basis vector that denotes the equilibrium position of the sth atom inside the unit cell.

Once the equilibrium positions of the crystal structure are fixed, we can Taylor expand the BOES in the displacements:

$$
\begin{aligned}
U(\mathbf{R}) = & \ U(\mathbf{R}^0) + \sum_{msl} \left. \frac{\partial U}{\partial u^l_{ms}} \right|_{\mathbf{R}^0} u^l_{ms} + \frac{1}{2} \sum_{msl} \sum_{m's'l'} \left. \frac{\partial^2 U}{\partial u^l_{ms} \partial u^{l'}_{m's'}} \right|_{\mathbf{R}^0} u^l_{ms} u^{l'}_{m's'} + \\
& + \frac{1}{6} \sum_{msl} \sum_{m's'l'} \sum_{m''s''l''} \left. \frac{\partial^3 U}{\partial u^l_{ms} \partial u^{l'}_{m's'} \partial u^{l''}_{m''s''}} \right|_{\mathbf{R}^0} u^l_{ms} u^{l'}_{m's'} u^{l''}_{m''s''} + (\ldots), \tag{3.2}
\end{aligned}
$$

where m runs up to $N_\mathbf{q}$, the number of units cell or, equivalently, the number of $\mathbf{q}$-points in the first BZ taken into account for solving the nuclear problem which are not necessarily the same as $N_\mathbf{k}$. The atom index s runs from 1 to N_s, the number of atoms per unit cell and l runs on the Cartesian coordinates x, y and z.

Since at equilibrium the first order $\left. \frac{\partial U}{\partial u^l_{ms}} \right|_{\mathbf{R}^0}$ term is identically zero by definition, the lowest order approximation one can make to account for the nuclear motion is the one retaining terms up to second order in the displacements. This is the so-called Harmonic approximation and the nuclear Hamiltonian now reads [64]:

$$H_I(\mathbf{R}) \approx U(\mathbf{R}^0) + \sum_{msl} \frac{(P^l_{ms})^2}{2m_s} + \frac{1}{2} \sum_{msl} \sum_{m's'l'} \Phi^{ll'}_{msm's'} u^l_{ms} u^{l'}_{m's'}, \tag{3.3}$$

where

$$\Phi^{ll'}_{msm's'} \equiv \left. \frac{\partial^2 U}{\partial u^l_{ms} \partial u^{l'}_{m's'}} \right|_{\mathbf{R}^0} \tag{3.4}$$

are the interatomic force constants.

It is convenient to define the Fourier transformed force constants as

$$\Phi^{ll'}_{ss'}(\mathbf{q}, \mathbf{q}') = \frac{1}{N_\mathbf{q}} \sum_{mm'} \Phi^{ll'}_{msm's'} e^{-i(\mathbf{q} \cdot \mathbf{T}_m + \mathbf{q}' \cdot \mathbf{T}_{m'})}. \tag{3.5}$$

Interestingly, due to translational symmetry the force constants only depend on $\mathbf{T}_m - \mathbf{T}_{m'}$. Therefore, only the terms with $\mathbf{q}' = -\mathbf{q}$ survive and Eq. (3.5) is simplified to

$$\Phi^{ll'}_{ss'}(\mathbf{q}) = \Phi^{ll'}_{ss'}(\mathbf{q}, -\mathbf{q}) = \sum_m \Phi^{ll'}_{ms0s'} e^{-i\mathbf{q} \cdot \mathbf{T}_m}. \tag{3.6}$$

Let us also define in a similar fashion the Fourier transforms of the nuclear displacement and momentum operators

$$u_s^l(\mathbf{q}) = \frac{1}{\sqrt{N_\mathbf{q}}} \sum_n e^{i\mathbf{q}\cdot\mathbf{T}_m} u_{ms}^l \qquad (3.7)$$

$$P_s^l(\mathbf{q}) = \frac{1}{\sqrt{N_\mathbf{q}}} \sum_n e^{-i\mathbf{q}\cdot\mathbf{T}_m} P_{ms}^l. \qquad (3.8)$$

$$\qquad (3.9)$$

The crucial step in order to diagonalize the Hamiltonian is to assume the following transformation to the bosonic ladder operators,

$$u_s(\mathbf{q}) = \sum_\mu \frac{1}{\sqrt{2m_s\omega_\mu(\mathbf{q})}} \epsilon_{s\mu}^l(\mathbf{q}) \left(b_{\mu\mathbf{q}} + b_{\mu-\mathbf{q}}^\dagger \right) \qquad (3.10)$$

$$P_s(\mathbf{q}) = -i \sum_\mu \sqrt{\frac{m_s\omega_\mu(\mathbf{q})}{2}} \epsilon_{s\mu}^l(\mathbf{q}) \left(b_{\mu\mathbf{q}} - b_{\mu-\mathbf{q}}^\dagger \right), \qquad (3.11)$$

which satisfy the following commutation algebra:

$$[b_{\mu\mathbf{q}}, b_{\mu'\mathbf{q}'}^\dagger] = \delta_{\mu\mu'}\delta_{\mathbf{q}\mathbf{q}'}, \ [b_{\mu\mathbf{q}}, b_{\mu'\mathbf{q}'}] = 0, \ [b_{\mu\mathbf{q}}^\dagger, b_{\mu'\mathbf{q}'}^\dagger] = 0. \qquad (3.12)$$

This way, the nuclear Hamiltonian in the harmonic approximation in second quantization can be written as a sum of independent harmonic oscillators [48, 65, 66]:

$$H_I = U_0 + \sum_\mu \sum_\mathbf{q}^{1BZ} \omega_\mu(\mathbf{q}) \left(b_{\mu\mathbf{q}}^\dagger b_{\mu\mathbf{q}} + \frac{1}{2} \right), \qquad (3.13)$$

with the following eigenenergies

$$\Omega_\mu(\mathbf{q}) = U_0 + \omega_\mu(\mathbf{q})(n_{\mu\mathbf{q}} + \frac{1}{2}) \qquad (3.14)$$

Here, U_0 is the ground state energy of the electronic system at equilibrium (which includes the contribution coming from the nuclei-nuclei interaction) at the local minimum of the BOES and $\boldsymbol{\epsilon}_{s\mu}(\mathbf{q})$ and $\omega_\mu(\mathbf{q})$ are, respectively, the polarization vector (of atom s in the unit cell) and the frequency of the vibrational mode μ with momentum $\mathbf{q}$. $n_{\mu\mathbf{q}}$ denotes the occupation level of a mode, in such a way that when a given mode is excited to the $n_{\mu\mathbf{q}}^{th}$ level, we would say that we have $n_{\mu\mathbf{q}}$ phonons of that mode. In practice even the frequencies of the vibrational modes $\omega_\mu(\mathbf{q})$ are often called *phonon frequencies* and the phonon frequency vs. momentum dispersion relation is called *phonon spectrum*. The polarization vectors

(eigenvectors) and phonon frequencies (eigenvalues) are obtained by diagonalizing the dynamical matrix $D^{ll'}_{ss'}(\mathbf{q}) = \Phi^{ll'}_{ss'}(\mathbf{q})/\sqrt{m_s m_{s'}}$, so that

$$\omega^2_\mu(\mathbf{q})\epsilon^l_{s\mu}(\mathbf{q}) = \sum_{s'}\sum_{l'} D^{ll'}_{ss'}(\mathbf{q})\epsilon^{l'}_{s'\mu}(\mathbf{q}). \tag{3.15}$$

Finally, the energy per unit cell of a total state $|\beta\rangle = |n_{1\mathbf{q}_1}\dots n_{3N_s\mathbf{q}_1}\dots n_{3N_s\mathbf{q}_{N_{\mathbf{q}}}}\rangle$, is given by

$$E^{cell}_\beta = \frac{1}{N_{\mathbf{k}}}U_0 + \frac{1}{N_{\mathbf{q}}}\sum_\mu\sum_{\mathbf{q}}^{1BZ}\omega_\mu(\mathbf{q})\left(n_{\mu\mathbf{q}} + \frac{1}{2}\right). \tag{3.16}$$

In particular, as phonons are bosons they follow Bose-Einstein statistics and the total energy at a given temperature can be calculated as

$$E^{cell}(T) = \frac{1}{N_{\mathbf{k}}}U_0 + \frac{1}{N_{\mathbf{q}}}\sum_\mu\sum_{\mathbf{q}}^{1BZ}\omega_\mu(\mathbf{q})\left(n_B(\omega_\mu(\mathbf{q})) + \frac{1}{2}\right). \tag{3.17}$$

where

$$n_B(\omega_\mu(\mathbf{q})) = \frac{1}{e^{\beta\omega_\mu(\mathbf{q})} - 1} \tag{3.18}$$

is the usual Bose-Einstein distribution function. The zero point energy (ZPE) of the system is defined as

$$E^{cell}_{ZPE} = E^{cell}(T=0) = \frac{1}{N_{\mathbf{k}}}U_0 + \frac{1}{N_{\mathbf{q}}}\frac{1}{2}\sum_\mu\sum_{\mathbf{q}}^{1BZ}\omega_\mu(\mathbf{q}). \tag{3.19}$$

3.2   Phonons from linear response theory

Once we have formulated the nuclear problem in the harmonic approximation, we need to calculate the derivatives of U appearing in Eq. (3.3) in order to obtain the dynamical matrices. Unfortunately, an *ab initio* calculation of these derivatives can be extremely cumbersome. Hellmann-Feynman theorem [67, 68] allows us to calculate first derivatives easily such that

$$\frac{\partial U}{\partial u^l_{ms}} = \langle\psi^e_0|\frac{\partial H^e}{\partial u^l_{ms}}|\psi^e_0\rangle = \frac{\partial V_{I,I}}{\partial u^l_{ms}} + \int d\mathbf{x}\, n(\mathbf{x})\frac{\partial V_{ext}(\mathbf{x})}{\partial u^l_{ms}}. \tag{3.20}$$

This relation holds since the only explicit dependence on the nuclear coordinates of H^e comes from the external potential V_{ext} and the Coulomb internuclear interaction $V_{I,I}$. In order to obtain the second derivatives at equilibrium needed for the

dynamical matrices, from Eq. (3.20) straightforwardly

$$
\begin{aligned}
\Phi^{ll'}_{msm's'} &= \left.\frac{\partial^2 U}{\partial u^l_{ms}\partial u^{l'}_{m's'}}\right|_{\mathbf{R}^0} = \int \mathrm{d}\mathbf{x}\ \left.\frac{\partial n(\mathbf{x})}{\partial u^l_{ms}}\right|_{\mathbf{R}^0} \left.\frac{\partial V_{ext}(\mathbf{x})}{\partial u^{l'}_{m's'}}\right|_{\mathbf{R}^0} + \\
&+ \int \mathrm{d}\mathbf{x}\ n(\mathbf{x})\left.\frac{\partial^2 V_{ext}(\mathbf{x})}{\partial u^l_{ms}\partial u^{l'}_{m's'}}\right|_{\mathbf{R}^0} + \left.\frac{\partial^2 V_{I,I}}{\partial u^l_{ms}\partial u^{l'}_{m's'}}\right|_{\mathbf{R}^0}.
\end{aligned}
\tag{3.21}
$$

This last fundamental equation shows how phonons can be calculated from the electronic properties at the nuclear equilibrium positions as it was already stated by Pick, Cohen and Martin [69]. However, the second derivatives require the knowledge not only of the electron density $n(\mathbf{x})$, but of its derivatives with respect to the nuclear positions $\frac{\partial n(\mathbf{x})}{\partial u^l_{ms}}$ as well. While the electronic density at equilibrium has been previously obtained in the electronic structure calculation, the latter needs to be calculated *a posteriori*.

Linear response theory allows to calculate derivatives of the density [70]. The change in the electronic density induced by any external potential Φ^{ext} is related to the density-response function $\chi(\mathbf{x}, \mathbf{x}')$ as follows:

$$
\delta n(\mathbf{x}) = \int \mathrm{d}\mathbf{x}'\chi(\mathbf{x}, \mathbf{x}')\Phi^{ext}(\mathbf{x}').
\tag{3.22}
$$

In the case of lattice vibrations $\Phi^{ext} = \delta V_{ext}$, which means the external potential is the change in the electron-ion interaction due to the displacement of ions from their equilibrium position. The next step is to assume both density and electron-ion potential changes are linear with respect to nuclear displacements. If one expands any function f in the atomic displacements up to first order as $f(\mathbf{x}) = f^0(\mathbf{x}) + \Delta f(\mathbf{x})$, where $f^0(\mathbf{x})$ is the value of the f with the ions at their equilibrium sites and

$$
\Delta f(\mathbf{x}) = \sum_{msl}\left.\frac{\partial f(\mathbf{x})}{\partial u^l_{ms}}\right|_{\mathbf{R}^0} u^l_{ms},
\tag{3.23}
$$

we can rewrite Eq. (3.22) as follows:

$$
\Delta n(\mathbf{x}) = \int \mathrm{d}\mathbf{x}'\chi(\mathbf{x}, \mathbf{x}')\Delta V_{ext}(\mathbf{x}').
\tag{3.24}
$$

It is, thus, straightforward to show the second derivatives can be written in terms of the electronic density-response function as

$$
\begin{aligned}
\left.\frac{\partial^2 U(\mathbf{R})}{\partial u^l_{ms}\partial u^{l'}_{m's'}}\right|_{\mathbf{R}^0} &= \int \mathrm{d}\mathbf{x}\mathrm{d}\mathbf{x}'\ \left.\frac{\partial V_{ext}(\mathbf{x})}{\partial u^l_{ms}}\right|_{\mathbf{R}^0}\chi(\mathbf{x}, \mathbf{x}')\left.\frac{\partial V_{ext}(\mathbf{x}')}{\partial u^{l'}_{m's'}}\right|_{\mathbf{R}^0} \\
&+ \int \mathrm{d}\mathbf{x}\ n(\mathbf{x})\left.\frac{\partial^2 V_{ext}(\mathbf{x})}{\partial u^l_{ms}\partial u^{l'}_{m's'}}\right|_{\mathbf{R}^0} + \left.\frac{\partial^2 V_{I,I}}{\partial u^l_{ms}\partial u^{l'}_{m's'}}\right|_{\mathbf{R}^0}.
\end{aligned}
\tag{3.25}
$$

The response function can be calculated with the following formula [71]:

$$
\begin{aligned}
\chi(\mathbf{x}, \mathbf{x}') &= \lim_{\eta \to 0^+} \sum_{\alpha} \frac{\langle \psi_0^e | n(\mathbf{x}) | \psi_\alpha^e \rangle \, \langle \psi_\alpha^e | n(\mathbf{x}') | \psi_0^e \rangle}{(E_0^e - E_\alpha^e) + i\eta} + \\
&\quad + \frac{\langle \psi_{e,0} | n(\mathbf{x}') | \psi_\alpha^e \rangle \, \langle \psi_\alpha^e | n(\mathbf{x}) | \psi_{e,0} \rangle}{(E_0^e - E_\alpha^e) - i\eta}
\end{aligned}
\tag{3.26}
$$

If in the equation above we plug Slater determinants constructed with non-interacting (Kohn-Sham, in the case of DFT) orbitals we obtain the so called non-interacting density-response function

$$
\chi_0(\mathbf{x}, \mathbf{x}') = \lim_{\eta \to 0^+} \sum_{\alpha_i, \alpha_i'} \phi_{\alpha_i}^*(\mathbf{x}) \phi_{\alpha_i'}(\mathbf{x}) \phi_{\alpha_i}(\mathbf{x}') \phi_{\alpha_i'}^*(\mathbf{x}') \frac{f_{\varepsilon_{\alpha_i}} - f_{\varepsilon_{\alpha_i'}}}{\varepsilon_{\alpha_i} - \varepsilon_{\alpha_i'} - i\eta},
\tag{3.27}
$$

where $\phi_{\alpha_i}(\mathbf{x})$ and ε_{α_i} are eigenfunctions and eigenvalues of an independent-electron Hamiltonian, and $f_{\varepsilon_{\alpha_i}}$ is the occupation of the state $|\phi_{\alpha_i}\rangle$ according to the Fermi-Dirac distribution. However, as electrons do not interact with each other, χ_0 cannot describe electronic screening. Instead, while χ connects the change in electronic density to the change in V_{ext}, χ_0 describes the response of non-interacting electrons with the already screened perturbation, which in the DFT formalism is ΔV^{KS}:

$$
\Delta n(\mathbf{x}) = \int d\mathbf{x}' \chi_0(\mathbf{x}, \mathbf{x}') \Delta V^{KS}(\mathbf{x}').
\tag{3.28}
$$

Finally, using Eqs. (2.20) (3.24) and (3.28) its easy to show χ and χ_0 are related by the Dyson equation:

$$
\chi(\mathbf{x}, \mathbf{x}') = \chi_0(\mathbf{x}, \mathbf{x}') + \iint d\mathbf{x}_1 d\mathbf{x}_2 \chi_0(\mathbf{x}, \mathbf{x}_1) K(\mathbf{x}_1, \mathbf{x}_2) \chi(\mathbf{x}_2, \mathbf{x}').
\tag{3.29}
$$

The kernel of the integral is the functional derivative of the electron-electron interaction potential with respect to the density:

$$
K(\mathbf{x}, \mathbf{x}') = \frac{\delta V_H(\mathbf{x})}{\delta n(\mathbf{x}')} + \frac{\delta V_{xc}(\mathbf{x})}{\delta n(\mathbf{x}')} = \frac{1}{|\mathbf{x} - \mathbf{x}'|} + f_{xc}(\mathbf{x}, \mathbf{x}')
\tag{3.30}
$$

This method has been successfully applied in several simple metallic solids and surfaces [72–75] but it also has some practical limitations [76]; calculating the response function *ab initio* is extremely computationally demanding for real systems since it includes a summation over unoccupied states. As we will see later in section 3.3, we can overcome this using perturbation theory. Before that, we will show a particular case in which χ_0 adopts an analytical expression: the homogeneous free-electron gas.

3.2.1 Phonons from Lindhard theory

Due to translational invariance, the response function of a homogeneous electron gas does not depend on the absolute coordinates $\mathbf{x}$ and $\mathbf{x}'$, but on $\mathbf{x} - \mathbf{x}'$:

$$\chi(\mathbf{x}, \mathbf{x}') = \chi(\mathbf{x} - \mathbf{x}'). \tag{3.31}$$

Consequently, its Fourier transform depends on a single momentum coordinate:

$$\chi(\mathbf{k}) = \frac{1}{V} \iint d\mathbf{x} d\mathbf{x}' \chi(\mathbf{x} - \mathbf{x}') e^{i\mathbf{k}\cdot(\mathbf{x}-\mathbf{x}')}, \tag{3.32}$$

meaning Eq. (3.24) adopts the following simple form in momentum space:

$$\Delta n(\mathbf{k}) = \chi(\mathbf{k}) \Delta V_{ext}(\mathbf{k}). \tag{3.33}$$

The same holds in the case of χ_0 and, therefore, the Dyson equation in momentum space reads as follows:

$$\chi(\mathbf{k}) = \chi_0(\mathbf{k}) + \chi_0(\mathbf{k}) K(\mathbf{k}) \chi(\mathbf{k}), \tag{3.34}$$

with simple arithmetic operations leading to

$$\chi(\mathbf{k}) = \frac{\chi_0(\mathbf{k})}{1 - K(\mathbf{k})\chi_0(\mathbf{k})}. \tag{3.35}$$

In the case of free electrons, whose parabolic energy-momentum dispersion and plane-wave eigenfunctions are well-known, χ_0 is analytical. Its expression in momentum space is known as the Lindhard formula and for a three-dimensional free-electron gas of density n it reads as follows:

$$\chi_0(\mathbf{k}) = -\frac{k_F}{\pi^2} F_L(|\mathbf{k}|/2k_F), \tag{3.36}$$

where $k_F = (3\pi^2 n)^{1/3}$ is the Fermi momentum and

$$F_L(x) = \frac{1}{2} + \frac{1 - x^2}{4x} \ln \left| \frac{1 + x}{1 - x} \right| \tag{3.37}$$

is the Lindhard function.

In the random phase approximation (RPA) we neglect the exchange-correlation term in K, and electronic screening is thus only considered with the Hartree term, which is analytical and in momentum space can be written as:

$$K(\mathbf{k}) = \frac{4\pi}{\mathbf{k}^2}. \tag{3.38}$$

Now, we have all the ingredients to write

$$\chi(\mathbf{k}) = \frac{\chi_0(\mathbf{k})}{1 - \frac{4\pi}{\mathbf{k}^2}\chi_0(\mathbf{k})}. \tag{3.39}$$

Lindhard theory, despite its simplicity, yields reasonably good results whenever the behavior of the electrons in the system under analysis is close to the homogeneous electron gas. The simple alkali metal sodium is a good example where the validity of this model holds at least up to a qualitative level [77], where this theory was even able to make predictions such as Kohn anomalies [78]. These kinks on the phonon branches are a consequence of the existence of a Fermi surface; they may appear whenever the wavevector of a phonon satisfied $|\mathbf{q} + \mathbf{G}| \sim 2k_f$ due to the discontinuity on the derivative of the Lindhard function (eq. (3.37)) at that point. However, one may expect this theory fails calamitously not only in insulators, but also in other metals with a more complex electronic structure than the one assumed here.

3.3   Density functional perturbation theory

In order to deal with the derivatives of the density, the main idea of density functional perturbation theory (DFPT) [79–81] is to apply first order perturbation theory to calculate the variation of the Kohn-Sham orbitals when the ions are displaced from their equilibrium position, allowing to obtain the induced electron density needed for calculating the force constant matrix (and, as we will see in Chapter 4, electron-phonon coupling coefficients as well) just summing over the occupied states.

The original Kohn-Sham problem was settled in Eq. (2.7) and the density given in Eq. (2.8). If we make a first order expansion in the Hamiltonian, the eigenvalues, the eigenfunctions and the density,

$$\begin{aligned}
H^{KS} &\rightarrow H^{KS} + \Delta H^{KS} \\
\varepsilon_{n\mathbf{k}} &\rightarrow \varepsilon_{n\mathbf{k}} + \Delta\varepsilon_{n\mathbf{k}} \\
|\phi_{n\mathbf{k}}\rangle &\rightarrow |\phi_{n\mathbf{k}}\rangle + |\Delta\phi_{n\mathbf{k}}\rangle \\
n(\mathbf{x}) &\rightarrow n(\mathbf{x}) + \Delta n(\mathbf{x}),
\end{aligned}$$

where $\langle\mathbf{x}|\Delta\phi_{n\mathbf{k}}\rangle = \Delta\phi_{n\mathbf{k}}(\mathbf{x})$, we obtain an eigenvalue problem at linear order that reads

$$(H^{KS} - \varepsilon_{n\mathbf{k}})\,|\Delta\phi_{n\mathbf{k}}\rangle = -(\Delta H^{KS} - \Delta\varepsilon_{n\mathbf{k}})\,|\phi_{n\mathbf{k}}\rangle \tag{3.40}$$

and, by simple derivation of Eq. (2.19) a density change

$$\Delta n(\mathbf{x}) = 2\mathfrak{Re} \sum_n \sum_{\mathbf{k}}^{1BZ} 2[\theta(\varepsilon_F - \varepsilon_{n\mathbf{k}})]\phi_{n\mathbf{k}}^*(\mathbf{x})\Delta\phi_{n\mathbf{k}}(\mathbf{x}), \qquad (3.41)$$

where the zero temperature Fermi-Dirac distribution function limits the sum to occupied states only. Eq. (3.40) is known as the Sternheimer equation [82] and is the perturbed version of eq. (2.7). Finally, the linear change of the Hamiltonian, ΔH^{KS}, can be derived making use of functional derivatives

$$\Delta H^{KS}(\mathbf{x}) = \Delta V_{ext}(\mathbf{x}) + \int d\mathbf{x}' K(\mathbf{x}, \mathbf{x}')\Delta n(\mathbf{x}') \qquad (3.42)$$

or, equivalently, since the kinetic energy change does not have a first order contribution,

$$\Delta H^{KS}(\mathbf{x}) \equiv \Delta V^{KS}(\mathbf{x}) = \Delta V_{ext}(\mathbf{x}) + \Delta V_H(\mathbf{x}) + \Delta V_{xc}(\mathbf{x}). \qquad (3.43)$$

The combination of Eqs. (3.40), (3.41) and (3.42) forms a set of self-consistent equations for the perturbed system that can be solved following a loop similar to the one in Fig. 2.2. The step function in Eq. (3.41) is smeared out as in the ground-state electronic calculation, using the same Methfessel-Paxton method [63].

Even though we have formulated the problem in terms of $\Delta n(\mathbf{x})$, we could have formulated it in terms of $\left.\frac{\partial n(\mathbf{x})}{\partial u_n s^l}\right|_{\mathbf{R}^0}$ considering that Eqs. (3.40), (3.41) and (3.42) must hold for all the coefficients in the expansion given in Eq. (3.23). Hence, the DFPT formalism described above gives the derivatives of the density needed to construct the dynamical matrices.

Our calculations of the dynamical matrices have been done using the *ph.x* package of QUANTUM ESPRESSO. In principle, one needs $N \sim 10^{23}$ dynamical matrices to sample the whole BZ. However, DFPT calculations are time demanding. Therefore, the usual procedure is to divide the BZ in a $\mathbf{q}$-point mesh and make the phonon calculation for those points. Afterwards, a discrete Fourier transform is done to obtain the force constant matrix of the system. Finally, one goes back to the reciprocal space by Fourier-transforming it again to the desired $\mathbf{q}$-points to plot the phonon spectra. These two last steps, which constitute the so-called Fourier interpolation, are performed by the packages *q2r.x* and *matdyn.x*, respectively.

3.4   Anharmonic effects in solids

In the harmonic approximation one makes the assumption that ions oscillate with a small amplitude near a fixed equilibrium position. Truncating the Taylor expansion in Eq. (3.3) at second order in the displacements we can diagonalize the Hamiltonian in terms of phonons that do not interact with each other. This assumption seems to be valid in most solids for temperatures below the melting point, specially for obtaining phonon frequencies and its associated physical properties [66]. There are, however, many important physical phenomena that cannot be explained within this approximation that arise entirely due to the higher order terms in the Taylor expansion. Within the harmonic approximation phonons have infinite lifetimes and do not decay which, for instance, implies a strictly harmonic crystal has an infinite thermal conductivity. In reality, solids obviously have a finite thermal conductivity and it is well known that the peaks observed in neutron scattering experiments have a measurable width, which is inversely proportional to the lifetime of a phonon. Moreover, the harmonic approximation is unable to explain the temperature dependence of phonons nor the thermal expansion of solids either.

Anharmonicity can be treated perturbatively by calculating explicitly more terms of the Taylor expansion of the potential. Third order terms can be efficiently computed in crystals using DFPT thanks to the $2n + 1$ theorem, which allows to obtain derivatives of the total energy up to $(2n + 1)^{th}$ order from n^{th} order derivatives of the density [83]. However, calculating higher-order terms *ab initio* is strongly complicated and perturbation theory is only valid in the regime where the harmonic potential is much larger than higher-order terms, which does not always hold. It can be the case that nuclear displacements cannot be considered small anymore making higher-order terms to be as important as, or even more than, the second-order ones. A source of such big displacements can be high temperature when a solid is close to melting, but even zero-point motion or low temperatures can be enough to break down both the harmonic and perturbative regimes in the presence of very light atoms or when the crystal is close to dynamical instabilities, as it happens in ferroelectrics or in materials exhibiting charge density waves.

Anharmonic effects at a non-perturbative level have been commonly treated with computationally expensive methods based on molecular dynamics simulations [84–91]. These approaches require long simulation times to obtain converged renormalized phonon spectra and, as they are based on Newtonian dynamics, their application is limited to temperatures above the Debye temperature. Path-integral molecular dynamics [92] overcomes this limitation by considering the quantum behavior of nuclei, but the computational cost of this approach is even greater. In

recent years, several methods [93–100] have been developed mainly inspired by the self-consistent harmonic approximation (SCHA) formulated by Hooton [101]. The SCHA uses the variational Gibbs-Bogoliubov (GB) principle in order to approximate the free energy of the true nuclear Hamiltonian with the free energy calculated with a trial harmonic density matrix for the same system, which does not necessarily coincide with the harmonic density matrix obtained from the harmonic approximation. In this thesis we use a stochastic implementation of the SCHA, the so-called stochastic self-consistent harmonic approximation (SSCHA) [93, 94].

3.4.1 The stochastic self-consistent harmonic approximation

In the SCHA the vibrational free energy of the system is minimized with respect to a trial density matrix which is chosen to be harmonic; this practically means the minimization is performed with respect to phonon frequencies, polarization vectors and average nuclear equilibrium positions. After minimization, one obtains effective phonon frequencies, polarization vectors and equilibrium positions which include anharmonic effects up to infinite order in a non-perturvative, variational way. The SSCHA has been successfully used in hydrides, such as platinum and palladium hydrides and the record superconductor H_3S [93, 94, 102, 103], charge density wave systems as Nb_2Se [104] and in ferroelectric and incipient ferroelectric chalcogenides [105].

Given the nuclear Hamiltonian $H = T_I + U$ in (we drop the I index from H^I in 1.13 for simplicity), the partition function reads $Z_H = \text{tr}\left[e^{-\beta H}\right]$ and the Helmholtz free energy is

$$F_H = -\frac{1}{\beta}\ln Z_H = \text{tr}\left(\rho_H H\right) + \frac{1}{\beta}\text{tr}\left(\rho_H \ln \rho_H\right), \tag{3.44}$$

where $\rho_H = e^{-\beta H}/tr[e^{-\beta H}]$ is the density matrix and $\beta = \frac{1}{\kappa_B T}$. We can define a trial Hamiltonian $\mathcal{H} = T_I + \mathcal{U}$ and build a trial density matrix $\rho_{\mathcal{H}}$ and write the corresponding free energy as

$$F_{\mathcal{H}} = \text{tr}\left(\rho_{\mathcal{H}}\mathcal{H}\right) + \frac{1}{\beta}\text{tr}\left(\rho_{\mathcal{H}} \ln \rho_{\mathcal{H}}\right). \tag{3.45}$$

If we take the trial density matrix $\rho_{\mathcal{H}}$ but compute the free energy with the actual anharmonic Hamiltonian H we obtain

$$\mathcal{F}_H(\mathcal{H}) = \text{tr}\left(\rho_{\mathcal{H}} H\right) + \frac{1}{\beta}\text{tr}\left(\rho_{\mathcal{H}} \ln \rho_{\mathcal{H}}\right), \tag{3.46}$$

which satisfies the Gibbs-Bogoliubov inequality

$$F_H \leq \mathcal{F}_H(\mathcal{H}). \tag{3.47}$$

By addition and subtraction of $\mathrm{tr}\,(\rho_\mathcal{H} \mathcal{H})$ and using Eq. (3.45) we get

$$\mathcal{F}_H(\mathcal{H}) = F_\mathcal{H} + \mathrm{tr}\,[\rho_\mathcal{H}\,(U - \mathcal{U})]\,, \tag{3.48}$$

which is the function that has to be minimized with respect to the trial Hamiltonian $\mathcal{H}$.

In the SCHA the trial potential $\mathcal{U}$ is restricted to a harmonic one, so $\mathcal{H}$ takes the form

$$\mathcal{H} = \sum_{ms}\sum_{l}\frac{\left(P_{ms}^l\right)^2}{2m_{ms}} + \frac{1}{2}\sum_{mm'}\sum_{ss'}\sum_{ll'}\tilde{u}_{ms}^l\,\widetilde{\Phi}_{mm'ss'}^{ll'}\,\tilde{u}_{m's'}^{l'}, \tag{3.49}$$

where $\widetilde{\Phi}_{nm'ss'}^{ll'}$ is the trial force constant matrix and the atomic displacements $\tilde{\mathbf{u}}_{m's'}$ are referred to the average nuclear positions $\tilde{\mathbf{R}}^0$, which are the centroids of the Gaussian harmonic density matrix. The advantage of using a harmonic trial Hamiltonian is that the term $F_\mathcal{H}$ in (3.48) and the density matrix $\rho_\mathcal{H}$ can be expressed in a closed form in terms of the phonon frequencies and polarization vectors, making calculations easier.

$\mathcal{F}_H(\mathcal{H})$ has to be minimized with respect to $\widetilde{\Phi}$, from which arises the implicit minimization with respect to phonon frequencies and polarization vectors, as diagonalizing the force constant matrices $\widetilde{\Phi}$ we obtain $\omega_{\mu\mathcal{H}}$ and $\varepsilon_{s\mu\mathcal{H}}^m$. Furthermore, it also has to be minimized with respect to the centroids $\tilde{\mathbf{R}}^0$, which are not necessarily the $\mathbf{R}^0$ positions of the minimum of the BOES.

The expressions for $\mathcal{F}_H(\mathcal{H})$ and its gradients are the following:

$$\mathcal{F}_H(\mathcal{H}) = F_\mathcal{H} + \int \mathrm{d}\mathbf{R}\,[U(\mathbf{R}) - \mathcal{U}(\mathbf{R})]\,\rho_\mathcal{H}(\mathbf{R}) \tag{3.50}$$

$$\nabla_{\tilde{\mathbf{R}}^0}\mathcal{F}_H(\mathcal{H}) = -\int \mathrm{d}\mathbf{R}\,[\mathbf{f}(\mathbf{R}) - \mathbf{f}_\mathcal{H}(\mathbf{R})]\,\rho_\mathcal{H}(\mathbf{R}) \tag{3.51}$$

$$
\begin{aligned}
\boldsymbol{\nabla}_{\widetilde{\Phi}}\mathcal{F}_H(\mathcal{H}) = -\sum_{mm'ss'll'\mu}\sqrt{\frac{m_{s'}}{m_s}}(\varepsilon_{s\mu\mathcal{H}}^{lm}\boldsymbol{\nabla}_{\widetilde{\Phi}}\ln a_{\mu\mathcal{H}} + \boldsymbol{\nabla}_{\widetilde{\Phi}}\varepsilon_{s\mu\mathcal{H}}^{lm})\varepsilon_{s'\mu\mathcal{H}}^{l'm'} \\
\times \int \mathrm{d}\mathbf{R}[f_s^{lm}(\mathbf{R}) - f_{s\mathcal{H}}^{lm}(\mathbf{R})](R_{s'}^{l'm'} - \tilde{R}_{s'}^{l'm'0})\rho_\mathcal{H}(\mathbf{R}). \tag{3.52}
\end{aligned}
$$

In these expressions $\mathbf{R} \equiv \{\mathbf{R}_1, ...\mathbf{R}_M\}$ is a general nuclear configuration. $\rho_{\mathcal{H}}(\mathbf{R})$ is the probability to find the system described by $\mathcal{H}$ in that general nuclear configuration $\mathbf{R}$, which in normal coordinates is a product of Gaussians. $a_{\mu\mathcal{H}} = \sqrt{\hbar\coth(\beta\hbar\omega_{\mu\mathcal{H}}/2)(2\omega_{\mu\mathcal{H}})}$ is called the normal length[1] of mode μ and is the standard deviation of the Gaussians. Finally, $\mathbf{f}(\mathbf{R})$ is the vector formed by all the atomic forces for the nuclear configuration $\mathbf{R}$ and $\mathbf{f}_{\mathcal{H}}(\mathbf{R})$ are the forces defined by $\mathcal{H}$. The only non-analytic terms in equations (3.50-3.52) are the integrals and, of course, the actual forces $\mathbf{f}(\mathbf{R})$.

The usual procedure for evaluating the integrals involves approaching to higher order coefficients in the Taylor expansion, which is a difficult and time-consuming task. In the SSCHA method, however, these integrals are evaluated stochastically. By using the relationship

$$\int d\mathbf{R}\mathcal{O}(\mathbf{R})\rho(\mathbf{R}) \simeq \frac{1}{N_c}\sum_{I=1}^{N_c}\mathcal{O}(\mathbf{R}_I) \equiv \langle\mathcal{O}\rangle, \tag{3.53}$$

we are able to convert the integral in a finite sum. The set of $\mathbf{R}_I$ configurations is created according to the distribution $\rho(\mathbf{R})$. $\mathcal{O}$ is any operator and N_c is the number of configurations we have created. One recovers the exact value for the integral in the limit $N_c \to \infty$. As we are dealing with a stochastic procedure, we have a statistical error scaling as $1/\sqrt{N_c}$. In return, this reduces the problem to calculating forces acting on atoms in supercells, which are easily extracted from electronic ground state calculations thanks to the Hellmann-Feynman theorem.

The minimization is worked out using a Conjugate-Gradient (CG) method and it is carried out in a subspace of the parameters that preserve crystal symmetries: $\widetilde{\Phi}$ and $\tilde{\mathbf{R}}^0$ are written on a symmetrized vector basis and the coefficients of such basis vectors are optimized. Therefore, depending on the system, we will obtain a different N_p number of independent coefficients to optimize. The flowchart in Fig. 3.1 summarizes the minimization process. An initial guess $\mathcal{H}_0$ (in the first step $j = 0$) is made for the trial Hamiltonian. A common procedure is to use the harmonic Hamiltonian obtained in a previous harmonic phonon calculation using DFPT, for instance, even though this cannot be used whenever the system is unstable in the harmonic approximation. This trial Hamiltonian is used to create N_c nuclear configurations according to $\rho_{\mathcal{H}_0}(\mathbf{R})$. The energy and atomic forces in each of the configurations are calculated in supercells[2]. Finally, we are able to evaluate the integrals in Eqs. (3.50-3.52) and perform a conjugate gradient step. This way, $\tilde{\mathbf{R}}^0$ and $\widetilde{\Phi}$ are updated so a new $\mathcal{H}_j$ is obtained.

---

[1]Even if it has dimensions of length times square root of mass.

[2]Using supercells to calculate atomic force constant matrices makes the Fourier transform provide the dynamical matrices in a $\mathbf{q}$-mesh of the same size as the supercell.
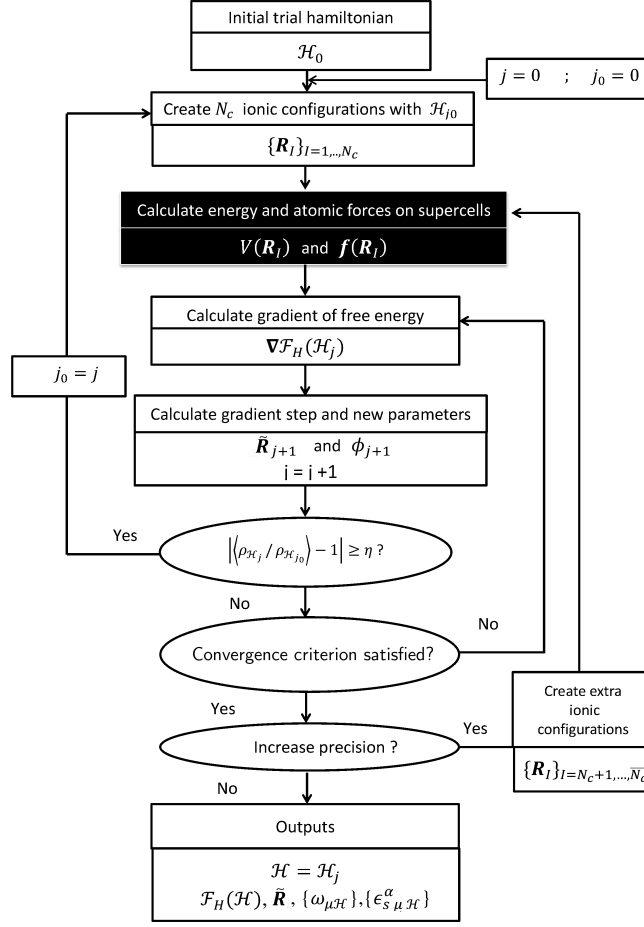
Figure 3.1: Flowchart of the SSCHA minimization process. The step marked in black, the calculation of forces in supercells, is the most time-demanding, and the program is optimized to call it as little as possible.

In principle, in order to perform a new cycle of the CG minimization new configurations should be created using the new $\rho_{\mathcal{H}_j}$. However, this would be very inefficient as electronic calculations in supercells are quite computationally demanding. Instead, a reweighting importance sampling technique is used, by correcting Eq. (3.53) as

$$\int d\mathbf{R}\mathcal{O}(\mathbf{R})\rho(\mathbf{R}) \simeq \frac{1}{N_c}\sum_{I=1}^{N_c}\mathcal{O}(\mathbf{R}_I)\frac{\rho_{\mathcal{H}_j}}{\rho_{\mathcal{H}_{j_0}}}, \qquad (3.54)$$

where j_0 is the latest iteration at which configurations were created. As long as $\langle\frac{\rho_{\mathcal{H}_j}}{\rho_{\mathcal{H}_{j_0}}}\rangle$ does not deviate substantially from unity, the configurations created with $\mathcal{H}_{j_0}$ can be reused. When the deviation is larger than a fixed parameter η new
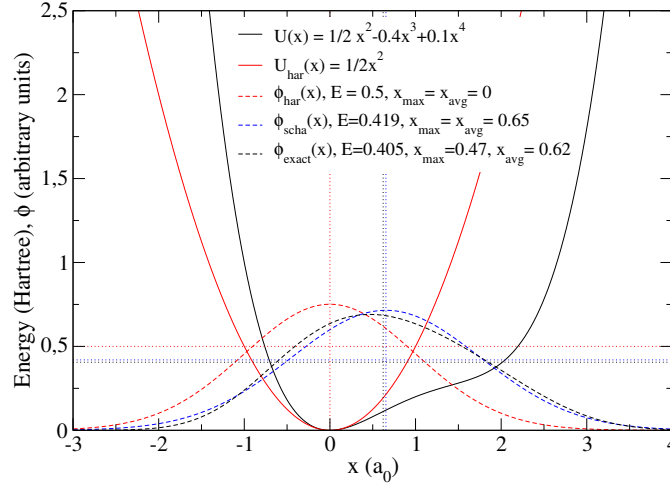
Figure 3.2: One dimensional example of the SCHA with arbitrary units for energy and displacement. The actual potential and the harmonic one are the black and red solid curves, respectively. The ground state harmonic, SSCHA (at zero temperature) and exact wavefunctions are shown with dashed curves. Dotted lines show the energy and the average position of each ground state wavefunction.

configurations have to be created with $\mathcal{H}_j$. The minimization stops when the chosen convergence criterion is satisfied. In our case we set a threshold value for the norm of the total gradient. One can always add extra configurations to reduce the statistical error and obtain the desired precision.

Figure 3.2 illustrates the aim of this theory with a simple one dimensional and zero temperature example were the density matrix in position representation reduces to the ground state wavefunction, which is a Gaussian curve. Imagine a real anharmonic potential, represented by a black curve in the figure, acts on a particle of unitary mass. In this particular case, the actual potential is known and we can solve the Schrödinger equation to obtain the exact ground state of the system, whose wavefunction is shown in dashed black. In the harmonic approximation (shown in red), the ground state wavefunction is just a Gaussian centered at the origin, whose standard deviation is just $\sqrt{1/\omega_0}\, a_0$ and the ground state energy is $E = \omega_0/2 = 1/2 = 0.5$ Hartree. In the SCHA we assume the wavefunction is a Gaussian and optimize its centroid position and standard deviation to minimize the vibrational energy. This leads to a wavefunction (blue curve) with a centroid position of 0.61 a_0 and a ground state energy of 0.41 Hartree, values much closer to the exact solutions, of 0.60 a_0 and 0.40 Hartree, respectively, than the harmonic ones (0.0 a_0 and 0.5 Hartree, respectively).

Chapter 4

The electron-phonon coupling

So far, we have considered electrons and phonons as fully independent systems. This means we assumed our total Hamiltonian was well approximated by just taking the Born-Oppenheimer Hamiltonian and neglecting ΔH in Eq. (1.11), which precisely accounts for how the nuclear motion affects the electronic structure of the system (and vice versa). For semi-conductors and insulators, where there is an electronic energy gap which is in general larger than the phonon frequencies, this assumption mostly holds; in the case of metals, where the gap is zero, it inevitably breaks down.

Let us write the Hamiltonian of the total system as

$$H_{tot} = H_{BO} + \Delta H. \tag{4.1}$$

For $|\alpha, \beta\rangle$ being any state of the system product of separate electronic and phonon parts in accordance to the adiabatic approximation (as defined in Eqs. 1.14 and 1.15), we can write the matrix elements of the total Hamiltonian as:

$$\langle \alpha', \beta' | H_{tot} | \alpha, \beta \rangle = E_{\alpha\beta} \delta_{\alpha\alpha'} \delta_{\beta\beta'} + \langle \alpha', \beta' | \Delta H | \alpha, \beta \rangle. \tag{4.2}$$

In Eq. 1.11 we can see ΔH is the sum of two terms, and so is any of its matrix elements:

$$\langle \alpha', \beta' | \Delta H | \alpha, \beta \rangle = \langle \alpha', \beta' | \sum_{ms} \frac{1}{m_s} [\mathbf{P}_{ms}]_I [\mathbf{P}_{ms}]_e | \alpha, \beta \rangle + \langle \alpha', \beta' | \sum_{ms} \frac{1}{2m_s} [\mathbf{P}_{ms}^2]_e | \alpha, \beta \rangle. \tag{4.3}$$

Let us assume $\langle \mathbf{x}; \mathbf{R}_m + \tau_s + \mathbf{u}_{ms} | \alpha \rangle = \psi_{e,\alpha}(\mathbf{x}; \mathbf{R}_m + \tau_s + \mathbf{u}_{ms})$ can be expanded in a power series of the atomic displacements $\mathbf{u}_{ms}$. While the first term in Eq. (4.3)

involves first order derivatives with respect to nuclear positions and, therefore, contributes at linear order in the displacement, the second term involves second order derivatives. Therefore, the first part is the important contribution and, thus, the electron-phonon interaction Hamiltonian can be limited to

$$H_{e-ph} = \sum_{ms} \frac{1}{m_s} [\mathbf{P}_{ms}]_e [\mathbf{P}_{ms}]_I, \tag{4.4}$$

and its matrix elements are separable in nuclear and electronic states:

$$\langle \alpha', \beta' | H_{ep} | \alpha, \beta \rangle = \sum_{ms} \frac{1}{m_s} \langle \beta' | \mathbf{P}_{ms} | \beta \rangle \langle \alpha' | \mathbf{P}_{ms} | \alpha \rangle . \tag{4.5}$$

The phonon part in momentum space can be immediately obtained by taking the matrix element $\langle \beta' | \mathbf{P}_{ms} | \beta \rangle$ and using the commutation relation $[H_I, \mathbf{u}_{ms}] = -\frac{i}{m_s} \mathbf{P}_{ms}$ and the bosonic ladder operators b and $b^\dagger$ as defined in Eq. 3.10[1]:

$$\begin{aligned}
\langle \beta' | \mathbf{P}_{ms} | \beta \rangle &= im_s(E_{\beta'} - E_\beta) \langle \beta' | \mathbf{u}_{ms} | \beta \rangle \\
&\qquad\qquad\qquad\qquad\qquad\qquad\qquad\qquad\qquad\qquad\qquad\qquad (4.6)\\
&= im_s(E_{\beta'} - E_\beta) \frac{1}{\sqrt{N_\mathbf{q}}} \sum_\mathbf{q}^{1BZ} \sum_\mu \frac{e^{i\mathbf{q}\cdot\mathbf{R}_m}}{\sqrt{2m_s\omega_{\mu\mathbf{q}}}} \boldsymbol{\varepsilon}_{s\mu\mathbf{q}} \langle \beta' | \left(b_{\mu\mathbf{q}} + b_{\mu-\mathbf{q}}^\dagger \right) | \beta \rangle .
\end{aligned}$$

Obtaining the electronic part is not straightforward, because the commutation relation $[H_I, \mathbf{u}_{ms}] = -\frac{i}{m_s} \mathbf{P}_{ms}$ does not hold for H^e. Using quantum perturbation theory we can write the perturbed electronic states to first order as $|\alpha\rangle \to |\alpha\rangle + |\Delta\alpha\rangle$, with

$$|\Delta\alpha\rangle = \sum_{\alpha'} \frac{\langle \alpha' | \Delta H_{ms}^e | \alpha \rangle}{E_\alpha^e - E_{\alpha'}^e} |\alpha'\rangle , \tag{4.7}$$

and the electronic states $|\alpha\rangle$ (and $|\alpha'\rangle$) referring to the equilibrium positions of the ions. In this context, the matrix element $\langle \alpha' | \mathbf{P}_{ms} | \alpha \rangle$ will only have a non-vanishing contribution for $\langle \alpha' | \mathbf{P}_{ms} | \Delta\alpha \rangle$. The change in the electronic Hamiltonian ΔH_{ms}^e caused by an atomic displacement $\mathbf{u}_{ms}$ can be expanded to linear order as $\Delta H_{ms}^e = \mathbf{u}_{ms} \cdot \nabla_{\mathbf{u}_{ms}} H^e$. Now we can rewrite the matrix element as

$$\begin{aligned}
\langle \alpha' | \mathbf{P}_{ms} | \alpha \rangle &= \langle \alpha' | \sum_{\alpha''} \frac{\langle \alpha'' | \mathbf{P}_{ms} \mathbf{u}_{ms} \cdot \nabla_{\mathbf{u}_{ms}} H^e | \alpha \rangle}{E_\alpha^e - E_{\alpha''}^e} |\alpha''\rangle = \\
&= -i \sum_{\alpha''} \delta_{\alpha'\alpha''} \frac{\langle \alpha'' | \nabla_{\mathbf{u}_{ms}} H^e | \alpha \rangle}{E_\alpha^e - E_{\alpha''}^e} = -i \frac{\langle \alpha' | \nabla_{\mathbf{u}_{ms}} H^e | \alpha \rangle}{E_\alpha^e - E_{\alpha'}^e}.
\end{aligned}$$

---

[1]From now on we will write the phonon wave vector dependence as a subindex, as in $\omega_{\mu\mathbf{q}} = \omega_\mu(\mathbf{q})$.

Given that within DFT $H^e(\mathbf{r}) = \sum\limits_{i}^{N} H^{KS}(\mathbf{r}_i)$, we can easily write $\nabla_{\mathbf{u}_{ms}} H^e$ in second quantization making use of the usual fermionic creation and annihilation operators,

$$\nabla_{\mathbf{u}_{ms}} H^e = \sum_{nn'} \sum_{\mathbf{k}\mathbf{k}'}^{1BZ} c_{n'\mathbf{k}'}^{\dagger} c_{n\mathbf{k}} \langle \phi_{n'\mathbf{k}'} | \nabla_{\mathbf{u}_{ms}} H^{KS} | \phi_{n\mathbf{k}} \rangle, \qquad (4.8)$$

where $c_{n\mathbf{k}}^{\dagger}$ creates and $c_{n\mathbf{k}}$ annihilates a Kohn-Sham state. Finally, the electronic part of the electron-phonon Hamiltonian reads as follows:

$$\langle \alpha' | \mathbf{P}_{ms} | \alpha \rangle = -i \frac{1}{E_\alpha^e - E_{\alpha'}^e} \sum_{nn'} \sum_{\mathbf{k}\mathbf{k}'}^{1BZ} \langle \phi_{n'\mathbf{k}'} | \nabla_{\mathbf{u}_{ms}} H^{KS} | \phi_{n\mathbf{k}} \rangle \langle \alpha' | c_{n'\mathbf{k}'}^{\dagger} c_{n\mathbf{k}} | \alpha \rangle. \quad (4.9)$$

Knowing that in a scattering process energy is conserved, $E_\alpha^e - E_{\alpha'}^e = E_{\beta'} - E_\beta$, we can write the total electron-phonon Hamiltonian as

$$H_{e-ph} = \sum_{ms} \sum_{nn'} \sum_{\mathbf{k}\mathbf{k}'\mathbf{q}}^{1BZ} \sum_{\mu} \frac{e^{i\mathbf{q}\cdot\mathbf{R}_m} \langle \phi_{n'\mathbf{k}'} | \nabla_{\mathbf{u}_{ms}} H^{KS} | \phi_{n\mathbf{k}} \rangle}{\sqrt{N_\mathbf{q} 2 m_s \omega_{\mu\mathbf{q}}}} \boldsymbol{\varepsilon}_{s\mu\mathbf{q}} \left(b_{\mu\mathbf{q}} + b_{\mu-\mathbf{q}}^{\dagger} \right) c_{n'\mathbf{k}'}^{\dagger} c_{n\mathbf{k}}.$$
$$(4.10)$$

Noting that the derivatives of the potential are periodic in real space and as momentum conservation can be extracted from $\sum_m e^{i\mathbf{q}\cdot\mathbf{R}_m} \langle \phi_{n'\mathbf{k}'} | \nabla_{\mathbf{u}_{ms}} H^{KS} | \phi_{n\mathbf{k}} \rangle$, the electron-phonon Hamiltonian can be rewritten in the Fröhlich way as

$$H_{e-ph} = \frac{1}{\sqrt{N_\mathbf{q}}} \sum_{\mu} \sum_{\mathbf{q}} \sum_{nn'} \sum_{\mathbf{k}}^{1BZ} g_{n'\mathbf{k}+\mathbf{q},n\mathbf{k}}^{\mu} c_{n'\mathbf{k}+\mathbf{q}}^{\dagger} c_{n\mathbf{k}} \left(b_{\mu\mathbf{q}} + b_{\mu-\mathbf{q}}^{\dagger} \right), \qquad (4.11)$$

where the electron-phonon coupling function is given by

$$g_{n'\mathbf{k}+\mathbf{q},n\mathbf{k}}^{\mu} = \sum_{m} \sum_{s} e^{i\mathbf{q}\cdot\mathbf{R}_m} \frac{1}{\sqrt{2 m_s \omega_{\mu\mathbf{q}}}} \langle \phi_{n'\mathbf{k}+\mathbf{q}} | \nabla_{\mathbf{u}_{ms}} H^{KS} \cdot \boldsymbol{\varepsilon}_{s\mu\mathbf{q}} | \phi_{n\mathbf{k}} \rangle. \qquad (4.12)$$

The Fröhlich Hamiltonian given in Eq. (4.11) describes the creation (annihilation) of a phonon mode that at the same time annihilates (creates) an electron-hole pair (see Fig. 4.1) and it is the basis for the many-body electron-phonon problem that drives, for example, the superconducting state. Luckily, once the electronic ground-state and phonon spectra have been calculated, H_{e-ph} can be obtained from DFPT following the procedure described in Section 3.3.
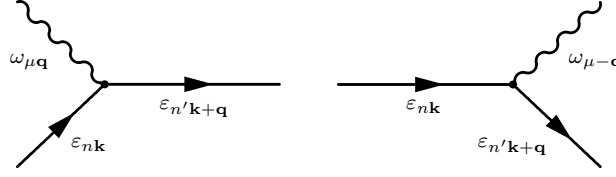
Figure 4.1: Diagrams that represent the interactions in H_{e-ph}. Straight and wiggling lines represent electrons and phonons, respectively, while time evolution is depicted from left to right. In the absorption diagram (left) energy conservation requires that $\varepsilon_{n\mathbf{k}} + \omega_{\mu\mathbf{q}} = \varepsilon_{n'\mathbf{k}+\mathbf{q}}$ while in the emission diagram (right) $\varepsilon_{n\mathbf{k}} = \omega_{\mu-\mathbf{q}} + \varepsilon_{n'\mathbf{k}+\mathbf{q}}$. Momentum is conserved in each interaction vertex.

4.1   Migdal-Eliashberg theory

Even though we have already defined the electron-phonon Hamiltonian, we have not deduced how it will affect the total wavefunction of the system yet. In fact, the electron-phonon interaction affects both the lattice dynamics and the electronic structure, which in turn alter the electron-phonon interaction itself. In order to properly account for this self-consistency we will use many-body perturbation theory and obtain both the electron and phonon Green functions, which will describe the excitations of the system or, in other words, how electronic and vibrational states are affected by the coupling of these two systems previously considered as independent under the Born-Oppenheimer approximation.

The starting point in all many-body problems is the Dyson equation [65, 106], which reads

$$G_n(\mathbf{k}, i\omega_m) = G_n^0(\mathbf{k}, i\omega_m) + G_n^0(\mathbf{k}, i\omega_m)\Sigma_n(\mathbf{k}, i\omega_m)G_n(\mathbf{k}, i\omega_m) \qquad (4.13)$$

for the electron Green function and

$$D_\mu(\mathbf{q}, i\Omega_m) = D_\mu^0(\mathbf{q}, i\Omega_m) + D_\mu^0(\mathbf{q}, i\Omega_m)\Pi_\mu(\mathbf{q}, i\Omega_m)D_\mu(\mathbf{q}, i\Omega_m) \qquad (4.14)$$

for the phonon Green function. In the equations above temperature is incorporated with the Matsubara complex frequency formalism and, therefore, the imaginary fermion $i\omega_m = i(2m-1)$ and boson $i\Omega_m = i2m$ frequencies need to be analytically continued to the real frequency (or energy) axis (i.e., $i\omega_n \to \varepsilon + i\eta$ and $i\Omega_n \to \omega + i\eta$ at zero temperature). The noninteracting electron Green function $G_n^0(\mathbf{k}, i\omega_m)$ can be written in terms of the eigenvalues of the one-electron effective electronic Hamiltonian (H^{KS} in the DFT formalism) as

$$G_n^0(\mathbf{k}, i\omega_m) = \frac{1}{i\omega_m - \varepsilon_{n\mathbf{k}}}, \qquad (4.15)$$

while the noninteracting phonon Green function $D_n^0(\mathbf{k}, i\omega_m)$ can be written in terms of the eigenvalues of the harmonic nuclear Hamiltonian (*i.e.* the phonon frequencies):

$$D_\mu^0(\mathbf{q}, i\Omega_m) = \frac{2\omega_{\mu\mathbf{q}}}{(i\omega_m)^2 - (\omega_{\mu\mathbf{q}})^2}.$$

(4.16)

This allows us to rewrite the Dyson equations as

$$G_n(\mathbf{k}, i\omega_m) = \frac{1}{i\omega_m - \varepsilon_{n\mathbf{k}} + \Sigma_n(\mathbf{k}, i\omega_m)}$$

$$D_\mu(\mathbf{q}, i\Omega_m) = \frac{2\omega_{\mu\mathbf{q}}}{(i\Omega_m)^2 - (\omega_{\mu\mathbf{q}})^2 + 2\omega_{\mu\mathbf{q}}\Pi_\mu(\mathbf{q}, i\Omega_m)}.$$

(4.17)

Finally, by following the diagrammatic representation in Fig. 4.2 the electron and phonon self-energies can be written formally from the standard Feynman rules [65][2] as

$$\Sigma_n(\mathbf{k}, i\omega_m) = -\frac{1}{N_{\mathbf{q}}\beta} \sum_\mu \sum_{\mathbf{q}}^{1BZ} \sum_{n'} \sum_{i\Omega_n} [g_{n'\mathbf{k}+\mathbf{q},n\mathbf{k}}^\mu]^* \tilde{g}_{n'\mathbf{k}+\mathbf{q},n\mathbf{k}}^\mu(i\omega_n, i\Omega_n)$$

$$\times \quad G_{n'}(\mathbf{k}+\mathbf{q}, i\omega_m + i\Omega_n) D_\mu(\mathbf{q}, i\Omega_m)$$

(4.18)

and

$$\Pi_\mu(\mathbf{q}, i\Omega_m) = \frac{1}{N_{\mathbf{k}}\beta} \sum_{nn'} \sum_{\mathbf{k}}^{1BZ} \sum_{i\omega_m} [g_{n'\mathbf{k}+\mathbf{q},n\mathbf{k}}^\mu]^* \tilde{g}_{n'\mathbf{k}+\mathbf{q},n\mathbf{k}}^\mu(i\omega_n, i\Omega_n)$$

$$\times \quad G_{n'}(\mathbf{k}+\mathbf{q}, i\omega_m + i\Omega_n) G_n(\mathbf{k}, i\omega_m),$$

(4.19)

respectively, where $\beta = 1/\kappa_B T$ is the inverse of temperature and $\tilde{g}_{n'\mathbf{k}+\mathbf{q},n\mathbf{k}}^\mu(i\omega_n, i\Omega_n)$ are the renormalized electron-phonon matrix elements due to the higher order terms of electron-phonon interaction, as well as due to scattering processes different than electron-phonon scattering as electron-electron or electron-impurity scatterings.

Electron and phonon self-energies constitute a set of coupled equations where the number of diagrams to be summed is infinite. Fortunately, the lowest order diagrams (see Fig.4.2), which are built by substituting the electron and phonon propagators by their noninteracting counterparts and by plugging $g_{nn'}^\mu(\mathbf{k}, \mathbf{q})$ instead of $\tilde{g}_{nn'}^\mu(\mathbf{k}, \mathbf{q}, i\omega_m, i\Omega_m)$, are expected to be a good approximation; according

---

[2]As we are neglecting spin degrees of freedom, the 2 factor in Eq. (4.19) is not present.
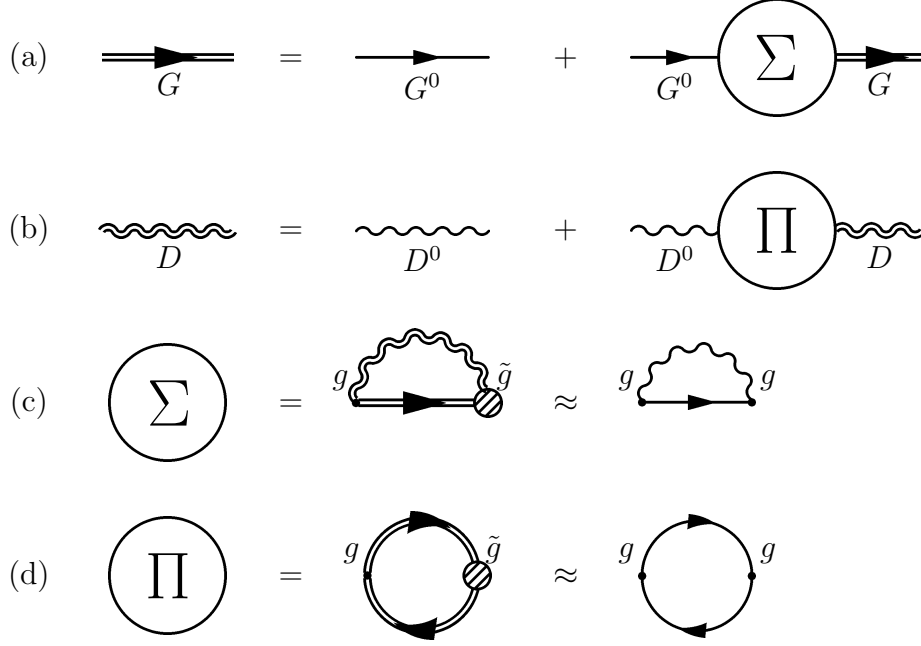
Figure 4.2: Pictorial representation using Feynman diagrams of the Dyson equation for the electron Green function (a) and the phonon Green function (b). The electron (c) and phonon (d) self-energies are shown in their exact form and in the Migdal approximation. In the diagrams a double straight line depicts the electron Green function, a single line the noninteracting electron Green function, a double wiggly line the phonon Green function, a single wiggly line the noninteracting phonon Green function, the dot the bare vertex shown in Fig. 4.1 and the shaded dot the renormalized vertex.

to Migdal's theorem, all vertex corrections will be of order $\sqrt{1/m_s}$ [107]. This way, we can decouple the expressions for the self-energies, which now read

$$
\begin{aligned}
\Sigma_n(\mathbf{k}, i\omega_m) &= -\frac{1}{N_\mathbf{q}\beta} \sum_\mu \sum_\mathbf{q}^{1BZ} \sum_{n'} \sum_{i\Omega_n} |g^\mu_{n'\mathbf{k}+\mathbf{q},n\mathbf{k}}|^2 G^0_{n'}(\mathbf{k}+\mathbf{q}, i\omega_m + i\Omega_n) \\
&\quad \times D^0_\mu(\mathbf{q}, i\Omega_m)
\end{aligned}
\tag{4.20}
$$

and

$$
\begin{aligned}
\Pi_\mu(\mathbf{q}, i\Omega_m) &= \frac{1}{N_\mathbf{k}\beta} \sum_{nn'} \sum_\mathbf{k}^{1BZ} \sum_{i\omega_m} |g^\mu_{n'\mathbf{k}+\mathbf{q},n\mathbf{k}}|^2 G^0_{n'}(\mathbf{k}+\mathbf{q}, i\omega_m + i\Omega_n) \\
&\quad \times G^0_n(\mathbf{k}, i\omega_m).
\end{aligned}
\tag{4.21}
$$

After performing the sum over Matsubara frequencies and continuing the functions analytically to real frequencies, the self-energies read[3]

$$
\Sigma_n(\mathbf{k}, \omega) = \frac{1}{N_{\mathbf{q}}} \sum_{\mu} \sum_{\mathbf{q}}^{1BZ} \sum_{n'} |g_{n'\mathbf{k}+\mathbf{q},n\mathbf{k}}^{\mu}|^2 \left[\frac{n_B(\omega_{\mu\mathbf{q}}) + \frac{1}{2} f_{n'\mathbf{k}+\mathbf{q}}}{\omega + i\delta + \omega_{\mu\mathbf{q}} - \varepsilon_{n'\mathbf{k}+\mathbf{q}}} \right.
$$
$$
\left. + \frac{n_B(\omega_{\mu\mathbf{q}}) + 1 - \frac{1}{2} f_{n'\mathbf{k}+\mathbf{q}}}{\omega + i\delta - \omega_{\mu\mathbf{q}} - \varepsilon_{n'\mathbf{k}+\mathbf{q}}} \right] \tag{4.22}
$$

$$
\Pi_\mu(\mathbf{q}, \omega) = \frac{1}{N_{\mathbf{k}}} \sum_{nn'} \sum_{\mathbf{k}}^{1BZ} |g_{n'\mathbf{k}+\mathbf{q},n\mathbf{k}}^{\mu}|^2 \frac{f_{n\mathbf{k}} - f_{n'\mathbf{k}+\mathbf{q}}}{\varepsilon_{n\mathbf{k}} - \varepsilon_{n'\mathbf{k}+\mathbf{q}} + \omega + i\delta}. \tag{4.23}
$$

The physical meaning of the self-energies is understood when taking the imaginary part of the Green functions which, when expressed in the real frequency axis, represent the electronic excitation and phonon spectra of the system under analysis. In this context, the real and imaginary parts of the self-energies are associated to the renormalization and linewidth, respectively, of the corresponding electron or phonon band. More interestingly, all relevant properties of the electron-phonon system are derived from these two equations.

In order to analyze the physical phenomena arising from the electron-phonon coupling we find useful to define the Eliashberg function as

$$
\alpha^2 F_n(\mathbf{k}, \omega, \Omega) = \frac{1}{N_{\mathbf{q}}} \sum_{\mathbf{q}} \sum_{\mu,n'} |g_{n'\mathbf{k}+\mathbf{q},n\mathbf{k}}^{\mu}|^2 \delta(\Omega - \omega_{\mu\mathbf{q}}) \delta(\omega - \varepsilon_{n'\mathbf{k}+\mathbf{q}}), \tag{4.24}
$$

with the electron self-energy adopting the following simple integral form:

$$
\Sigma_n(\mathbf{k}, \omega) = \int_{-\infty}^{\infty} d\omega' \int_0^{\infty} d\Omega \, \alpha^2 F_n(\mathbf{k}, \omega', \Omega) \left[\frac{n_B(\Omega) + \frac{1}{2} f(\omega')}{\omega - \omega' + i\delta + \Omega} + \right.
$$
$$
\left. + \frac{n_B(\Omega) + 1 - \frac{1}{2} f(\omega')}{\omega - \omega' + i\delta - \Omega} \right] \tag{4.25}
$$

Considering that all the relevant physics happen among the states at the Fermi level, the Eliashberg function can be averaged over the Fermi surface as

$$
\alpha^2 F(\Omega) = \frac{1}{N(\varepsilon_F) N_{\mathbf{k}}} \sum_{n} \sum_{\mathbf{k}}^{1BZ} \alpha^2 F_n(\mathbf{k}, \varepsilon_F, \Omega) \delta(\varepsilon_{n\mathbf{k}} - \varepsilon_F), \tag{4.26}
$$

---

[3]In Eq. (4.22) the $1/2$ factor in front of the f's is a consequence of the fact that we are including a $g = 2$ spin-degeneracy factor in the Fermi-Dirac distribution function. The phonon occupation number follows the Bose-Einstein distribution $n_B(\omega_{\mu\mathbf{q}}) = \frac{1}{e^{\omega_{\mu\mathbf{q}}/\kappa_B T} - 1}$

leading to

$$
\begin{aligned}
\alpha^2 F(\Omega) \;=\;& \frac{1}{N(\varepsilon_F)} \frac{1}{N_\mathbf{q} N_\mathbf{k}} \sum_{nn'} \sum_{\mathbf{kq}}^{1BZ} \sum_\mu |g^\mu_{n'\mathbf{k}+\mathbf{q},n\mathbf{k}}|^2 \delta(\Omega - \omega_{\mu\mathbf{q}}) \\
& \times \delta(\varepsilon_{n\mathbf{k}} - \varepsilon_F)\delta(\varepsilon_{n'\mathbf{k}+\mathbf{q}} - \varepsilon_F),
\end{aligned} \tag{4.27}
$$

with $N(\varepsilon_F) = \frac{1}{N_\mathbf{k}} \sum_{n\mathbf{k}} \delta(\varepsilon_{n\mathbf{k}} - \varepsilon_F)$ being the electronic density of states at the Fermi level.

From the last equation one can think of the Eliashberg function as a phonon density of states weighted by the strength of the electron-phonon coupling. In fact, after considering a few assumptions one can write this useful function in terms of the phonon linewidths, which are experimentally accessible and given by the imaginary part of the self-energy at the phonon frequency,

$$
\gamma_\mu(\mathbf{q}) = -\mathfrak{Im}\Pi_\mu(\mathbf{q}, \omega_{\mu\mathbf{q}}). \tag{4.28}
$$

Making use of the following

$$
\lim_{\delta \to 0} 1/(a \pm i\delta) = \mathcal{P}(1/a) \mp i\pi\delta(a) \tag{4.29}
$$

property,

$$
\gamma_\mu(\mathbf{q}) = \frac{\pi}{N_\mathbf{k}} \sum_{nn'} \sum_\mathbf{k}^{1BZ} |g^\mu_{n'\mathbf{k}+\mathbf{q},n\mathbf{k}}|^2 (f_{n\mathbf{k}} - f_{n'\mathbf{k}+\mathbf{q}})\delta(\varepsilon_{n\mathbf{k}} - \varepsilon_{n'\mathbf{k}+\mathbf{q}} + \omega_{\mu\mathbf{q}}). \tag{4.30}
$$

At temperatures much lower than the Fermi temperature (ε_f/κ_B) $f_{n\mathbf{k}} \approx 2\theta(\varepsilon_F - \varepsilon_{n\mathbf{k}})$ and, considering that the Dirac delta is the derivative of the step function and that phonon frequencies are much smaller than electron energies, it can be deduced that $f_{n\mathbf{k}} - f_{n'\mathbf{k}+\mathbf{q}} = 2[\theta(\varepsilon_F - \varepsilon_{n\mathbf{k}}) - \theta(\varepsilon_F - \varepsilon_{n'\mathbf{k}+\mathbf{q}})] \approx 2\omega_{\mu\mathbf{q}}\delta(\varepsilon_{n'\mathbf{k}+\mathbf{q}} - \varepsilon_F)$. The smallness of phonon frequencies compared to the electronic energies allows us to neglect the phonon frequency in the delta function of Eq. (4.30) as well, so the linewidth can be simplified to

$$
\gamma_\mu(\mathbf{q}) = \frac{2\pi\omega_{\mu\mathbf{q}}}{N_\mathbf{k}} \sum_{nn'} \sum_\mathbf{k}^{1BZ} |g^\mu_{n'\mathbf{k}+\mathbf{q},n\mathbf{k}}|^2 \delta(\varepsilon_{n'\mathbf{k}+\mathbf{q}} - \varepsilon_F)\delta(\varepsilon_{n\mathbf{k}} - \varepsilon_F). \tag{4.31}
$$

This means we just need to focus on excitations happening exclusively on the Fermi surface, as we actually recover the Eliashberg function averaged over the Fermi surface by combining Eqs. (4.31) and (4.27):

$$
\alpha^2 F(\omega) = \frac{1}{2\pi N(\varepsilon_F)N_\mathbf{q}} \sum_\mu \sum_\mathbf{q}^{1BZ} \frac{\gamma_\mu(\mathbf{q})}{\omega_{\mu\mathbf{q}}}\delta(\omega - \omega_{\mu\mathbf{q}}). \tag{4.32}
$$

This will be the procedure throughout this work to calculate the Eliashberg function. For convergence and numerical reasons, the delta functions in Eq. (4.31) are commonly substituted by Gaussians, whose width needs to be optimized.

As we will see later, the Eliashberg function is a key ingredient to investigate the electron-phonon coupling mediated superconductivity. However, electron-phonon coupling affects normal metals as well, as it modifies the electronic states distorting the band structure close to the Fermi energy. This alteration of the band-structure is usually represented by the electron-phonon coupling parameter or the sometimes called mass-enhancement parameter,

$$\lambda_n(\mathbf{k}) = -\mathfrak{Re}\left[\frac{\partial \Sigma_n(\mathbf{k}, \omega)}{\partial \omega}\right]_{\omega=0}, \tag{4.33}$$

which measures the distortion of the $n\mathbf{k}$ band close to the Fermi level due to the electron-phonon interaction. Actually, this is a key quantity for studying superconductors as well, even though a new formalism needs to be introduced to account for the creation of Cooper pairs and the consequent condensate: the Eliashberg formalism.

4.2 Eliashberg equations

So far we have dealt with a set of electrons and phonons that interact with each other, yielding a renormalization of electronic and vibrational spectra. However, in this work the electron-phonon coupling calculations will be addressed to determining the superconducting properties of the systems under analysis. In the superconducting state the system appears as a condensate formed by electron pairs known as Cooper pairs. In conventional superconductors the pairing mechanism is provided by the electron-phonon interaction. Eliashberg theory [108, 109], which extends BCS theory [110] beyond the weak coupling limit, is the appropriate method to reformulate the problem studied in Section 4.2 by accounting for the Cooper pairs.

Despite electrons usually repel each other due to the strong Coulomb repulsion, when being part of a metal a pair of electrons can gain attraction by exchanging phonons, even if this is not evident if one just looks at the Fröhlich Hamiltonian in the form (4.11). However, a canonical transformation and a perturbative expansion of the mentioned Hamiltonian leads to an expression which does not depend on
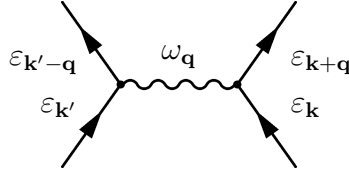
Figure 4.3: Diagrammatic representation of Eq. (4.34), which describes the phonon mediated effective electron-electron interaction responsible of the creation of Cooper pairs. The exchanged phonon is virtual as it propagates perpendicularly to time evolution and it is, therefore, infinitesimally short lived, allowing $|\varepsilon_{\mathbf{k}} - \varepsilon_{\mathbf{k}'+\mathbf{q}}| \neq \omega_{\mathbf{q}}$.

phonon creation and annihilation operators [65][4]:

$$\tilde{H}_{ep} = \sum_{\mathbf{kk}'}^{1BZ} \sum_{\mathbf{q}}^{1BZ} V_{eff}(\mathbf{k}, \mathbf{k}', \mathbf{q}) c_{\mathbf{k}+\mathbf{q}}^{\dagger} c_{\mathbf{k}'-\mathbf{q}}^{\dagger} c_{\mathbf{k}'} c_{\mathbf{k}} \qquad (4.34)$$

with

$$V_{eff}(\mathbf{k}, \mathbf{k}', \mathbf{q}) = g_{\mathbf{k}+\mathbf{q},\mathbf{k}} g_{\mathbf{k}'-\mathbf{q},\mathbf{k}'} \frac{\omega_{\mathbf{q}}}{|\varepsilon_{\mathbf{k}} - \varepsilon_{\mathbf{k}+\mathbf{q}}|^2 - \omega_{\mathbf{q}}^2}. \qquad (4.35)$$

This Hamiltonian describes the scattering of two electrons with momenta $\mathbf{k}$ and $\mathbf{k}'$ into states with momenta $\mathbf{k}+\mathbf{q}$ and $\mathbf{k}'-\mathbf{q}$ by the exchange of a virtual phonon with momentum $\mathbf{q}$ (see Fig. 4.3). If we look at the effective electron-electron interaction V_{eff} we see it becomes attractive when $|\varepsilon_{\mathbf{k}} - \varepsilon_{\mathbf{k}'+\mathbf{q}}| < \omega_{\mathbf{q}}$, potentially allowing two-electron bound states (Cooper pairs). Unfortunately, ordinary perturbation theory does not work in order to solve the eigenvalue problem with a Hamiltonian of the form $H = H^e + \tilde{H}_{ep}$ and V_{eff} adopting the form in Eq. 4.35. However, we can extract some conclusions which are crucial for solving this many-body problem:

- As total energy is preserved in a scattering process and as electron-electron attraction is limited to energy differences below phonon frequencies, only states existing within a shell of width ω_{max} (the maximum phonon frequency of the system) above the Fermi level will contribute to Cooper pair formation.

- The available $\mathbf{k}$-space for scattering processes that fulfill the condition above is maximum when the total momentum of the electron-pair is zero ($\mathbf{k}' = -\mathbf{k}$).

- Since in conventional superconductors Cooper pairs are expected to have a symmetric spatial wavefunction, they must adopt the singlet spin state with the constituting electrons having anti-parallel spins.

---

[4]Let us write it for a single electronic band and a single phonon branch for clarity.

With these considerations, the superconducting state can be defined as a macroscopic quantum state characterized by a coherent occupation of Cooper pairs, i.e., two-electron states with $(\mathbf{k}\uparrow, -\mathbf{k}\downarrow)$ where arrows denote spin up and down states. BCS theory uses the variational principle to find a new ground-state following the conditions above and simplifying the effective attraction potential as

$$V_{eff}(\mathbf{k}, \mathbf{k}', \mathbf{q}) = \begin{cases} -|C| & , \text{ for } |\varepsilon_{\mathbf{k}} - \varepsilon_{\mathbf{k}'+\mathbf{q}}| < \omega_{\mathbf{q}} \\ 0 & , \text{ otherwise }, \end{cases} \tag{4.36}$$

with C being a real number. Considered the most important theory regarding the field of superconductivity, BCS theory was able to explain the underlying physical mechanism as well as many properties of conventional superconductors. One of the most important results of the theory was the emergence of an energy gap ($2\Delta \approx 2\omega_D e^{-1/|C|N(\varepsilon_F)}$ at zero temperature) in the electronic excitation spectra of metals, responsible of the Meissner effect and lack of electrical resistivity, for instance. Interestingly, the gap decreases with increasing temperature until vanishing at T_c, the superconducting critical temperature.

However, BCS theory lacked of predictive power, specially for T_c, since $|C|$ had to be determined *a posteriori* and it did not work whenever the electron-phonon coupling was strong, as in lead or mercury. This was mainly because retardation effects were neglected by writing V_{eff} as an instantaneous interaction. Eliashberg theory [108], which extends Migdal's work [107] on normal metals to the superconducting state, overcomes the issues of BCS theory by appropriately rewriting the electronic Green function and self-energy and by considering the electron-phonon Hamiltonian in its original many-body Fröhlich form.

Eliashberg theory makes use of the so-called Nambu formalism [111], in which the two-electron Green function $\underline{G_n}(\mathbf{k}, i\omega_m)$ adopts the following 2×2 matrix form

$$\underline{G_n}(\mathbf{k}, i\omega_m) = \begin{pmatrix} G_n(\mathbf{k}, i\omega_m) & F(\mathbf{k}, i\omega_m) \\ F^*(\mathbf{k}, i\omega_m) & G_n(-\mathbf{k}, -i\omega_m) \end{pmatrix}, \tag{4.37}$$

in terms of the one-electron Green functions $G_n(\mathbf{k}, i\omega_m)$ and the anomalous Green functions $F(\mathbf{k}, i\omega_m)$, which will account for the creation of Cooper pairs, vanishing in the normal state. In this context the Dyson equation does not change, except that now the electron Green functions and the self-energy are matrices [5]:

$$\underline{G_n}^{-1}(\mathbf{k}, i\omega_m) = \underline{G_n^0}^{-1}(\mathbf{k}, i\omega_m) - \underline{\Sigma_n}(\mathbf{k}, i\omega_m), \tag{4.38}$$

with

$$\underline{G_n^0}(\mathbf{k}, i\omega_m) = (i\omega_m - \varepsilon_{n\mathbf{k}})^{-1}\underline{\tau_3} \tag{4.39}$$

---

[5] $\underline{\tau_0} = \begin{pmatrix} 1 & 0 \\ 0 & 1 \end{pmatrix}$, $\underline{\tau_1} = \begin{pmatrix} 0 & 1 \\ 1 & 0 \end{pmatrix}$, $\underline{\tau_1} = \begin{pmatrix} 0 & -i \\ i & 0 \end{pmatrix}$ and $\underline{\tau_3} = \begin{pmatrix} 1 & 0 \\ 0 & -1 \end{pmatrix}$

and

$$\underline{\Sigma}_n(\mathbf{k}, i\omega_m) = -\frac{1}{N_{\mathbf{q}}\beta}\sum_\mu\sum_{\mathbf{q}}^{1BZ}\sum_{n'}\sum_{i\omega_{m'}} g^\mu_{n'\mathbf{k}+\mathbf{q},n\mathbf{k}}\underline{\tau_3}\ \underline{G}_{n'}(\mathbf{k}+\mathbf{q}, i\omega_{m'})\ \underline{\tau_3}$$
$$\times g^\mu_{n\mathbf{k},n'\mathbf{k}-\mathbf{q}}D_\mu(\mathbf{q}, i\omega_{m'}-i\omega_m). \qquad (4.40)$$

If we write the electron self-energy in the general form

$$\underline{\Sigma}_n(\mathbf{k}, i\omega_m) = i\omega_m[1-Z_n(\mathbf{k}, i\omega_m)]\underline{\tau_0}+\chi_n(\mathbf{k}, i\omega_m)\underline{\tau_3}+$$
$$+ \Phi_n(\mathbf{k}, i\omega_m)\underline{\tau_1}+\tilde{\Phi}_n(\mathbf{k}, i\omega_m)\underline{\tau_2}, \qquad (4.41)$$

where Z_n, χ_n, Φ and $\tilde{\Phi}$ are yet unknown and real functions, using the Dyson equation the Green function can be written as

$$\underline{G}_n(\mathbf{k}, i\omega_m) = \frac{1}{\mathcal{D}_n(\mathbf{k}, i\omega_m)}[i\omega_m Z_n(\mathbf{k}, i\omega_m)\underline{\tau_0}+(\varepsilon_{n\mathbf{k}}+\chi_n(\mathbf{k}, i\omega_m))\underline{\tau_3}+$$
$$+ \Phi_n(\mathbf{k}, i\omega_m)\underline{\tau_1}+\tilde{\Phi}_n(\mathbf{k}, i\omega_m)\underline{\tau_2}], \qquad (4.42)$$

with

$$\mathcal{D}_n(\mathbf{k}, i\omega_m) = (i\omega_m Z_n(\mathbf{k}, i\omega_m))^2-(\varepsilon_{n\mathbf{k}}+\chi_n(\mathbf{k}, i\omega_m))^2-$$
$$- \Phi_n^2(\mathbf{k}, i\omega_m)-\tilde{\Phi}_n^2(\mathbf{k}, i\omega_m). \qquad (4.43)$$

Plugging Eq. (4.42) in (4.40) and separating the $\underline{\tau}$ components, one arrives at four

self-consistent equations for the four unknown functions Z_n, χ_n, Φ_n, and $\tilde{\Phi}_n$:

$$
\begin{aligned}
\omega_m(1 - Z_n(\mathbf{k}, i\omega_m)) &= -\frac{1}{N_\mathbf{q}\beta} \sum_{\mu,n',m'} \sum_{\mathbf{q}}^{1BZ} |g^\mu_{n'\mathbf{k}+\mathbf{q},n\mathbf{k}}|^2 D_\mu(\mathbf{q}, i\omega_{m'} - i\omega_m) \\
&\times \frac{\omega_{m'} Z_n(\mathbf{k}+\mathbf{q}, i\omega_{m'})}{\mathcal{D}_{n'}(\mathbf{k}+\mathbf{q}, i\omega_{m'})}
\end{aligned}
\tag{4.44}
$$

$$
\begin{aligned}
\chi_n(\mathbf{k}, i\omega_m) &= -\frac{1}{N_\mathbf{q}\beta} \sum_{\mu,n',m'} \sum_{\mathbf{q}}^{1BZ} |g^\mu_{n'\mathbf{k}+\mathbf{q},n\mathbf{k}}|^2 D_\mu(\mathbf{q}, i\omega_{m'} - i\omega_m) \\
&\times \frac{\varepsilon_{n'\mathbf{k}+\mathbf{q}} + \chi_{n'}(\mathbf{k}+\mathbf{q}, i\omega_{m'})}{\mathcal{D}_{n'}(\mathbf{k}+\mathbf{q}, i\omega_{m'})}
\end{aligned}
\tag{4.45}
$$

$$
\begin{aligned}
\Phi_n(\mathbf{k}, i\omega_m) &= \frac{1}{N_\mathbf{q}\beta} \sum_{\mu,n',m'} \sum_{\mathbf{q}}^{1BZ} |g^\mu_{n'\mathbf{k}+\mathbf{q},n\mathbf{k}}|^2 D_\mu(\mathbf{q}, i\omega_{m'} - i\omega_m) \\
&\times \frac{\Phi_{n'}(\mathbf{k}+\mathbf{q}, i\omega_{m'})}{\mathcal{D}_{n'}(\mathbf{k}+\mathbf{q}, i\omega_{m'})}
\end{aligned}
\tag{4.46}
$$

$$
\begin{aligned}
\tilde{\Phi}_n(\mathbf{k}, i\omega_m) &= \frac{1}{N_\mathbf{q}\beta} \sum_{\mu,n',m'} \sum_{\mathbf{q}}^{1BZ} |g^\mu_{n'\mathbf{k}+\mathbf{q},n\mathbf{k}}|^2 D_\mu(\mathbf{q}, i\omega_{m'} - i\omega_m) \\
&\times \frac{\tilde{\Phi}_{n'}(\mathbf{k}+\mathbf{q}, i\omega_{m'})}{\mathcal{D}_{n'}(\mathbf{k}+\mathbf{q}, i\omega_{m'})}
\end{aligned}
\tag{4.47}
$$

The equations above are the so-called Eliashberg equations and the physical meaning of the four unknown functions can be understood after writing the electronic quasiparticle energy, which are the poles of the Green function after analytic continuation, i.e., from $\mathcal{D}_n(\mathbf{k}, i\omega_m \to \omega + i\delta) = 0$. This gives

$$
E_{n,\mathbf{k}} = \sqrt{\frac{(\varepsilon_{n,\mathbf{k}} + \chi_n(\mathbf{k}, E_{n,\mathbf{k}}))^2}{Z_n^2(\mathbf{k}, E_{n,\mathbf{k}})} + \frac{\Phi_n^2(\mathbf{k}, E_{n,\mathbf{k}}) + \tilde{\Phi}_n^2(\mathbf{k}, E_{n,\mathbf{k}})^2}{Z_n^2(\mathbf{k}, E_{n,\mathbf{k}})}}.
\tag{4.48}
$$

One can see Z is the quasiparticle renormalization factor, χ describes shifts in the electron energies and the gap function is given by

$$
\Delta_n(\mathbf{k}, \omega) = \frac{\Phi_n(\mathbf{k}, \omega) - i\tilde{\Phi}_n(\mathbf{k}, \omega)}{Z_n(\mathbf{k}, \omega)}.
\tag{4.49}
$$

Thus, the superconducting state is characterized by a non-zero Φ or $\tilde{\Phi}$.

4.2.1   Isotropic approximation

The Eliashberg equations represent a complicated non-linear set of equations which couple all momenta $\mathbf{k}$ with each other. We will use the so-called isotropic equations instead, where the functions are averaged over the Fermi surface and only the frequency dependence remains. A very detailed derivation is given by Allen and Mitrovic [109], but here we only briefly explain the main assumptions leading to the final form.

- As in the normal state, the electron-phonon interaction produces a significant renormalization of quasiparticle energies only in a range $\pm\omega_{max}$ around the Fermi energy. Moreover, superconducting gaps are often very isotropic and, in real materials, defects tend to average anisotropic gaps [112].

- The shift in the electronic energies is usually small, and we therefore take $\chi = 0$.

- As Φ and $\tilde{\Phi}$ obey the same equations, they are expected to have the same functional form up to a common phase factor. Even though this phase factor can be important in some cases, as for the description of Josephson junctions, it is irrelevant for the thermodynamic properties of a homogeneous superconductor. In the following, we choose the simple gauge $\tilde{\Phi} = 0$.

- We ignore changes of the phonon quasiparticles and replace $D_\mu(\mathbf{q}, i\Omega_m)$ by the non-interacting Green function

$$D_\mu(\mathbf{q}, i\Omega_m) \to D_\mu^0(\mathbf{q}, i\Omega_m) = \int_0^\infty d\Omega\, \delta(\Omega - \omega_{\mu\mathbf{q}}) \frac{2\Omega}{(i\Omega_m)^2 - \Omega^2}. \qquad (4.50)$$

Under these conditions we can replace the quantities $Z_n(\mathbf{k}, i\omega_m)$ and $\phi_n(\mathbf{k}, i\omega_m)$ by their Fermi surface averages $Z(i\omega_m)$ and $\Phi(i\omega_m)$ and write the so called Eliashberg equations [109, 113][6]:

$$\omega_m(1 - Z_m) = -\pi T \sum_{m'} \Lambda_{m-m'} \frac{\omega_{m'} Z_{m'}}{[(\omega_{m'} Z_{m'})^2 + \phi_{m'}^2]^{1/2}}$$

$$\phi_m = \pi T \sum_{m'} \Lambda_{m-m'} \frac{\phi_{m'}}{[(\omega_{m'} Z_{m'})^2 + \phi_{m'}^2]^{1/2}},$$

(4.51)

---

[6]For simplicity, functions are written as: $f_n = f(i\omega_n)$

where the superconducting bandgap in the Matsubara axis is given by $\Delta_n = \frac{\phi_n}{Z_n}$. The frequency dependent electron-phonon coupling constant can be directly obtained from the Fermi surface averaged electron-phonon spectral function $\alpha^2 F(\omega)$:

$$\Lambda_{m-m'} = \int_0^\infty d\Omega \alpha^2 F(\Omega) \frac{2\Omega}{\Omega^2 + (\omega_m - \omega_{m'})^2}. \tag{4.52}$$

This even function takes its largest value at $\omega_m - \omega_{m'} = 0$,

$$\lambda = \Lambda_0 = 2 \int_0^\infty d\Omega \frac{\alpha^2 F(\Omega)}{\Omega}. \tag{4.53}$$

λ is called the (isotropic) electron-phonon coupling constant and is a dimensionless measure of the average strength of the electron-phonon coupling. In fact, it is just the Fermi surface average of the mass enhancement parameter shown in Eq. (4.33).

In order to calculate up to which temperature the superconducting condensate survives, the critical temperature T_c, one needs to solve the Eliashberg functions for different temperatures and check whether there's a solution with $\Delta_0 = \Delta(\Delta_0) > 0$ after analytically continuing the gap function. Practically, a Matsubara frequency cutoff is chosen such that $|\pi(2n-1)\pi T| \leq \Omega_c$ and the ME equations are solved using an iterative self-consistent loop by setting a threshold for either Δ_n in the superconducting state or Z_n in the normal state.

4.2.2   Coulomb repulsion and impurity effects

An important feature of the Eliashberg equations is that they only depend on normal-state properties: the electronic band structure, phonons, and the electron-phonon coupling vertices, quantities which are accessible to first principles techniques. Moreover, because $\alpha^2 F(\omega)$, as defined in Eq. (4.27), is a positive function, Eliashberg equations always possess a superconducting solution for low enough temperatures, meaning all metals would be superconductors below a certain temperature.

Our derivation up to now was based on the Fröhlich Hamiltonian, where the electronic subsystem is approximated by bands of noninteracting quasiparticles ignoring any Coulomb interaction, as repulsion between electrons was already considered using a mean-field approach (DFT in our case). However, the interaction among the electron quasiparticles cannot be completely neglected in the discussion of phonon-mediated superconductivity, as it tends to reduce or even completely suppress the pairing. It was shown by Morel and Anderson [112] that the Coulomb repulsion can be taken into account by replacing the kernel just in the gap equation

by

$$\Lambda_{m-m'} \rightarrow [\Lambda_{m-m'} - \mu^*]\theta(\omega_c - |\omega'_m|). \tag{4.54}$$

In practice, the so-called Coulomb pseudopotential μ^* is commonly treated as a phenomenological dimensionless parameter of the order of 0.1 for normal metals.

On the other hand, we have not included the effects of elastic impurity scattering in the Eliashberg equations. We can in fact easily introduce impurity scattering in the equations by replacing the spectral function in both equations by

$$\alpha^2 F(\omega) \rightarrow \alpha^2 F(\omega) + \alpha_{imp}^2 F(\omega), \tag{4.55}$$

with

$$\alpha_{imp}^2 F(\omega) = \frac{\omega}{2\pi T \tau_{imp}}\delta(\omega). \tag{4.56}$$

If we consider the substitutions shown above, the Eliashberg equations can be rewritten as

$$\omega_m(1 - Z_m) = -\sum_{m'}[\pi T \Lambda_{m-m'} + \frac{1}{2\tau_{imp}}\delta_{m,m'}]\frac{\omega_{m'} Z_{m'}}{[(\omega_{m'} Z_{m'})^2 + \phi_{m'}^2]^{1/2}}$$

$$\tag{4.57}$$

$$\phi_m = \sum_{m'}[\pi T(\Lambda_{m-m'} - \mu^*) + \frac{1}{2\tau_{imp}}\delta_{m,m'}]\frac{\phi_{m'}}{[(\omega_{m'} Z_{m'})^2 + \phi_{m'}^2]^{1/2}}.$$

In this thesis we have solved the equations above mostly in order to obtain T_c values of different materials, but also for obtaining the gap and renormalization functions, which provide crucial information about the excitations of the system (i.e. to obtain optical reflectivity spectra, as we will see in Chapter 8). In order to solve the equations, a *FORTRAN* code has been written from scratch.

4.3   McMillan equation

When the electron-phonon coupling is weak ($\lambda < 1$), instead of solving the Eliashberg equations a simpler approach can be taken by using the McMillan equation [114] improved by Dines [115]:

$$T_c = \frac{\omega_{log}}{1.2}\exp\left(-\frac{1.04(1 + \lambda)}{\lambda - \mu^*(1 + 0.62\lambda)}\right), \tag{4.58}$$

with the logarithmic frequency average, ω_{log}, reading as

$$\omega_{log} = \exp\left(\frac{2}{\lambda}\int_0^\infty \mathrm{d}\omega\ \frac{\alpha^2 F(\omega)}{\omega}\ln\omega\right). \qquad (4.59)$$

Although Eq. (4.58) is an equation based on quantities averaged on the Fermi surface, it generally yields results in agreement with experiments [113] and is even used in systems with anisotropic Fermi surfaces [116, 117].

Chapter 5

Time-dependent density functional theory

In Section 3.2 we described phonons in terms of a time-independent density-response function χ, assuming the electrons adapt instantaneously to the changing ionic positions. Later, in Section 3.3 we overcame the cumbersome calculation of χ by using DFPT, after which we included non-adiabatic (time-dependent) effects by considering the electron-phonon coupling in a perturbative way as well in Chapter 4. This approach is valid in order to account for lattice dynamics and the effects of electron-phonon interaction in both the electronic and the vibrational spectra. However, systems are often characterized after being excited by some incident external beam; the difference between the incident beam and the scattered one provides information about the excitations of the system. The potential induced by the external probe will be, in general, time-dependent and, therefore, the electronic density will depend on time. Interestingly, collective excitations may exist even in the absence of an external probe, such as plasmons, which cannot be represented with conventional DFT. In order to tackle these problems with oscillating frequencies we will use an expansion of DFT, the so called linear response time-dependent density-functional theory (linear response TDDFT).

Let us consider an interacting many electron system under a time-dependent external potential

$$V_{ext}(\mathbf{x}, t) = V_{ext}(\mathbf{x}) + \Phi^{ext}(\mathbf{x}, t), \tag{5.1}$$

where $V_{ext}(\mathbf{x})$ is the potential created by the ions and $\Phi^{ext}(\mathbf{x}, t)$ the potential created by a general external probe. As Runge and Gross showed [118], the final density $n(\mathbf{x}, \mathbf{R}, t)$ becomes a functional of the potential and, as the relation can be inverted, the potential itself becomes a functional of the density. This is an

analogous time dependent version of the first Hohenberg-Kohn theorem.

The key of TDDFT is that the theorem also holds for a system of non-interacting Kohn-Sham electrons moving in an effective time-dependent potential

$$V^{KS}(\mathbf{x}, t) = V_{ext}(\mathbf{x}, t) + V_H(\mathbf{x}, t) + V_{xc}(\mathbf{x}, t), \tag{5.2}$$

where the time-dependent Hartree potential is

$$V_H(\mathbf{x}, t) = \int \mathrm{d}\mathbf{x}' \, \frac{n(\mathbf{x}', t)}{|\mathbf{x} - \mathbf{x}'|} \tag{5.3}$$

and $V_{xc}(\mathbf{x}, t)$ is the time-dependent exchange-correlation potential [119, 120].

Taking into account such functional relations, and assuming a causal relation between the induced density and the external probe, the time-dependent density response function can be written as

$$\chi(\mathbf{x}, \mathbf{x}', t - t') = \frac{\delta n(\mathbf{x}, t)}{\delta V_{ext}(\mathbf{x}', t')}, \tag{5.4}$$

while in the non-interacting case

$$\chi^0(\mathbf{x}, \mathbf{x}', t - t') = \frac{\delta n(\mathbf{x}, t)}{\delta V^{KS}(\mathbf{x}', t')}. \tag{5.5}$$

As we saw for the time-independent case, the interacting and non-interacting response functions are related to each other by a Dyson-type equation [119],

$$
\begin{aligned}
\chi(\mathbf{x}, \mathbf{x}', t - t') &= \chi^0(\mathbf{x}, \mathbf{x}', t - t') + \int_{-\infty}^{\infty} \mathrm{d}t_1 \mathrm{d}t_2 \int \mathrm{d}\mathbf{x}_1 \mathrm{d}\mathbf{x}_2 \, \chi^0(\mathbf{x}, \mathbf{x}_1, t - t_1) \\
&\quad \times \left[\frac{\delta(t_1 - t_2)}{|\mathbf{x}_1 - \mathbf{x}_2|} + f^{xc}(\mathbf{x}_1, \mathbf{x}_2, t_1 - t_2) \right] \chi(\mathbf{x}_2, \mathbf{x}', t_2 - t').
\end{aligned}
\tag{5.6}
$$

The time-dependent exchange-correlation kernel is defined according to

$$f^{xc}(\mathbf{x}, \mathbf{x}', t - t') = \frac{\delta V_{xc}(\mathbf{x}, t)}{\delta n(\mathbf{x}', t')}. \tag{5.7}$$

Since $\chi(\mathbf{x}, \mathbf{x}', t - t')$ and $\chi_0(\mathbf{x}, \mathbf{x}', t - t')$ are periodic in real space for any lattice translation, their momentum components $\chi(\mathbf{k}, \mathbf{k}', t - t')$ and $\chi_0(\mathbf{k}, \mathbf{k}', t - t')$ are zero unless $\mathbf{k}$ and $\mathbf{k}'$ differ by a reciprocal lattice vector $\mathbf{G}$. Thus, adopting the matrix notation $f_{\mathbf{GG}'}(\mathbf{k}) = f(\mathbf{k} + \mathbf{G}, \mathbf{k} + \mathbf{G}')$, and by Fourier transforming in

time coordinates as well, we can expand $\chi(\mathbf{x}, \mathbf{x}', t - t')$ in its $\chi_{\mathbf{GG'}}(\mathbf{k}, \omega)$ Fourier components as

$$\chi(\mathbf{x}, \mathbf{x}', t - t') = \frac{1}{N_\mathbf{k}\Omega_{BZ}} \sum_\mathbf{k}^{1BZ} \sum_{\mathbf{GG'}} \int_{-\infty}^{\infty} d\omega \; e^{i(\mathbf{k}+\mathbf{G})\cdot\mathbf{x}} e^{-i(\mathbf{k}+\mathbf{G'})\cdot\mathbf{x'}} e^{i\omega(t-t')} \chi_{\mathbf{GG'}}(\mathbf{k}, \omega),$$

(5.8)

which also holds for χ_0. In Fourier space, Eq. (5.6) becomes a simple matrix equation for each $\mathbf{k}$ and ω,

$$
\begin{aligned}
\chi_{\mathbf{GG'}}(\mathbf{k}, \omega) &= \chi^0_{\mathbf{GG'}}(\mathbf{k}, \omega) + \sum_{\mathbf{G_1}\mathbf{G_2}} \chi^0_{\mathbf{GG_1}}(\mathbf{k}, \omega) \\
&\times \left[\frac{4\pi}{|\mathbf{k} + \mathbf{G_1}|^2} \delta_{\mathbf{G_1}\mathbf{G_2}} + f^{xc}_{\mathbf{G_1}\mathbf{G_2}}(\mathbf{k}, \omega) \right] \chi_{\mathbf{G_2}\mathbf{G'}}(\mathbf{k}, \omega),
\end{aligned}
$$

(5.9)

where the reciprocal lattice vectors serve as the indexes of the matrices. Adopting the same matrix notation for the Fourier transform of the exchange-correlation kernel $K_{\mathbf{G_1}\mathbf{G_2}}(\mathbf{k}, \omega) = 4\pi \delta_{\mathbf{G_1}\mathbf{G_2}}/|\mathbf{k} + \mathbf{G_1}|^2 + f^{xc}_{\mathbf{G_1}\mathbf{G_2}}(\mathbf{k}, \omega)$, the interacting density response matrix can be obtained from

$$\chi = (1 - \chi^0 K)^{-1}\chi^0.$$

(5.10)

Hence, in order to calculate χ one needs to estimate the noninteracting response matrix and, then, invert $1 - \chi^0 K$.

The non-interacting response function can be calculated from the single-particle Kohn-Sham states as [71, 121, 122]

$$
\begin{aligned}
\chi^0_{\mathbf{GG'}}(\mathbf{k}, \omega) &= \frac{1}{\Omega} \sum_{\mathbf{k'}}^{1BZ} \sum_{nm} \frac{f_{n\mathbf{k'}} - f_{m\mathbf{k'}+\mathbf{k}}}{\varepsilon_{n\mathbf{k'}} - \varepsilon_{m\mathbf{k'}+\mathbf{k}} + \omega + i\eta} \\
&\times \langle \phi_{n\mathbf{k'}} | e^{-i(\mathbf{k}+\mathbf{G})\cdot\mathbf{x}} | \phi_{m\mathbf{k'}+\mathbf{k}} \rangle \langle \phi_{m\mathbf{k'}+\mathbf{k}} | e^{i(\mathbf{k}+\mathbf{G'})\cdot\mathbf{x}} | \phi_{n\mathbf{k'}} \rangle,
\end{aligned}
$$

(5.11)

where η is a positive infinitesimal which insures that the response function is causal or, if preferred, is the retarded response function.

Moreover, considering that $\chi^0_{\mathbf{GG'}}(\mathbf{k}, \omega)$ is analytic in the upper complex half-plane, the useful Kramers-Kronig relations can be derived [71]:

$$\mathfrak{Re}\chi^0_{\mathbf{GG'}}(\mathbf{k}, \omega) = -\frac{1}{\pi} \int_{-\infty}^{\infty} d\omega' \mathfrak{Im}\chi^0_{\mathbf{GG'}}(\mathbf{k}, \omega') \mathcal{P}\left(\frac{1}{\omega - \omega'}\right)$$

(5.12)

$$\mathfrak{Im}\chi^0_{\mathbf{GG'}}(\mathbf{k}, \omega) = \frac{1}{\pi} \int_{-\infty}^{\infty} d\omega' \mathfrak{Re}\chi^0_{\mathbf{GG'}}(\mathbf{k}, \omega') \mathcal{P}\left(\frac{1}{\omega - \omega'}\right),$$

(5.13)

where $\mathcal{P}$ denotes the principal value. Kramers-Kronig relations are a consequence of the causality of the response function and relate its real and imaginary parts. Thus, it suffices to calculate one of the terms (the usual procedure is to calculate $\mathfrak{Im}\chi^0_{\mathbf{GG}'}$ with TDDFT), as the other term can be obtained by using the mentioned relations.

Once the density response function of the system has been obtained, the inverse dielectric matrix can be written as

$$\epsilon^{-1}_{\mathbf{GG}'}(\mathbf{k},\omega) = \delta_{\mathbf{GG}'} + \frac{4\pi}{|\mathbf{k}+\mathbf{G}|^2}\chi_{\mathbf{GG}'}(\mathbf{k},\omega). \tag{5.14}$$

The inverse dielectric function relates the induced (screened) field and external field as

$$\Phi^{ind}_{\mathbf{G}}(\mathbf{k},\omega) = \sum_{\mathbf{G}'}\epsilon^{-1}_{\mathbf{GG}'}(\mathbf{k},\omega)\Phi^{ext}_{\mathbf{G}'}(\mathbf{k},\omega). \tag{5.15}$$

The non-diagonal elements of the matrix are often named as the crystal local-field effects (CLFE), which appear because translational symmetry is reduced to a discrete symmetry under translations by lattice vectors [121]. In the case of an homogeneous electron gas with full translational symmetry the inverse dielectric matrix is diagonal [71].

Inverting Eq. (5.15) one obtains

$$\Phi^{ext}_{\mathbf{G}}(\mathbf{k},\omega) = \sum_{\mathbf{G}'}\epsilon_{\mathbf{GG}'}(\mathbf{k},\omega)\Phi^{ind}_{\mathbf{G}'}(\mathbf{k},\omega), \tag{5.16}$$

with the dielectric matrix being the inverse of Eq. (5.14). Interestingly, there is a nontrivial solution of Eq. (2.6) even in the absence of an external field ($\Phi^{ext} = 0$) whenever $\det \epsilon(\mathbf{k},\omega) = 0$. These solutions are known as plasmons, and they are defined as an oscillating electronic potential that is set up without the application of an external field [122].

In this thesis we are interested in the zero-momentum transfer limit, as we will use TDDFT for obtaining reflectivity spectra for normal incident light. Reflectivity of a material for normal incident light in a medium with refractive index n can be written as

$$R(\omega) = \left|\frac{\sqrt{\epsilon(\omega)}-n}{\sqrt{\epsilon(\omega)}+n}\right|^2, \tag{5.17}$$

with $\epsilon(\omega) \equiv \lim_{\mathbf{k}\to 0}\epsilon_{00}(\mathbf{k},\omega)$ being the so-called frequency dependent dielectric function, notation that will be used throughout the results shown in Chapter 8. We find important to point out that, unless the CLFE are negligible, generally

$\epsilon_{00}(\mathbf{k}, \omega) \neq [\epsilon_{00}^{-1}(\mathbf{k}, \omega)]^{-1}$. Therefore, one needs to invert $\epsilon_{00}^{-1}(\mathbf{k}, \omega)$ and take the $< 00 >$ element of the resulting matrix.

Even though TDDFT is an exact theory, similar to DFT, the time-dependent exchange-correlation kernel is unknown and it needs to be approximated. In this work, among the different kernels available in literature [123], the time-dependent local-density approximation (TDLDA) is used to approximate the many-body effects.

The TDLDA is a local and time-independent expansion of the RPA based on the static LDA exchange-correlation potential. Indeed,

$$f_{TDLDA}^{xc}(\mathbf{x}, \mathbf{x}', t - t') = \delta(\mathbf{x} - \mathbf{x}') \left[\frac{\mathrm{d}^2 (n\varepsilon_{xc}^{hom}(n))}{\mathrm{d}n^2} \right]_{n(\mathbf{x})}, \qquad (5.18)$$

where ε_{xc}^{hom} is given in Section 2.21. Despite being more complex than the RPA, which consists of taking $f_{RPA}^{xc}(\mathbf{x}, \mathbf{x}', t - t') = 0$, most of the times it corrects only very slightly the RPA results [124]. However, while in general terms both RPA and TDLDA describe accurately optical properties of metals due to their screening capability, sometimes effects beyond RPA may be important.

Part II

Solid metallic hydrogen

High pressure hydrogen has been of scientific interest for a long time, being solid hydrogen first documented back in 1899 [125]. Despite molecular and insulating in its common gaseous state, its position on the periodic table suggests it could, once condensed and under certain conditions, adopt a metallic form similar to the alkalis. In 1935 Wigner and Huntington predicted hydrogen molecules would dissociate at around 25 GPa yielding a metallic compound [14]. Despite a huge experimental effort in the last years has characterized the phase diagram of hydrogen even beyond 400 GPa [126, 126–137], metallic hydrogen has remained elusive. However, the long standing quest might have come to an end as, early in 2017, Dias and Silvera reported the first ever laboratory-produced sample of solid metallic hydrogen at 495 GPa [138].

We find convenient to note that there are two pathways to obtain metallic hydrogen at static pressures (see Fig. 5.1). The first (pathway I) is to compress hydrogen along a quasi-isotherm at temperatures below 400 K until the insulator-metal transition occurs. This is, in fact, what Wigner and Huntington predicted [14] and Dias and Silvera claimed to have achieved in Ref. [138]. The second path to metallize hydrogen (pathway II) consists of increasing the temperature at almost constant pressure (typically around 150 GPa) beyond its melting point and further up until the molecules dissociate into a partially ionized metallic monoatomic liquid after the so-called plasma phase transition [139]. This region of the phase diagram belongs to hot-dense matter and it has been widely analyzed theoretically [129, 139–142] as well as with both static and shockwave experiments [143–146]. Even though this is of tremendous interest to plasma and planetary scientists, as these are the conditions found in the giant gaseous planets and exoplanets, in this thesis we will focus on the low temperature metallization of hydrogen instead, which we find more interesting from the point of view of materials science.

The interest of solid metallic hydrogen for materials scientists grew exponentially when in 1968 Neil Ashcroft predicted a superconducting T_c of nearly room temperature for high pressure hydrogen [15]. In fact, recent *ab initio* predictions support this statement and estimate hydrogen may superconduct even at ambient temperatures above 400 GPa [147–150], which would make hydrogen the best superconductor ever observed. The measurement of a T_c of 203 K in the sulfur hydrogen system [16], a temperature reachable on Earth's surface, was a major breakthrough in the field of superconductivity and validated Ashcroft's idea that hydrogen and hydrogen-dominant metallic compounds can be high-temperature superconductors [15, 151]. This measurement, specially after Dias and Silvera's controversial claim of having produced a metallic hydrogen sample [138], offers new hopes to find sooner than later room-temperature superconductivity in other hydrogen-rich compounds or hydrogen itself.
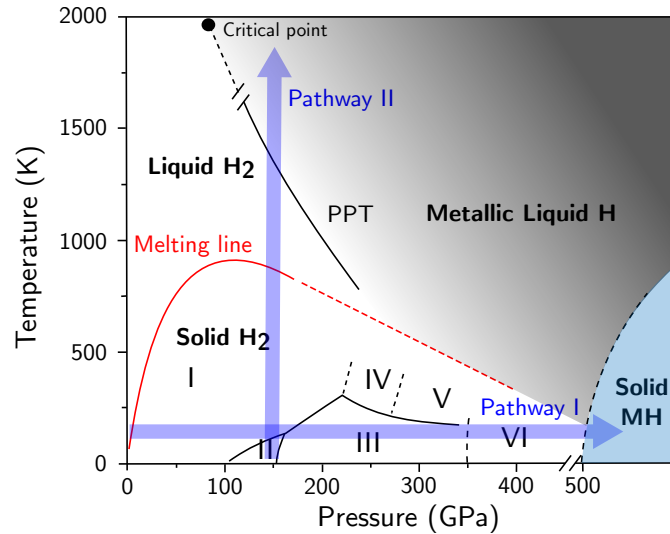
Figure 5.1: Experimental/theoretical pressure vs. temperature phase diagram of hydrogen. It shows the two pathways to metallic hydrogen: I the low temperature pathway and II the high temperature pathway. In pathway I phases of solid hydrogen are shown with their Latin number names. The plasma phase transition (PPT) is the liquid-liquid transition to metallic atomic hydrogen. Dashed lines emphasize uncertainty in the phase boundaries. This graph has been adapted from Ref. [138].

Despite the fact that these predictions and hypotheses may look promising, lots of experimental and theoretical work are still necessary. With the latest developed DACs it is possible to obtain pressures potentially up to 600 GPa [34]. As most of the properties of a material are critically influenced by the structure of its condensed phases, structural characterization is crucial. However, due to the weak cross-section of hydrogen against X-ray radiation and the difficulties to obtaining samples big enough for neutron diffraction experiments for the DAC technology, determining the structures of hydrogen is a huge experimental challenge. These limitations imposed on conventional techniques make the use of alternative techniques imperative. Nowadays, most of the available experimental data comes from infrared (IR) and Raman measurements that give us information about the vibrational properties of high pressure hydrogen at the Γ point. The way for determining a phase transition is to follow the vibrational modes' (as a molecular vibron) frequencies when changing the pressure and temperature. Thus, a phase transition will lead to an abrupt change of the frequencies of the modes. On the other hand, the latest claim of having produced metallic hydrogen in a lab relies on reflectance experiments [138], suggesting optical measurements could also be an alternative for characterizing high pressure hydrogen.

Raman and IR data are not, on their own, enough to characterize the phases of hydrogen and comparison with theoretical predictions becomes crucial to understand the phase diagram. In fact, the way to determine the crystal structure of each phase is by comparing the measured vibrational spectra to calculations on candidate structures. However, the theoretical study of such a light element turns out to be difficult due to the large nuclear quantum effects. Even at $T = 0$ K fluctuations of nuclear positions due to Heisenberg's indetermination principle could energetically favor some structures against others, as well as even melt the crystal into a liquid. Actually, metallic and superconducting hydrogen could also appear in a quantum liquid state under certain conditions [129, 152, 153]. Quantum fluctuations may lead to huge anharmonic effects even down to absolute zero temperature as zero point motion can cause large atomic displacements due to the lightness of hydrogen atoms. As a consequence, the change in frequencies and free energies due to anharmonic effects could alter the relative stability among different structures. Actually, the influence of anharmonic effects in the stability goes beyond a purely energetic discussion knowing that imaginary frequencies at phonon spectra are fingerprints of instabilities in crystals. Furthermore, phonon frequency renormalization due to anharmonicity may have an impact in the large T_c values predicted for hydrogen [147–150, 154–156], as seen in many hydrides [93, 94, 102, 103, 157, 158]. Considering that in aluminum [157, 158], palladium [94], and platinum hydrides [93], as well as in the record superconductor H_3S [102] anharmonicity suppresses the electron-phonon couping as it tends to harden optical H-character phonon modes, one might expect that anharmonicity might strongly impact superconductivity in hydrogen too. The SSCHA is the appropriate tool for including anharmonic effects in *ab initio* simulations, and it will be intensively used throughout this chapter to estimate their consequent structural and spectral renormalizations.

Thus far, five solid phases of hydrogen have been confirmed, all of them molecular and insulating. Only phase I and phase II, which are the lowest pressure solid phases of hydrogen, have been characterized by X-ray and neutron scattering experiments. Phase I is thought to be a molecular solid of quantum rotors on a hexagonal close packed lattice [127]. It is found in a wide pressure and temperature range up to the melting curve, which has a maximum of ∼1000 K around 65 GPa [128, 129]. Phase II appears between approximately 50-150 GPa and only below 150 K, temperature at which it transforms back to phase I [130, 159]. The phase I to phase II transformation is described as a broken symmetry phase transition, in which the molecules go from a spherical rotational state to an anisotropic rotational state [159]. The other phases have been found by Raman and IR measurements and, therefore, the information about their crystal structure is limited to finding a candidate structure that fits best the measured vibrational spectra.

Hydrogen adopts phase III above 150 GPa up to at least 360 GPa [131, 132] and it is best modeled by a candidate structure with symmetry $C2/c$ [160]. Recent experiments have determined that this phase transforms to phase IV at around 200 K in the 240-325 GPa pressure range [126, 133, 134], which might melt close to room temperature [135]. Transition from phase IV to V occurs at 325 GPa, the last one existing probably up to the dissociation pressure [137]. The candidate structures for phases IV and V are the mixed molecular-atomic phases predicted by Pickard and Needs [160, 161].

Recently, new phases have been claimed to be found as experimental researchers have been able to reach pressures up to around 500 GPa, where metallization is already expected according to extrapolation of optical measurements [136]. A new work claims to have found phase VI by cooling down phase V below 200-220 K [162, 163] and it could be semi-metallic. Dias and Silvera, months after announcing the discovery of a new molecular and close to a metallic phase of hydrogen up to 421 GPa [164], which could be the same semi-metallic phase VI found by Eremets *et al.* [162, 163], made a very controversial [165–168] claim of having produced metallic hydrogen at 495 GPa in a dissociated atomic state [138], as predicted by Wigner and Huntington in 1935. According to recent quantum Monte Carlo calculations, where anharmonicity was included for considering the zero-point energy [169], the $I4_1/amd$ structure is the most likely structure of this metallic atomic phase (shown in Fig. 6.1) a structure which had been predicted before [170]. Several molecular structures have been proposed for the region where phase VI is supposed to exist, with $Cmca - 4$ being a strong candidate to model it in the case it is confirmed to be metallic. In fact, very recent experiments suggested this molecular metallic phase may exist above 300 GPa [171]. However, the uncertainty of the phase diagram in this region is very large and whether metallization of hydrogen would occur due to band gap closure in a molecular phase or due to a phase transition to an atomic phase is unclear.

In this thesis we perform an exhaustive analysis of the electronic and vibrational properties of low temperature solid metallic hydrogen around its, so far, highest achieved pressure regime, which is above 400 GPa. Our goal is to provide useful information in order to diminish the uncertainty in the region of the phase diagram where metallization of hydrogen is expected to occur. With that in mind, we present first-principle calculations of the physical properties of the most probable candidate structures, as well as we try to help in structure determination with optical spectra calculations which, apart from shining some light on the latest experiment by Dias and Silvera [138], could also guide future experiments. This way, in chapter 6 we analyze the impact of anharmonicity in the stability and superconducting properties of metallic hydrogen in the 400-600 GPa pressure range, under

the hypothesis of it adopting the predicted atomic $I4_1/amd$ tetragonal structure. In chapter 7 we analyze how anharmonic effects alter the crystal structure and superconducting properties in the hypothetical scenario of metallization in the predicted $Cmca-4$ molecular structure. Finally, in chapter 8 we try to contribute on the goal of characterization of high pressure hydrogen as we analyze the optical properties of both previous candidate structures and evaluate if reflectance measurements can actually distinguish different crystalline phases.

Chapter 6

The atomic I4$_1$/amd structure

In this chapter we show the results of our *ab initio* analysis of the electronic and vibrational properties of $I4_1/amd$ hydrogen in the 400-600 GPa pressure range. While in Ref. [148] vibrational and superconducting properties of this possible first structure of atomic hydrogen phase are analyzed holding to the harmonic approach, our goal is to elucidate the impact of anharmonicity in those properties plus its consequences on lattice stability.

6.1 Computational details

We performed DFT calculations within the PBE parametrization of the GGA [45]. The electron-proton interaction was considered making use of an ultrasoft pseudopotential as implemented in QUANTUM ESPRESSO [61]. Due to the large kinetic energy of the electrons, a proper convergence of the electronic properties and phonon frequencies required a dense $80 \times 80 \times 80$ **k**-mesh and 0.05 Ry Methfessel-Paxton electronic smearing for the electronic integrations in the first Brillouin zone (BZ). An energy cutoff of 100 Ry was necessary for expanding the wave-functions in the plane-wave basis.

Phonon frequencies were calculated within DFPT as implemented in QUANTUM ESPRESSO [61] in a $6 \times 6 \times 6$ **q**-point grid in the BZ. Fourier interpolation was used to obtain the phonon spectra along high-symmetry lines. Electron-phonon matrix elements were also calculated within DFPT in a $6 \times 6 \times 6$ **q**-point grid. Converging the double Dirac delta in Eq. (4.31) required a $100 \times 100 \times 100$ denser **k**-point mesh and a 0.04 Ry Gaussian smearing. The superconducting T_c was calculated solving the isotropic Eliashberg equations [107, 108], considering that

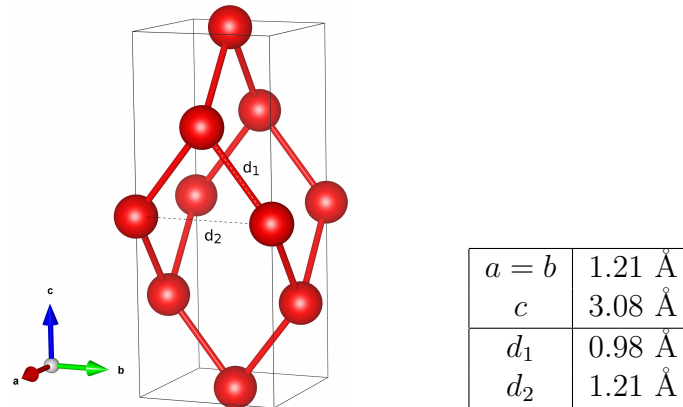| $a = b$	1.21 Å
c	3.08 Å
d_1	0.98 Å
d_2	1.21 Å

Figure 6.1: (a) Conventional unit cell of $I4_1/amd$ hydrogen. (b) $a = b$ and c lattice parameters as well as the two different interatomic distances d_1 and d_2 of $I4_1/amd$ hydrogen at 500 GPa.

for large electron-phonon coupling constants McMillan's equation underestimates T_c [172]. Besides DFPT, we have also used free-electron Lindhard response function within the Random Phase Approximation (RPA) as explained in section 3.2.1. In the latter approach the dynamical matrix is analytical at any $\mathbf{q}$ so that we have not restricted the calculations to the $6 \times 6 \times 6$ grid.

The anharmonic phonon spectra were calculated with the SSCHA [93, 94]. Forces acting on atoms were calculated in a $3 \times 3 \times 3$ supercell making use of DFT with the same parameters as the DFPT phonon calculations. This yielded phonon frequencies in a commensurate $3 \times 3 \times 3$ $\mathbf{q}$-point grid. The difference between the harmonic and anharmonic dynamical matrices was interpolated to the finer $6 \times 6 \times 6$ grid (see Appendix B). The anharmonic correction to the electron-phonon coupling and the superconducting T_c was calculated by using the SSCHA polarization vectors and phonon frequencies in Eq. (4.12), with the electron-phonon deformation potentials $\langle \phi_{n'\mathbf{k}+\mathbf{q}} | \nabla_{u_{ms}^l} H^{KS} | \phi_{n\mathbf{k}} \rangle$ calculated within DFPT.

6.2 Electronic structure

Fig. 6.2a shows the electronic band structure of $I4_1/amd$ hydrogen at 500 GPa. The bands present a huge dispersion, associated to the dominating kinetic term in the energies of the electronic states. The calculated band structure is not far from the free-electron approximation, the main difference being the band gaps opened at the border of the BZ and whenever band crossing occurs due to the
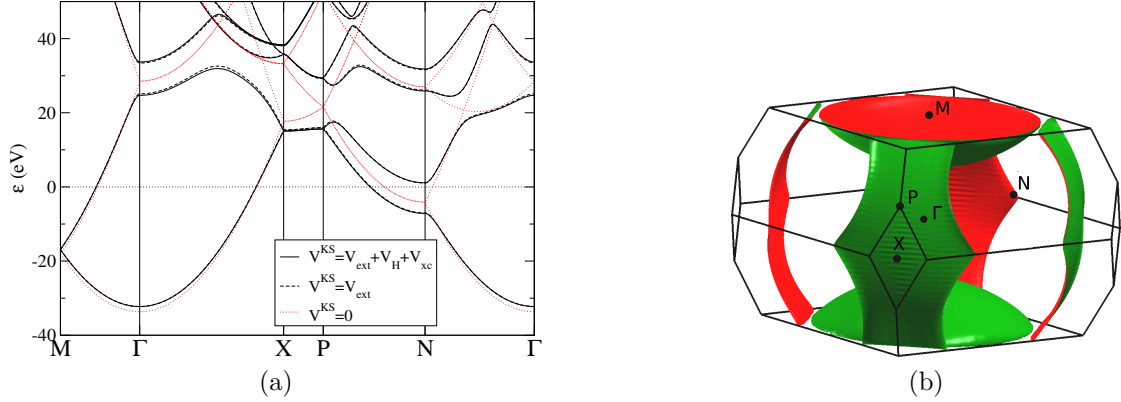
Figure 6.2: (a) Electronic band structure of $I4_1/amd$ hydrogen at 500 GPa calculated within DFT, where the self-consistent potential is $V^{KS} = V_{ext} + V_H + V_{xc}$. Bands obtained within the free-electron approach ($V^{KS} = 0$) and the independent-electron approach ($V^{KS} = V_{ext}$) are also shown. The origin of energy (black dotted line) corresponds to the Fermi level. (b) Fermi surface of $I4_1/amd$ hydrogen at 500 GPa within DFT. The BZ and its high-symmetry points are shown.

interaction of the electrons with the proton lattice. It is interesting to point out that if we consider the independent electron approximation, just keeping the V_{ext} term that gives the electron-proton interaction in the V^{KS} self-consistent potential and completely neglecting the electron-electron interactions, the resulting bands match almost perfectly with the DFT ones. Therefore, we can conclude that the main differences with the free-electron approximation are due to the large proton-electron interaction, and that the interaction between the electrons is not giving any significant contribution to the band structure. Fig. 6.2b shows the Fermi surface, which is quite spherical. However, the sphere shows some open areas around the high symmetry point N, where it touches the BZ boundary and a band gap is opened.

6.3 Harmonic phonons and lattice stability

In Fig. 6.3 we show the calculated phonon dispersion in tetragonal $I4_1/amd$ hydrogen at 500 GPa within DFPT. We also show the phonons at 400 and 600 GPa, but due to the minor qualitative changes we will focus just on the 500 GPa spectrum, as the following analysis is valid for all the pressure range. The system clearly is dynamically stable, even if there are some branches with Kohn anomalies [78], which are visible in the lowest energy transverse acoustic branch in
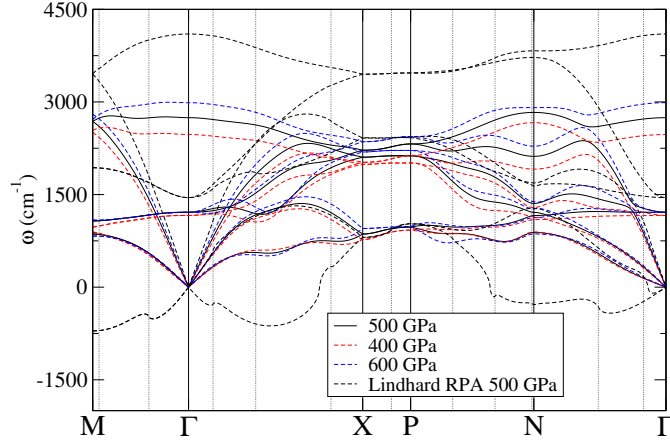
Figure 6.3: Harmonic phonon spectra of $I4_1/amd$ hydrogen calculated within DFPT at several pressures. At 500 GPa phonons calculated within the Lindhard RPA formulation are also shown. Dotted vertical black lines indicate **q**-points satisfying $|\mathbf{q} + \mathbf{G}| = 2k_f$, where Kohn anomalies are expected to appear.

form of slight oscillations. Indeed, as shown in Fig. 6.3, some **q**-points at which the anomalies appear coincide with $|\mathbf{q} + \mathbf{G}| = 2k_f$, where k_f is the Fermi wave-vector and **G** the reciprocal lattice vector that brings **q** back into the BZ.

Considering the validity of the free-electron-like approximation to describe the electronic band structure, we have calculated the phonon dispersion with the Lindhard response function at the RPA level as explained in section 3.2.1, therefore, neglecting exchange and correlation in the electronic response. In this free-electron limit we can obtain the spectra along high-symmetry lines without any Fourier interpolation (see Fig. 6.3), evidencing the presence of the Kohn anomalies at the $|\mathbf{q} + \mathbf{G}| = 2k_f$ points, and confirming that the kinks present in the DFPT result are Kohn anomalies as well.

Nevertheless, the Lindhard RPA spectrum completely differs from the DFPT calculations. The intensity of the Kohn anomalies is much stronger and the transverse acoustic modes become unstable with imaginary frequencies. While the lower strength of the Kohn anomalies in the DFPT calculations may be a consequence of Fourier interpolation, the underlying reason for the instabilities in the Lindhard approach must be physical. Even though the electronic band structure could be understood within the free-electron-like approximation, phonons seem to be far from this picture, contrary to the case of sodium [33, 77]. This fact also questions the stability of the $I4_1/amd$ tetragonal phase in the ultimate high-pressure limit where the electrons are expected to be free.
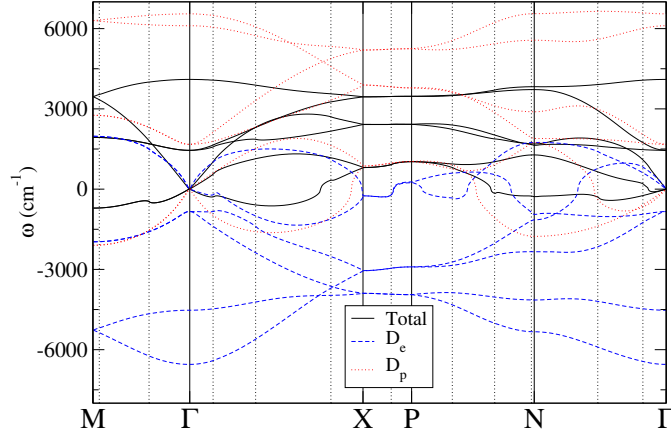
Figure 6.4: Lindhard RPA phonons of $I4_1/amd$ hydrogen at 500 GPa decomposed into the contributions coming from the D_p and D_e terms. Dotted vertical lines indicate $\mathbf{q}$-points satisfying $|\mathbf{q} + \mathbf{G}| = 2k_f$, where Kohn anomalies appear.

The origin of these instabilities can be better understood if we split the calculated dynamical matrices at a given wave-vector as $D(\mathbf{q}) = D_p(\mathbf{q}) + D_e(\mathbf{q})$. D_p represents the contribution of the proton-proton Coulomb interaction to the dynamical matrix, which can be estimated analytically with an Ewald summation. D_e contains the effect of the electronic response to the proton motion in the dynamical matrix (see Appendix A for more details). Interestingly, D_p and D_e scale differently with the average inter-electronic distance parameter r_s: D_p always scales as r_s^{-3}, while, in the Lindhard RPA, D_e scales as $r_s^{-2}(r_s + C)$, where C is always positive and of the order of unity. Therefore, in the very large pressure limit with small r_s, the D_p contribution is expected to dominate over the electronic contribution. In Fig. 6.4 we present the dispersion of the root of the eigenvalues of each contribution separately. This represents the phonon spectra that would be obtained from each contribution independently. In our case, phonons associated to D_p are already unstable and the contribution from D_e is not enough to stabilize them. This is the reason why the Lindhard RPA phonons have imaginary frequencies. As in the high-pressure limit D_p will dominate over D_e, the tetragonal $I4_1/amd$ will not become stable at very large pressure, but more symmetric and compact structures with positive eigenvalues of D_p (as fcc or bcc) will be favored.

In order to better understand the discrepancy between the *ab initio* DFPT and the Lindhard RPA spectra, we have made several calculations based on linear-response theory trying to disentangle the different contributions of the electronic response to the final phonon spectra. The main aspect we want to analyze is whether the evident failure of the Lindhard RPA model is because of the failure of the free-electron bands for estimating χ_0, or because we are neglecting exchange
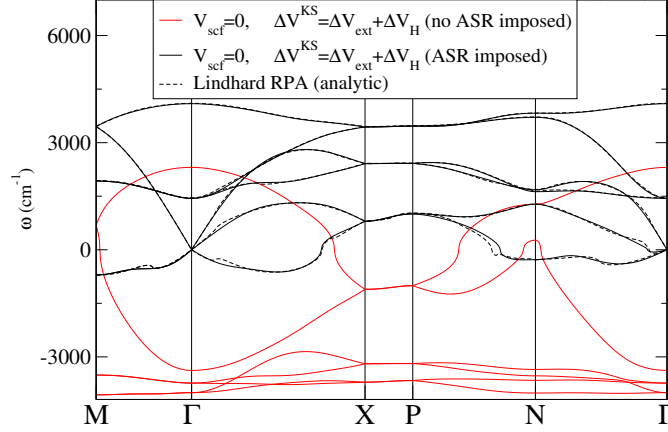
Figure 6.5: Phonon spectra of $I4_1/amd$ hydrogen at 500 GPa calculated within DFPT using $V^{KS} = 0$ and $\Delta V^{KS} = \Delta V_{ext} + \Delta V_H$ with and without imposing the ASR. The results are compared to the Lindhard RPA spectrum calculated analytically, which is an equivalent calculation.

and correlation in the Dyson equation for obtaining χ (i.e. using the RPA, f_{xc} is set to zero in the electronic screening kernel K in Eq. (3.30)). Instead of calculating χ_0 and χ explicitly using different approximations for the electronic structure and screening, which is extremely cumbersome, we use DFPT and solve the Sternheimer equation neglecting different terms in V^{KS} and ΔV^{KS}, which is equivalent to making different approaches to χ_0 and K, respectively. For instance, one recovers the Lindhard RPA by taking $V^{KS} = 0$ and taking $\Delta V^{KS} = \Delta V_{ext} + \Delta V_H$ (setting $\Delta V_{xc} = 0$).

In those cases when a different scheme is adopted for V^{KS} and ΔV^{KS} translational invariance is not satisfied anymore. We overcome this difficulty imposing the acoustic sum rule (ASR) *a posteriori* by correcting the force-constants matrix in Eq. (3.21) as

$$\phi_{0s0s}^{ll'} \longrightarrow \phi_{0s0s}^{ll'} - \sum_{ms'} \phi_{ms0s'}^{ll'}. \tag{6.1}$$

The added term corrects the second term in Eq. (3.21) dependent on the electronic density. As an example, in Fig. 6.5 we show how imposing the ASR works in the case $V^{KS} = 0$, $\Delta V^{KS} = \Delta V_{ext} + \Delta V_H$, which is equivalent to the analytic Lindhard RPA approximation. We see how after imposing the ASR the spectrum coincides with the analytic one. The small differences between the analytic spectrum and the one obtained with the DFPT procedure are because the latter is obtained from a Fourier interpolation from a $6 \times 6 \times 6$ **q**-grid, while the former one is calculated point by point.
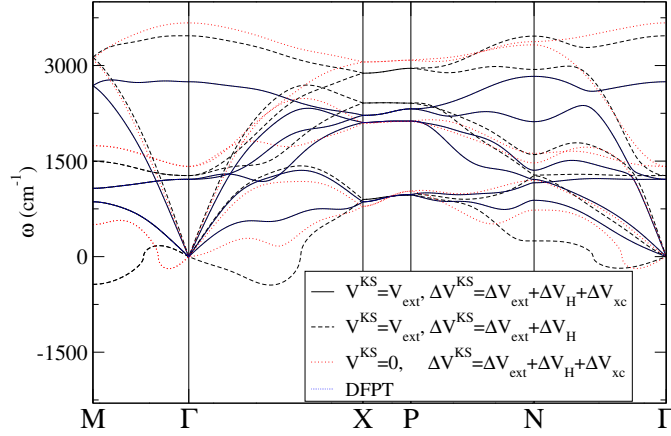
Figure 6.6: Phonon spectra of $I4_1/amd$ hydrogen at 500 GPa within different approximations for the unperturbed self-consistent potential V^{KS} and its linear perturbation ΔV^{KS}. Calculations are performed within the DFPT formalism. The ASR has been imposed *a posteriori* in every case.

In Fig. 6.6 we show four phonon spectra with different combinations of neglected terms in V^{KS} and ΔV^{KS}. First, we show the spectrum obtained by neglecting any electron-electron interaction in the unperturbed Hamiltonian ($V^{KS} = V_{ext}$), but keeping all the terms in its linear perturbation $\Delta V^{KS} = \Delta V_{ext} + \Delta V_H + \Delta V_{xc}$. We obtain exactly the same result as in the previously calculated full DFPT phonons, remarking the insignificant role of electron-electron interaction in the electronic bands and, consequently, in χ_0. Second, we show the phonons calculated neglecting electron-electron interaction in V^{KS} again, but this time neglecting the exchange and correlation term in ΔV^{KS}. This is equivalent to calculating χ_0 as in the previous case, but using the RPA for electronic screening ($f_{xc} = 0$). Finally, we show the dispersion obtained with free electrons ($V^{KS} = 0$) but using the full linear perturbation going beyond the RPA. Comparing the free-electron RPA calculation in Fig. 6.3 with the one including exchange-correlation effects for the response in Fig. 6.6, it can be confirmed that including exchange and correlation in ΔV^{KS} (and, therefore, in f_{xc}) is determinant for obtaining dynamically stable phonons. However, due to the strong electron-proton interaction, including V_{ext} in the self-consistent potential is necessary to obtain good quantitative results.

Analyzing these different calculations, we conclude that, despite the electronic kinetic energy dominates and the electron-electron interaction plays a negligible role in the band structure, going beyond the RPA including exchange-correlation effects in the calculation of the electronic response is crucial. Indeed, exchange-correlation effects in the response to the proton motion make tetragonal $I4_1/amd$ atomic hydrogen dynamically stable.
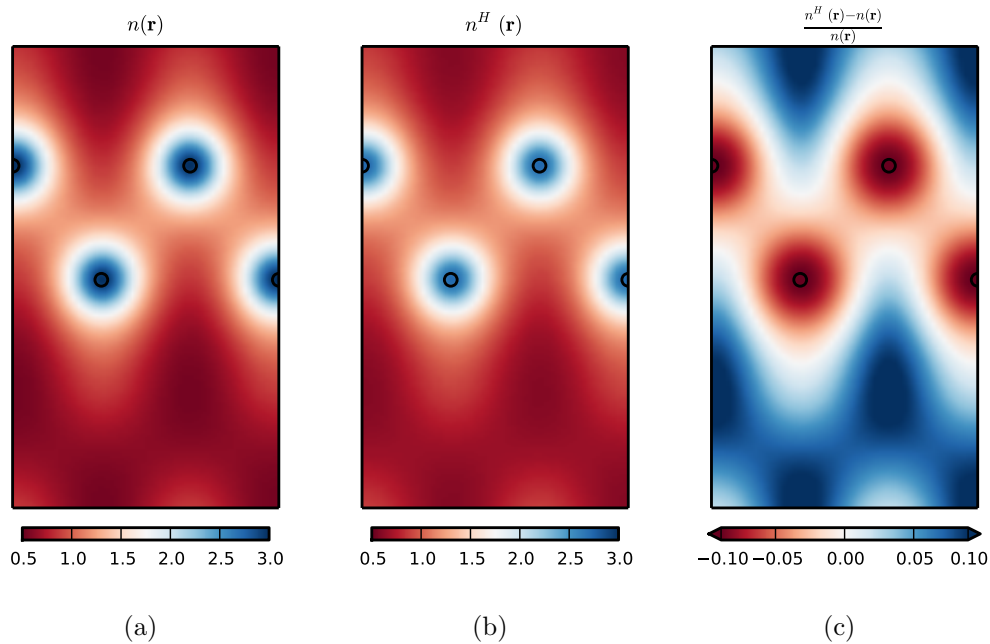
Figure 6.7:   Electronic density of $I4_1/amd$ hydrogen at 500 GPa in units of the average electron density ($0.1301\ a_0^{-3}$) for (a) $V^{KS} = V_{ext} + V_H + V_{xc}$ and (b) $V^{KS} = V_{ext} + V_H$, and (c) their difference shown in relative terms. The values are shown for the OYZ plane passing through the center of the atoms (black circles).

This calamitous failure of the RPA is related to the self-interaction error associated to the Hartree potential, which, as seen in Fig. 6.7, underestimates the high electronic density around the protons up to a 9% at 500 GPa.

We have checked that similar phonons are obtained for different approximations of the exchange-correlation potential, as seen in Fig. 6.8, where we show phonon spectra calculated using LDA, PBE and BLYP exchange-correlation functionals [45, 46, 173]. Thus, the conclusions extracted from this chapter are functional independent. This is not the case in the molecular case at lower pressures, where correlation clearly has an effect in the energies of molecular vibrons [174].

6.4   Anharmonic effects

Even if exchange-correlation effects guarantee the stability of the $I4_1/amd$ atomic structure of hydrogen, this conclusion is drawn exclusively at the harmonic level.
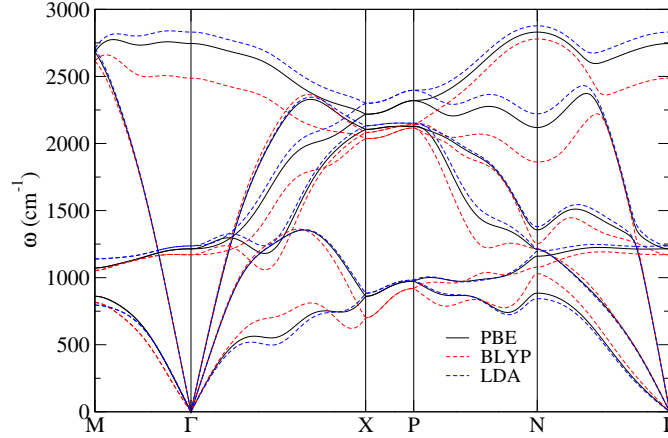
Figure 6.8: Phonon spectra of $I4_1/amd$ hydrogen at 500 GPa within different approximations for the exchange and correlation functional [45, 46, 173].

In Fig. 6.9 we compare the harmonic DFPT phonon spectra with the anharmonic spectra obtained within the SSCHA. Anharmonicity is quite strong, as phonon frequencies are affected up to a 20% in the transverse acoustic branch in the Γ-N path. Transverse acoustic branches are in general specially vulnerable as their energies are considerably lowered. Consequently, one could expect anharmonic effects to increase the zero-point displacement of the atoms, bringing atomic hydrogen closer to quantum melting. According to our calculations, however, $I4_1/amd$ hydrogen is not melted if we hold to the quantum limit of the Lindemman criterion, which states quantum melting occurs when the root mean square (RMS) displacement of atoms is around $27 - 30\%$ of the interatomic distances [175]. The RMS displacement of the atom with index s in the unit cell can be calculated with the following formula:

$$u_s^{RMS} = \sqrt{\frac{1}{N_q} \sum_{\mu\mathbf{q}} \frac{1 + 2n_B(\omega_{\mu\mathbf{q}})}{m_s \omega_{\mu\mathbf{q}}} |\boldsymbol{\varepsilon}_{s\mu\mathbf{q}}|^2}, \tag{6.2}$$

In this case, both atoms in the primitive unit cell are symmetry equivalent and, therefore, yield the same RMS displacement values. While in the harmonic approach we obtain RMS displacements of 20.3% and 16.4% at zero temperature relative to the two different interatomic distances d_1 and d_2 of the crystal, these values are only slightly raised by anharmonicity to 20.7% and 16.6%, respectively. The reason of this rather small change is a big part of the high energy modes are enhanced by anharmonicity, compensating the softening of the transverse acoustic branches.

As most of the phases have been found and characterized by Raman and infrared spectroscopy experiments, we show the impact of anharmonicity in the optical

P (GPa)	Mode	ω_h (cm^{-1})	ω_{anh} (cm^{-1})
400	E_g	1161.8	-
	B_{1g}	2472.2	-
500	E_g	1214.6	1187.9
	B_{1g}	2745.4	2769.8
600	E_g	1212.4	-
	B_{1g}	2988.4	-

Table 6.1: Raman active modes of $I4_1/amd$ hydrogen in the 400-600 GPa pressure range. Harmonic and anharmonic frequencies are represented as ω_h and ω_{anh} respectively.

modes at the Γ point in Table 6.1. The structure has two Raman active modes that are barely affected by anharmonicity. On the other hand, this structure lacks of first order IR active modes.

6.5 Electron-phonon coupling and superconductivity

In order to analyze how anharmonicity affects superconductivity, we have calculated the electron-phonon spectral function $\alpha^2 F(\omega)$ at 500 GPa both in the harmonic and anharmonic cases. $\alpha^2 F(\omega)$ shows a large peak at high energy due to the large electron-phonon linewidth of high-energy optical modes (see Fig. 6.9). The practically linear and homogeneous increase of the integrated electron-phonon coupling constant,

$$\lambda_{\text{int}}(\omega) = 2 \int_0^\omega \mathrm{d}\omega' \alpha^2 F(\omega')/\omega', \tag{6.3}$$

indicates that the contribution to the electron-phonon coupling constant is quite homogeneous over all the modes in the BZ. This analysis holds both in the harmonic and in the anharmonic case as, even though anharmonic effects have a significant impact on the phonon spectra, the electron-phonon coupling constant $\lambda = \lambda(\infty)$ is practically unaltered by anharmonicity. We obtain $\lambda = 1.68$ and $\lambda = 1.63$ in the harmonic and anharmonic cases, respectively. As λ scales with the phonon frequencies as $\propto \omega^{-2}$, the contribution of the low-energy transverse acoustic modes to the electron-phonon coupling constant is slightly enhanced due to the anharmonic suppression of their frequencies. However, this is compensated by the hardening of the high-energy optical modes.
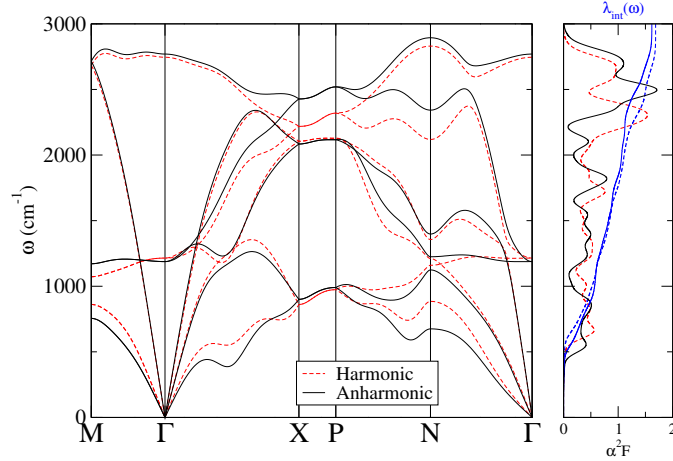
Figure 6.9: Left: harmonic and anharmonic phonon spectra of $I4_1/amd$ hydrogen at 500 GPa. Right: harmonic and anharmonic electron-phonon spectral function $\alpha^2 F(\omega)$ and frequency dependent electron-phonon coupling constant $\lambda_{\text{int}}(\omega)$.

We estimate the superconducting critical temperature by solving the isotropic Eliashberg equations in order to overcome the underestimation of T_c given by McMillan's equation in the strongly interacting limit [172]. With a Coulomb pseudopotential of $\mu^* = 0.1$ we obtain a superconducting energy gap (we take the first Matsubara frequency) of $\Delta_1 \approx 62$ meV and $\Delta_1 \approx 58$ meV in the harmonic and anharmonic cases, respectively, at 0 K (see Fig. 6.10). T_c, defined as the temperature at which the gap vanishes, is 318 K and 300 K in the harmonic and anharmonic approaches, respectively. The harmonic result is in reasonable agreement with previous results [148]. The effect of the Coulomb pseudopotential in T_c is weak, which is expected whenever λ values are considerably larger than μ^*. Therefore, anharmonicity slightly lowers the superconducting critical temperature in tetragonal $I4_1/amd$ hydrogen due to the small reduction of λ. In Fig. 6.10 we also show the first Matsubara frequencies of the energy gap at 400 GPa and 600 GPa in the harmonic approach. As wee can see, T_c is very weakly affected by pressure in the 400-600 GPa pressure range. Due to the flatness of T_c and the smooth change of the phonons with pressure (Fig. 6.3) anharmonic effects are expected to have a similar impact at 400 and 600 GPa.

Considering that in all superconducting hydrides where strong anharmonic effects in superconductivity have been reported there are strongly softened optical modes in the harmonic approximation [93, 94, 102, 157, 158], even imaginary sometimes, it seems the impact of anharmonicity on T_c is largely determined by the presence of such soft hydrogen-character optical modes. Due to the fairly uniform distribution of the electron-phonon coupling in the BZ here, there are no particular optical
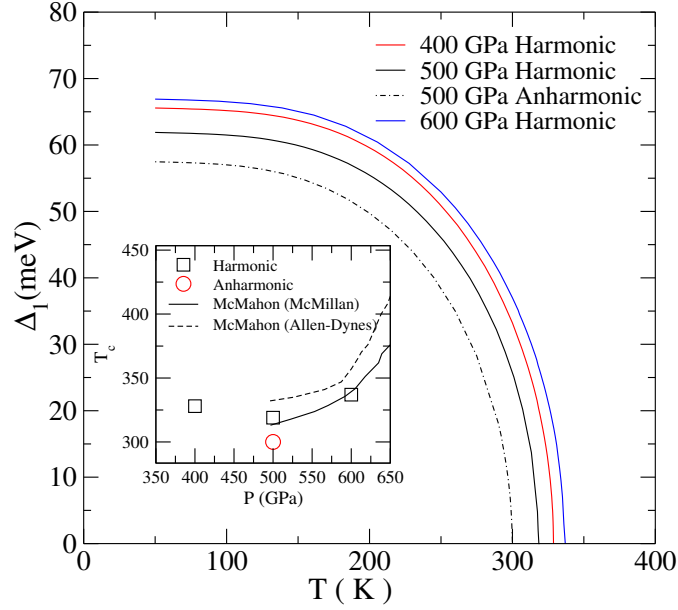
Figure 6.10: Calculated first Matsubara frequency of the superconducting energy gap of $I4_1/amd$ hydrogen at different pressures and temperatures using a Coulomb pseudopotential $\mu^* = 0.10$. Inset: T_c vs pressure in the harmonic and anharmonic cases. Solid and dashed curves correspond to the values estimated in Ref. [148], with $\mu^* = 0.089$.

modes that soften, making anharmonic effects on T_c weaker.

6.6   Conclusions

In this chapter we present an exhaustive analysis of the electronic and vibrational properties of $I4_1/amd$ hydrogen within the 400-600 GPa pressure range. Moreover, we have studied how anharmonic effects affect those mentioned properties as well as its superconductivity.

Atomic metallic hydrogen in this phase shows a nearly free-electron-like electronic band structure, where the opened band gaps can be explained even without the need of electron-electron interaction. The huge kinetic energy of the electrons due to the extremely high pressure plus their strong interaction with the bare nuclei makes the electron-electron interaction be irrelevant for the electronic structure. Nevertheless, the strong electron-proton interaction creates a big electronic localization near the atomic nuclei. Consequently, the RPA dramatically fails when

calculating the phonons of atomic hydrogen. In fact, the inclusion of exchange-correlation effects in the calculation of the electronic response to proton motion guarantees the dynamical stability of the structure.

Despite anharmonicity modifies phonon frequencies up to approximately a 20%, for instance, lowering the energies of the transverse acoustic modes and hardening high-energy optical modes, it has a minor effect on superconductivity, only suppressing T_c by a 6%. This is in stark contrast to other hydrides where anharmonicity has a huge impact on the superconducting properties [93, 94, 102, 157, 158], even inducing an inverse isotope effect in palladium hydrides [94]. This raises the interesting question whether anharmonicity impacts superconductivity in hydrides simply because hydrogen is light and vibrates far from equilibrium or for another particular reason. Our results suggest that determining whether anharmonicity has a strong impact on T_c cannot be related exclusively to the lightness of the ions present in the system, but to the presence of softened optical modes.

Chapter 7

The molecular Cmca-4 structure

While in the previous chapter we have analyzed the impact of anharmonicity on the properties of the most likely atomic candidate, we find interesting to consider its impact on the hypothetical scenario of metallization occurring in a molecular phase as well. Crystal structure predictions applying DFT within the PBE [45] generalized gradient approximation and neglecting the vibrational contribution to the free energy suggest that between 385 and 490 GPa hydrogen adopts a metallic $Cmca - 4$ orthorhombic structure with two molecules in the unit cell [160]. This molecular phase is claimed to be a high-temperature superconductor with $T_c = 242$ K at 450 GPa [147]. However, previous *ab initio* studies on this phase were performed only at the harmonic level. Anharmonicity could not only strongly affect superconductivity due to phonon frequency renormalization, but also affect the crystal structure as, unlike in the $I4_1/amd$ structure, in the $Cmca - 4$ structure atomic positions are not fully determined by symmetry. This feature has been recently shown for the record superconductor H_3S, where the quantum behavior of the proton and the consequent anharmonicity symmetrize the hydrogen bonds strongly affecting the phase diagram at the pressures where the record T_c was observed [103]. A significant structural renormalization could have implications in the electronic band-structure and in the electron-phonon coupling and, consequently, the superconducting properties.

7.1 Computational method

We performed our DFT calculations within the Perdew-Wang parametrization of the LDA [53] by making use of the QUANTUM ESPRESSO package [61]. The
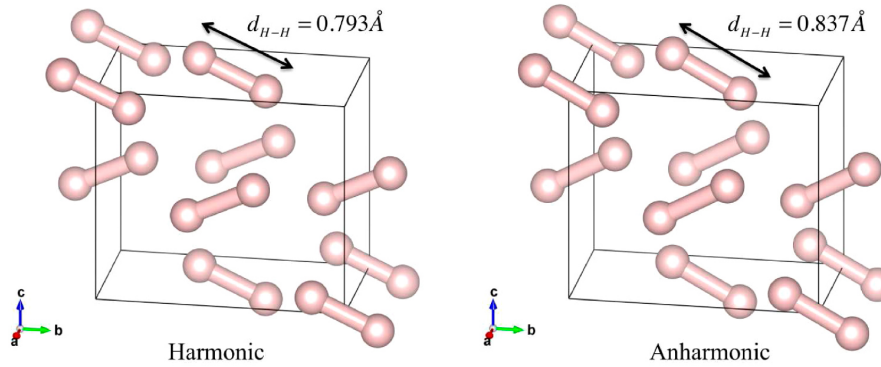
Figure 7.1: Crystal structure of $Cmca-4$ hydrogen at $414\,\mathrm{GPa}$ at the harmonic and anharmonic level in the conventional orthorhombic lattice. The hydrogen intramolecular distance $d_{\mathrm{H-H}}$ is shown for each case.

LDA is chosen to allow a direct comparison with previous calculations [147]. The electron-proton interaction was considered making use of a norm-conserving pseudopotential as implemented in Quantum ESPRESSO [61]. Convergence of the electronic properties and phonon frequencies required a $16 \times 16 \times 16$ **k**-mesh and $0.01\,\mathrm{Ry}$ Hermite-Gaussian electronic smearing for the electronic integrations in the first BZ. An energy cutoff of $65\,\mathrm{Ry}$ was necessary for expanding the wave-functions in a plane-wave basis.

Harmonic phonon frequencies were calculated within DFPT as implemented in Quantum ESPRESSO [61] in a $6 \times 6 \times 6$ **q**-point grid in the BZ. Fourier interpolation was used to obtain the phonon spectra along high-symmetry lines. Electron-phonon matrix elements were also calculated within DFPT in a $6 \times 6 \times 6$ **q**-point grid. Converging the double Dirac delta in the equation for the phonon linewidth required a $100 \times 100 \times 100$ dense **k**-point mesh. The superconducting T_c was calculated solving the isotropic Eliashberg equations (Eq. (4.57)).

Anharmonic renormalization of phonon spectra and crystal structure were calculated with the SSCHA. Forces acting on atoms were calculated in a $2 \times 2 \times 2$ supercell making use of DFT with the same parameters as the DFPT phonon calculations. This yielded phonon frequencies in a commensurate $2 \times 2 \times 2$ **q**-point grid. The difference between the harmonic and anharmonic dynamical matrices was interpolated to the finer $6 \times 6 \times 6$ grid as in the previous chapter (see Appendix B).

The anharmonic correction to the superconducting T_c was calculated combining the SSCHA dynamical matrices with the electron-phonon deformation potentials calculated within DFPT as in the previous case.

	P(GPa)	$a(a_0)$	$b(a_0)$	$c(a_0)$	$r_s(a_0)$	Wyckoff position	$d_{\mathrm{H-H}}$ (Å)
Harmonic	414	2.9345	5.1365	4.4727	1.26	(0.0000,0.3677,0.4296)	0.793
Anharmonic	414	2.9345	5.1365	4.4727	1.26	(0.0000,0.3653,0.4143)	0.837
Harmonic	450	2.8987	5.0539	4.4599	1.25	(0.0000,0.3659,0.4339)	0.782
Anharmonic	450	2.8987	5.0539	4.4599	1.25	(0.0000,0.3670,0.4085)	0.832

Table 7.1: Structural parameters of $Cmca - 4$ hydrogen at the harmonic and anharmonic level. Lattice parameters a, b, and c used in the calculations are given in units of the Bohr radius, $a0$. The coordinates of a representative of the $8f$ Wyckoff orbit in fractional coordinates of the conventional orthorhombic lattice, the Wigner–Seitz radius (r_s), and the intramolecular distance are also included.

7.2   Crystal structure

The $Cmca - 4$ structure is a base-centered orthorhombic structure with hydrogen molecules at the $z = 0$ and $z = c/2$ planes with opposite orientations as shown in Fig. 7.1, with two molecules in the primitive unit cell. Hydrogen atoms sit at the $8f$ Wyckoff positions, which have two free parameters not determined by symmetry. These two parameters determine the intramolecular H–H distance, d_{H-H} , as well as the orientation of the molecules.

In the harmonic approximation, for a given volume, the equilibrium positions are those determined by the minimum of the static BOES. If the motion of the nuclei is considered, instead, atomic positions are determined by the minimum of the free energy that includes the vibrational contribution. This is true even at zero temperature, where the vibrational free energy reduces to just the energy, due to the zero point motion of the nuclei. As we saw in section 3.4.1, if the system is an ideal harmonic solid, the static and the dynamical equilibrium positions will be exactly the same, as the centroid positions of the harmonic Gaussian density matrix coincide with the static equilibrium positions. However, this does not necessarily hold for real anharmonic solids. In the SSCHA this is calculated by minimizing the vibrational free energy with respect to the atomic coordinates. In this dynamical approach, the equilibrium positions are defined as the ones that make the quantum statistical average of the forces vanish.

Our results, summarized in Table 7.1, show that such quantum behavior significantly modifies the equilibrium Wyckoff positions in molecular $Cmca - 4$ hydrogen by increasing the intramolecular d_{H-H} distance and increasing the angle of the molecules with respect to the $z = 0$ plane. As shown in Table 7.1, the SSCHA result shows that at 414 and 450 GPa d_{H-H} is increased by a non-negligible 5.5% and 6.4%, respectively. An increase of the intramolecular H-H distance could be expected a priori if the intramolecular interaction was described by a simple

Heitler–London model [176]. It could be said that quantum behavior and anharmonicity tend to break the molecule and bring molecular hydrogen closer to an atomic crystal. This implies that it should be expected that first-principles calculations correctly incorporating the zero-point fluctuations will predict molecular dissociation of hydrogen at lower pressures than calculations at the static level.

7.3 Electronic and vibrational spectra

Figure 7.2 shows the band structure at 414 and 450 GPa calculated with the harmonic and anharmonic atomic positions. Once the molecules stretch by quantum and anharmonic effects, electron pockets are induced at the Γ and R points at these two pressures. The Fermi surface thus becomes more complex and rich at the anharmonic level with a new disk around the Γ point and a small pocket at R (see Fig. 7.3a). In Fig. 7.3b we can see how the density of states (DOS) at the Fermi level is increased by anharmonicity by approximately a factor of 1.2 at 414 GPa and 1.3 at 450 GPa. Our bands at the harmonic level at 414 GPa are in good agreement with previous calculations [147], although at 450 GPa in the results presented in [147] the Γ and R electron pockets are already occupied, while not in our case, as we predict the occupation of these states starting above 470 GPa. Considering the small energies involved, the different pressure at which the pockets appear on the Fermi surface might be attributed to the different **k**-point mesh used for the self-consistent electronic calculation, which is finer in our case [147]. Our calculations show that the pressure at which the Γ and R electron pockets appear is significantly lowered by anharmonicity. Therefore, anharmonic structural changes have a large impact on the electronic structure of $Cmca-4$ hydrogen, remarking that the zero point motion can strongly affect Fermi surface states in metals as it can modify the band gap in insulators [177–179].

With two molecules in the base-centered orthorhombic primitive unit cell, this structure presents two different vibrons, one in which the molecules in different planes vibrate in phase and a second in which they vibrate in counter phase. These two modes have a very low energy compared to those observed for molecular phases of hydrogen below 420 GPa. Peaking at the Γ point with about $2800\,\text{cm}^{-1}$, they lay far below the typical vibronic signals at energies of approximately $4000\,\text{cm}^{-1}$ [131–135, 137]. It is also remarkable the large dispersion of these vibrons over the BZ, a fingerprint of molecular vibrations being strongly coupled to the lattice. Indeed, large electron–phonon coupling is the reason for the softening of the vibrons in the $Cmca-4$ phase [147].

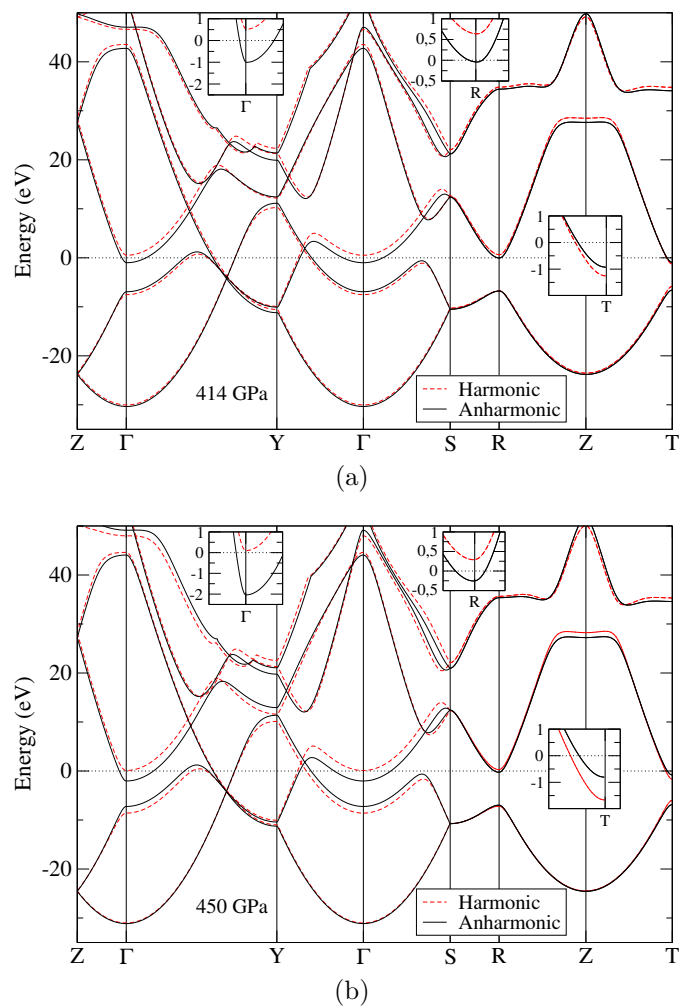The impact of anharmonicity in the phonon dispersion relation of $Cmca-4$ hy-

Figure 7.2: Band structure of $Cmca-4$ hydrogen at (a) $414\,\mathrm{GPa}$ and (b) $450\,\mathrm{GPa}$. The band structure is calculated for the crystal structure at the harmonic and anharmonic level. The Fermi energy is at $0\,\mathrm{eV}$. The insets show the band structure close to the Fermi level around the Γ, R and T points.
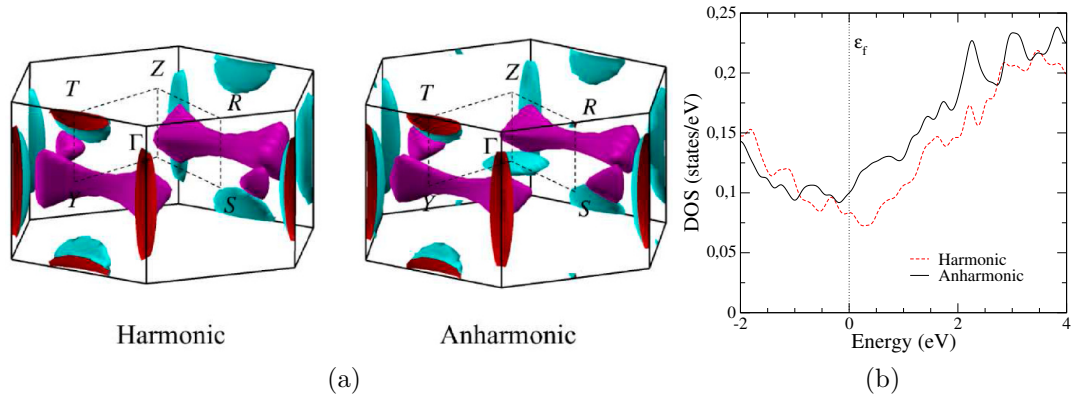
Figure 7.3: Electronic DOS of $Cmca-4$ hydrogen in the neighborhood of the Fermi level ε_f at $414\,\mathrm{GPa}$ calculated with the harmonic and anharmonic atomic positions. (b) Fermi surface at $414\,\mathrm{GPa}$ for the two different approaches.

drogen is also considerable. As shown in Fig. 7.4, the SSCHA renormalization of the phonons clearly indicates that vibronic modes are further softened by anharmonicity. The anharmonic softening of the vibrons makes these modes mix with the rest of the phonons in large areas of the BZ, even at Γ. As well as molecular stretching, the Heitler–London model [176] or enhanced Friedel oscillations induced intramolecular potential picture [78] also predict that anharmonicity tends to soften the vibrons. On the contrary, the anharmonic correction of the non-vibronic modes does not show a clear pattern as some modes are softened while others hardened. It should be noted that the small instability that appears along ZT in the anharmonic case at $450\,\mathrm{GPa}$ is an artifact of the Fourier interpolation, as no imaginary frequencies are found in the $6 \times 6 \times 6$ grid used for the interpolation.

7.4 Electron-phonon coupling and superconductivity

Considering the large electronic band-structure and phonon spectra renormalization induced by anharmonicity, a big impact on the superconducting behavior should be expected. Calculating the electron–phonon deformation potential within DFPT, we have estimated the electron–phonon coupling constant λ for $Cmca-4$ hydrogen at 414 and $450\,\mathrm{GPa}$. At the harmonic level, we obtain a value of $\lambda = 0.97$ at $414\,\mathrm{GPa}$ and a similar $\lambda = 0.89$ at $450\,\mathrm{GPa}$ (see Fig. 7.5 and Table 7.2). The
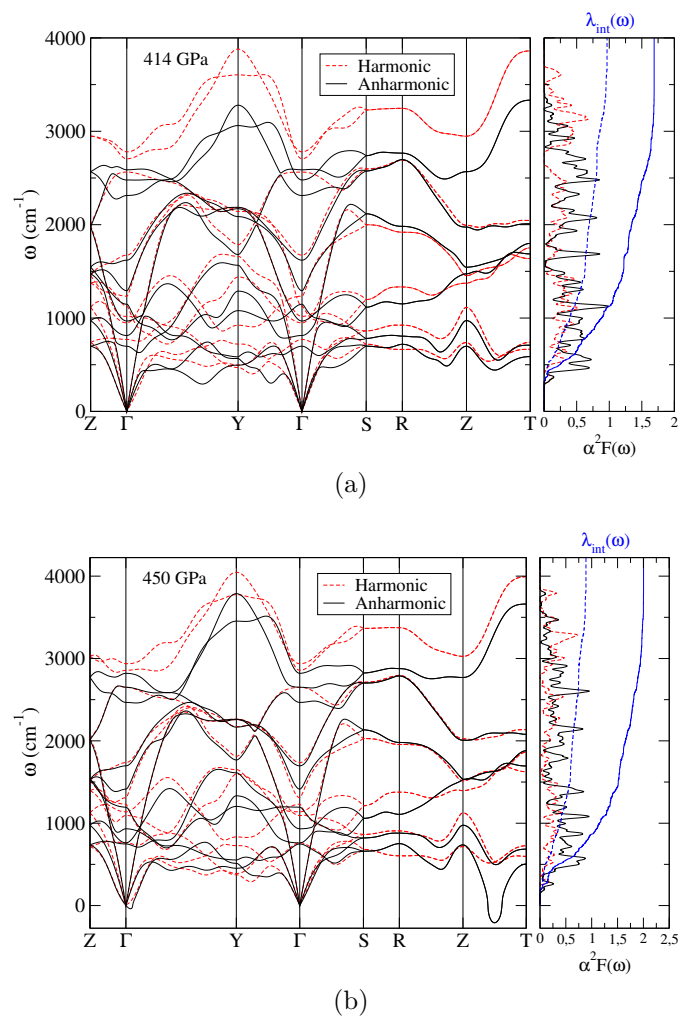
Figure 7.4: (a) Harmonic and (b) anharmonic phonon spectra of $Cmca-4$ hydrogen at $414\,\mathrm{GPa}$ and $450\,\mathrm{GPa}$. In the right panels the Eliashberg functions $\alpha^2 F(\omega)$ and the integrated electron–phonon coupling constants $\lambda_{int}(\omega)$ are shown both at the harmonic and anharmonic level.
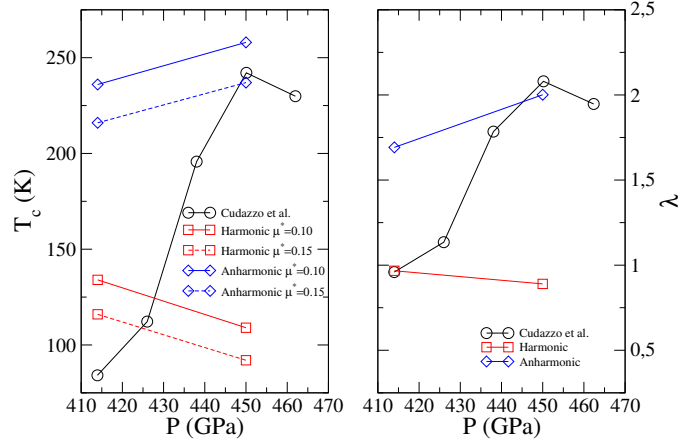
Figure 7.5: Calculated superconducting T_c, both with $\mu^* = 0.10$ and $\mu^* = 0.15$, and electron–phonon coupling constant λ for $Cmca - 4$ hydrogen both at the harmonic and anharmonic level. Results are compared with earlier calculations at the harmonic level presented in Ref. [147].

value at 414 GPa is in very good agreement with previous calculations [147], though the value at 450 GPa is much lower than the one given in [147]. The reason for the discrepancy is that there are no electron pockets at Γ and R in our case at 450 GPa, while they exist in the previous calculation. Indeed, these pockets, and specially the disk around the Γ point [147], provide new scattering channels for the electrons in the Fermi surface strongly enhancing λ. We estimate the superconducting T_cs by solving isotropic Eliashberg equations with a value of 0.10 and 0.15 for the Coulomb pseudopotential, μ^* , which covers the range estimated for it by superconducting DFT (SCDFT) calculations [155, 156]. At the harmonic level the estimated T_cs are around 100 K both at 414 and 450 GPa (see Fig. 7.5 and Table 7.2). The T_c estimated at 414 GPa is not far from the value given by SCDFT that, in contrast to the isotropic Eliashberg approach used here, considers the multi-band character of the superconductivity and includes electron-electron repulsion effects non-parametrically [147]. On the contrary, our calculation gives a much lower T_c at 450 GPa due to the lower value of λ obtained.

The superconducting behavior of $Cmca - 4$ hydrogen changes radically once the quantum and anharmonic renormalization of the Wyckoff positions and phonons is considered. As shown in Fig. 7.5 anharmonicity makes the electron–phonon coupling constant reach a value of 1.69 at 414 GPa, an increase of a factor of 1.75, and 2.00 at 450 GPa, a value 2.25 times larger than the harmonic value. This supposes a huge anharmonic enhancement of the electron–phonon coupling that brings T_c above 200 K, reaching a value of 258(237) K at 450 GPa with $\mu^* =$

	P(GPa)	$\langle\omega\rangle$ (cm^{-1})	λ	$T_c^{\mu^*=0.10}$ (K)	$T_c^{\mu^*=0.15}$ (K)
Harmonic	414	1701	0.97	134	116
Anharmonic	414	1580	1.69	236	216
Harmonic	450	1742	0.89	109	92
Anharmonic	450	1650	2.00	258	237

Table 7.2: Calculated average phonon frequency, electron–phonon coupling constant, and superconducting T_c.

0.10(0.15) .

This anharmonic enhancement of superconductivity is exactly the opposite of what has been calculated in superconducting hydrides [93, 94, 102, 103, 157, 158]. In order to unravel the possible sources of this anomaly, it is useful to write the following formula for the electron–phonon coupling constant, which can be derived from equations (4.12),(4.27) and (4.53) and reads as

$$\lambda = \frac{N(\varepsilon_F)D^2}{M\langle\omega\rangle^2},\tag{7.1}$$

where $N(\varepsilon_f)$ is the electronic DOS at the Fermi level, D^2 an effective squared deformation potential (an average of $|\langle\phi_{n'\mathbf{k+q}}|\nabla_{u_{ms}^l}H^{KS}|\phi_{n\mathbf{k}}\rangle|^2$), M the atomic mass, and $\langle\omega\rangle$ an effective phonon frequency. The reason why T_c is suppressed in hydrides is that anharmonicity tends to harden H-character optical modes and thus reduce the value of λ. Here, the situation is very different as the average phonon frequency, calculated as

$$\langle\omega\rangle = \frac{\int_0^\infty \omega g(\omega)d\omega}{\int_0^\infty g(\omega)d\omega}\tag{7.2}$$

where $g(\omega) = 1/N_q\sum_{\mu\mathbf{q}}\delta(\omega-\omega_{\mu\mathbf{q}})$ is the phonon density of states, barely changes by anharmonicity. Our results give $(\langle\omega\rangle_{\mathrm{harmonic}}/\langle\omega\rangle_{\mathrm{SSCHA}})^2 = 1.16$ at 414 GPa, while at 450 GPa the ratio is 1.12, which reflects the softening of the vibronic modes. Even if the increase of the DOS at the Fermi level of around a 20-30% and the softening of the vibrational frequencies enhances λ, according to (7.1) these are insufficient to explain the large increase of the electron–phonon coupling constant shown in Fig. 7.5. Hence, from Eq. (7.1) it can be deduced that the large increase of the electron–phonon coupling constant comes mainly from the increase of the deformation potential D. Therefore, the electron pockets created by quantum and anharmonic effects at the Γ and R points are responsible for the enhancement of λ and T_c. The occupation of these pockets specially enhances the low-energy part of the Eliashberg function $\alpha^2 F(\omega)$ as shown in Fig. 7.4 so that the integrated electron–phonon coupling constant $\lambda(\omega)$ rapidly soars at low energy.

7.5 Conclusions

In this Chapter we have studied how anharmonicity affects the structural, electronic and vibrational properties of the molecular metallic $Cmca-4$ candidate structure at 414 and 450 GPa, along with the consequent effects in its superconducting properties. We have found including anharmonic effects is of vital importance to properly account for all of the mentioned properties, showing big anharmonic renormalizations in its atomic positions, electronic band structure, phonon spectra and superconducting T_c.

Despite the fact that anharmonicity suppresses the superconducting T_c in many hydrides due to the enhancement of hydrogen character optical modes [93, 94, 102, 103, 157, 158], in the possible metallic and molecular $Cmca-4$ phase of hydrogen the situation is the contrary: anharmonicity doubles T_c bringing it from around $100\,\text{K}$ to values well above $200\,\text{K}$. The reason is that quantum and anharmonic effects strongly affect the hydrogen positions of the crystal by considerably stretching the hydrogen molecules. This has a large impact on the electronic structure by creating two extra electron pockets on the Fermi surface. The new scattering channels opened by these pockets strongly enhance the electron–phonon coupling constant and, consequently, superconductivity.

Similar molecular phases of hydrogen, which might be candidates for the first metallic phase of hydrogen, might also be strongly affected by the quantum nature of the protons and the consequent anharmonicity. The anharmonic stretching of hydrogen molecules and the consequent softening of the vibron frequencies might be a general feature among molecular phases of hydrogen. If, as it happens in $Cmca-4$ hydrogen, the structural changes open electron pockets in the Fermi surface, superconducting properties can be strongly affected in metallic molecular phases of hydrogen, in a larger degree than in the energetically most favored atomic phase in the 400–500 GPa pressure range as we analyzed in the previous chapter.

Chapter 8

Optical spectra

A huge experimental effort in the last years has characterized the phase diagram of hydrogen up to very high pressures [126, 126–137]. Even so, long after the start of this thesis, metallic hydrogen has remained elusive. There have been some works in which the first signals of metallization were present or close to appear [137, 162]. There even was a claim of having found metallic hydrogen in the form of a monoatomic liquid [126], which was put in doubt and disproved shortly after [180, 181]. However, the long standing quest might have come to an end as, early in 2017, Dias and Silvera reported the first ever laboratory-produced sample of metallic hydrogen [138].

Metallic hydrogen was claimed to have been observed as the sample became reflective above 495 GPa [138]. The claim remains controversial as doubts on the pressure calibration have been raised and semiconductors may also be reflective [165–168]. Moreover, raw reflectance data in Ref. [138] shows a sharp decrease for photon energies larger than 2 eV whose origin is not totally understood even though it was first attributed to absorption of diamond [182]. Thus, reproducibility of the experiment and exhaustive characterization of the system are necessary to confirm which would be a new milestone not only in materials science, but in physics in general.

So far, in this thesis we have calculated several properties of metallic hydrogen under the hypotheses that it adopts either an atomic or molecular structure. However, publication of Ref. [138], which claims to provide experimental data for metallic hydrogen for the first time, motivated us to contribute in the effort of characterization. As the outstanding claim in Ref. [138] relies on reflectance measurements, our initial goal was to obtain, from first-principles, the most accurate reflectance spectra of the $I4_1/amd$ atomic candidate structure as possible, covering not only

the experimental frequency range for direct comparison, but also reaching the IR and ultraviolet (UV) regimes in order to check for possible features which could help guiding future experiments. Additionally, we performed our calculations also for the $Cmca-4$ molecular phase in order to check whether optical spectra could be useful for distinguishing among crystal structures.

This way, in this chapter we present reflectance calculations of solid metallic hydrogen for the two most probable crystal structures $I4_1/amd$ and $Cmca-4$, which model solid hydrogen at around its metallization pressure in the atomic and molecular cases, respectively.

8.1   Calculation methods and procedure

The central quantity addressed in this chapter is the frequency dependent reflectivity, which for normal incident light in a medium with refractive index n can be written as

$$R(\omega) = \left| \frac{\sqrt{\epsilon(\omega)} - n}{\sqrt{\epsilon(\omega)} + n} \right|^2 , \tag{8.1}$$

where the relative dielectric function $\epsilon(\omega)$ can be expressed in terms of the optical conductivity $\sigma(\omega)$ as[1]

$$\epsilon(\omega) = 1 + i\frac{4\pi\sigma(\omega)}{\omega}. \tag{8.2}$$

The optical conductivity of a metal can be splitted into different contributions:

$$\sigma(\omega) = \sigma_{intra}(\omega) + \sigma_{inter}(\omega) + \sigma_{phonons}(\omega), \tag{8.3}$$

where σ_{intra} and σ_{inter} account, respectively, for the optical conductivity provided by electronic intraband and interband transitions, while $\sigma_{phonons}$ accounts for the direct phonon absorption contribution. As $I4_1/amd$ hydrogen, due to crystal symmetry, lacks of first order IR active vibrational modes, we set $\sigma_{phonons} = 0$. $Cmca-4$ does have some IR active modes, but we will deal with them later, in Section 8.3.

The interband and intraband contributions are computed in two stages. We first calculate the dielectric function within TDDFT as described in Chapter 5, which realistically incorporates the actual electronic structure into the dielectric function. The dielectric function is calculated by employing an interpolation scheme [183–185] of both the Kohn-Sham states and the matrix elements

---

[1]We have used atomic units, even though we show final results and graphics in different units (*e.g.* eV for energy).
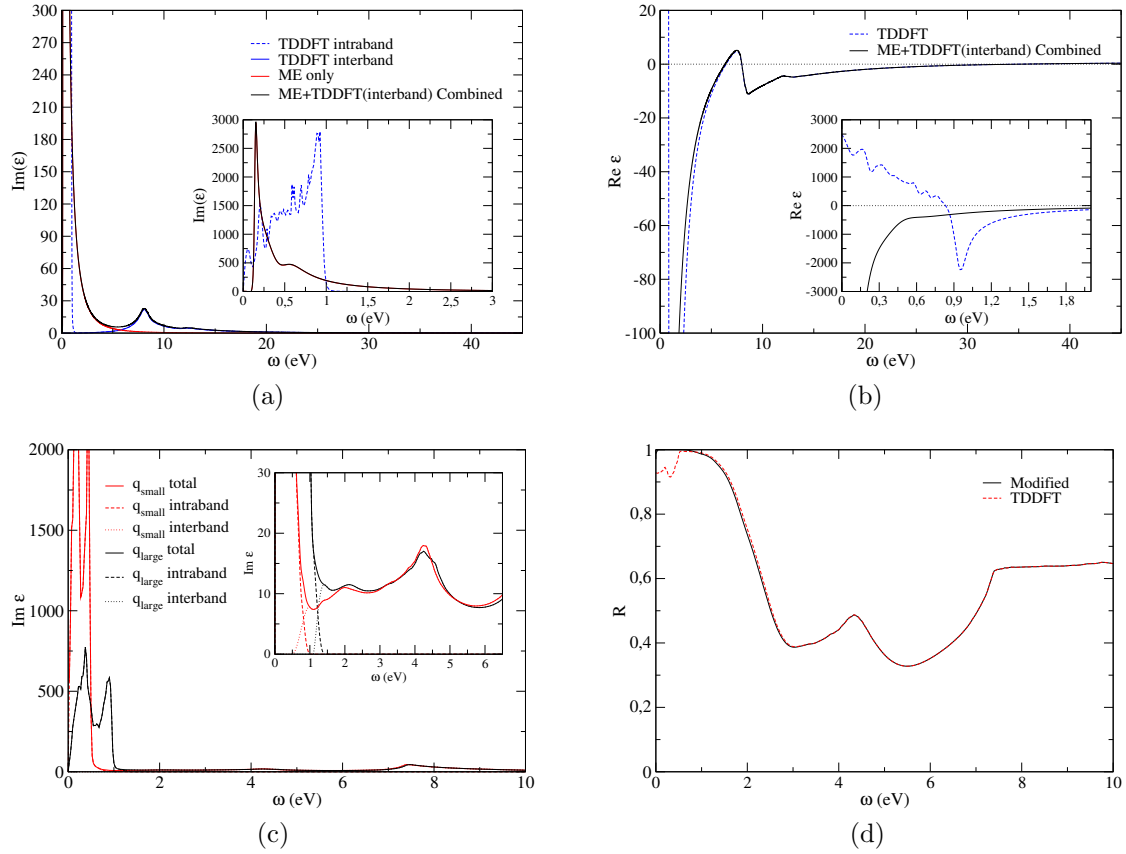
Figure 8.1: (a) Different contributions to the imaginary part of ϵ of of $I4_1/amd$ hydrogen at 500 GPa. The inset shows a zoom into lower energies. (b) Real part of ϵ calculated using the Kramers-Kronig relations. (c) Different contributions to the imaginary part of ϵ of of $Cmca - 4$ hydrogen at 414 GPa for two different momentum transfers ($\mathbf{q}_{small} = 1/160\Gamma S$ and $\mathbf{q}_{large} = 1/80\Gamma S$). The inset shows a zoom into lower energies. (d) Reflectivity of a $Cmca - 4$ hydrogen/diamond interface at 414 GPa calculated using TDDFT. The red dashed curve shows the results using the ϵ values obtained directly with TDDFT, while for the black curve the intraband contribution in $Im\ \epsilon$ has been substituted by a Delta function at $\omega = 0$ and $Re\ \epsilon$ has been obtained using the Kramers-Kronig relations afterwards. The magnitude of the Delta function is set to satisfy the f-sum rule and therefore it is related to the electronic density contributing to intraband transitions N_{intra}.

with the use of maximally localized Wannier functions [186, 187]. The method allows a very fine sampling of the reciprocal space in Eq. (5.11). In order to avoid numerical problems, a finite but small momentum is taken for the calculation of the dielectric function. The obtained optical conductivity from the TDDFT calculation thus contains both interband and intraband contributions: $\sigma^{TDDFT}(\omega) = \sigma_{intra}^{TDDFT}(\omega) + \sigma_{inter}^{TDDFT}(\omega)$. In order to incorporate the fine features of the band structure, we set $\sigma_{inter}(\omega) = \sigma_{inter}^{TDDFT}(\omega)$ in Eq. (8.3), which provides a fine description of the reflectivity at high energies.

The low-energy intraband contribution given by $\sigma_{intra}^{TDDFT}(\omega)$ is affected by the choice of a finite momentum and completely neglects how an excited electron can decay due to the electron-phonon interaction. Moreover, this regime can also be strongly affected in superconductors due to the presence of the superconducting gap [188–190]. In order to incorporate these effects into the reflectivity, the intraband contribution to the optical conductivity is calculated instead by solving the isotropic Eliashberg equations including Coulomb and impurity effects (Eq. (4.57)) and by evaluating the current-current correlation function. This function can be written in terms of the band gap and gap renormalization functions (ϕ_n and Z_n, respectively) and, if one takes the average of a spherical Fermi surface, it reads as follows [191]:

$$\Pi(i\Omega_m) = N_{free}\pi T \sum_n S_{nm}, \tag{8.4}$$

with N_{free} the free-electron density and

$$S_{nm} = \begin{cases} \frac{\phi_n^2}{R_n^3}, & (m = 0) \\ \frac{1}{R_n}, & (m = -2n - 1) \\ \frac{\tilde{\omega}_n(\tilde{\omega}_n + \tilde{\omega}_{n+m}) + \phi_n(\phi_n - \phi_{n+m})}{R_n P_{nm}} - \\ -\frac{\tilde{\omega}_{n+m}(\tilde{\omega}_{n+m} + \tilde{\omega}_n) + \phi_{n+m}(\phi_{n+m} - \phi_n)}{R_{n+m} P_{nm}}, & \text{other } m \end{cases}, \tag{8.5}$$

where $i\omega_n = i\pi T(2n - 1)$ and $i\Omega_m = i2\pi Tm$ are the fermionic and bosonic Matsubara frequencies, respectively, and

$$\begin{aligned} \tilde{\omega}_n &= Z_n \omega_n, \\ R_n &= (\tilde{\omega}_n^2 + \phi_n^2)^{1/2}, \\ P_{nm} &= \tilde{\omega}_n^2 - \tilde{\omega}_{n+m}^2 + \phi_n^2 - \phi_{n+m}^2. \end{aligned} \tag{8.6}$$

We can now write the optical conductivity in the Matsubara axis:

$$\sigma^{ME}(i\Omega_m) = i\frac{\Pi(i\Omega_m)}{i\Omega_m}. \tag{8.7}$$

The conductivity must still be analytically continued to the real axis. It is convenient to separate the imaginary-axis conductivity into the superconducting condensate contribution and additional excitations (electron-phonon coupling and impurities):

$$
\begin{aligned}
\sigma^{ME}(i\Omega_m) &= \sigma_{sc}(i\Omega_m) + \sigma_{exc}(i\Omega_m), \\
\sigma_{sc}(i\Omega_m) &= i\frac{\Pi(0)}{i\Omega_m}, \\
\sigma_{exc}(i\Omega_m) &= i\frac{\Pi(i\Omega_m) - \Pi(0)}{i\Omega_m}.
\end{aligned}
\tag{8.8}
$$

The analytic continuation of the superconducting part is just

$$
\sigma_{sc}(\omega) = \pi\Pi(0)\delta(\omega) + i\frac{\Pi(0)}{\omega},
\tag{8.9}
$$

which is exactly zero at the normal state since, as it can be seen in Eqs. (8.4) and (8.5), $\phi_n = 0 \Rightarrow \Pi(0) = 0$. We perform the continuation of $\sigma_{exc}(i\Omega_m)$ to $\sigma_{exc}(\omega)$ numerically using the Padé approximant technique of Vidberg and Serene [192]. Finally, by adding up the two contributions in the real axis we get $\sigma^{ME}(\omega) = \sigma_{sc}(\omega) + \sigma_{exc}(\omega)$.

Due to the low energy of phonons compared to interband transitions, even for hydrogen, electron-phonon coupling takes part practically at the Fermi surface. Thus, using the partial f-sum rule integral we write

$$
N_{free} = N_{intra} = \frac{2}{\pi}\int_0^\infty Re\ \sigma_{intra}^{TDDFT}(\omega)d\omega
\tag{8.10}
$$

where N_{intra} is the electronic density contributing to the intraband processes, and plug it in Eq. 8.4. Finally, we set $\sigma_{intra}(\omega) = \sigma^{ME}(\omega)$ and compute the total optical conductivity $\sigma(\omega) = \sigma^{ME}(\omega) + \sigma_{inter}^{TDDFT}(\omega)$. Since

$$
N_{inter} = \frac{2}{\pi}\int_0^\infty Re\ \sigma_{inter}^{TDDFT}(\omega)d\omega
\tag{8.11}
$$

and $N = N_{intra} + N_{inter}$, this guarantees that the total f-sum rule yields the correct total electronic density of the system.

In the $I4_1/amd$ atomic structure this procedure can be easily performed because the interband and intraband contributions in the TDDFT optical conductivities (real part) are clearly separated as it can be seen in Fig. 8.1a for Im $\epsilon(\omega) = \omega Re\ \sigma(\omega)/4\pi$. The real part of ϵ (Fig. 8.1b) is obtained afterwards using the Kramers-Kronig relations. Performing the f-sum rule integral

(Eq. (8.10)) for each contribution in the TDDFT calculation at 500 GPa we obtain $\omega_p^{intra} = \sqrt{4\pi N_{intra}} = 22.6$ eV and $\omega_p^{inter} = \sqrt{4\pi N_{intra}} = 26.3$ eV, with $\omega_p = \sqrt{4\pi N} = \sqrt{4\pi(N_{intra} + N_{inter})} = 35.0$ eV, with N_{intra} and N_{inter} being the electronic density contributing to the intraband and interband processes respectively.

In the $Cmca - 4$ molecular phase splitting the two contributions in Im ϵ is still possible, even though trickier than in the atomic case as interband and intraband transitions are closer in energy than in the atomic phase. In Fig. 8.1c we show Im ϵ calculated within TDDFT at 414 GPa for two different wavevectors in order to understand how intraband and interband contributions could be separated. We can see that the offset of intraband excitations is at a lower energy for smaller **q** as ideally, intraband and interband contributions would be completely separated for an infinitesimally small **q** where the former would just consist of a Dirac delta function at $\omega = 0$. However, numerical restrictions impose a minimum size for the wavevector. Here we use $\mathbf{q} = 1/160\Gamma S$ and in Fig. 8.1d we show how after separating both contributions and substituting the intraband contribution by a Dirac delta function at $\omega = 0$, we recover practically the same reflectivity values for energies larger than the offset of intraband transitions in the TDDFT calculation (around 1 eV). For energies smaller than the mentioned offset reflectivity is exactly one, as there are no available scattering possibilities for electrons, while in the original TDDFT calculation R takes smaller values as an artifact of the finite **q**. The f-sum rule integral for each contribution in the TDDFT calculation at 414 GPa yields $\omega_p^{intra} = \sqrt{4\pi N_{intra}} = 10.6$ eV and $\omega_p^{inter} = \sqrt{4\pi N_{intra}} = 22.6$ eV, for a total plasma frequency of 33.2 eV.

Our DFT calculations were performed by employing the QUANTUM ESPRESSO package [61]. For $I4_1/amd$ hydrogen we used a plane-wave energy cutoff of 100 Ry and a norm-conserving pseudopotential with the Perdew-Wang parametrization of the LDA [53] for the exchange and correlation potential. The wannierization process includes the 40 lowest-lying bands and was performed using the WANNIER90 package [193]. It allows us to interpolate the original $20 \times 20 \times 20$ **k**-space mesh into a fine $80 \times 80 \times 80$ mesh for the calculation of the TDDFT dielectric function. In the latter crystal local field effects were taken into account by the use of two reciprocal lattice shells [183, 185]. The Eliashberg function $\alpha^2 F(\omega)$ function needed to solve the Eliashberg equations was calculated as described in Chapter 6, but with the use of the same exchange and correlation potential as for the TDDFT calculation. $\alpha^2 F(\omega)$ was calculated at the harmonic level as we have seen in Chapter 6 anharmonicity barely affects it. Eliashberg equations were solved using a Matsubara energy cutoff of 6 times the highest phonon frequency, the same as for the Padé approximant. We solved the Eliashberg equations assuming
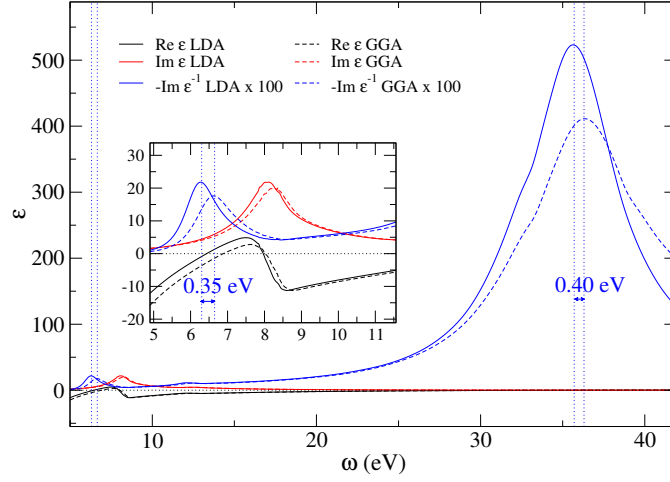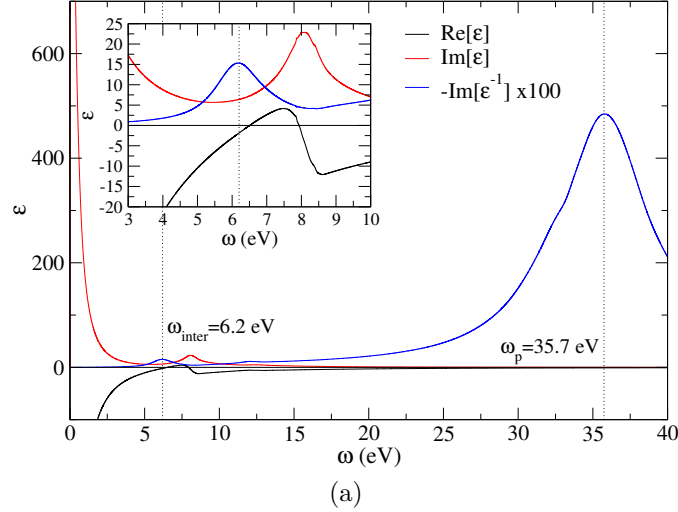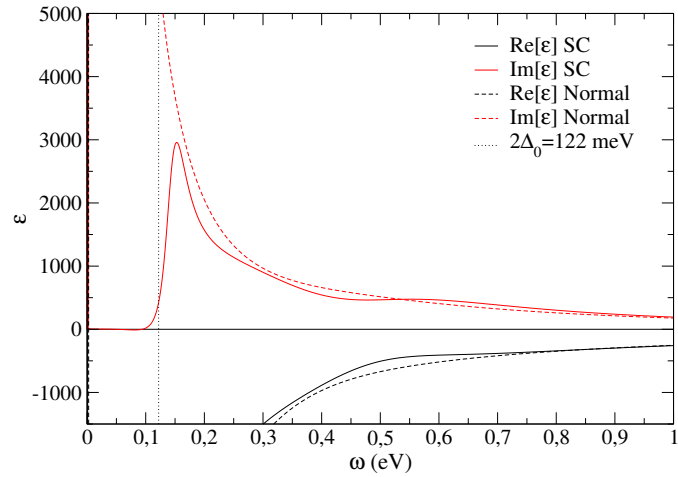
Figure 8.2: TDDFT results of the dielectric function of $I4_1/amd$ hydrogen at 500 GPa for LDA and GGA exchange and correlation functionals.

different τ_{imp}^{-1} impurity scattering rates as the latter is introduced as a parameter in the equations. We checked our results are robust with respect to the choice of exchange and correlation functional as TDDFT plasmon frequencies, which are identified as peaks in -Im ϵ^{-1} vary less than a 5% from the LDA to the generalized gradient approximation (PBE) [45] (see Fig. 8.2). Moreover, in Section 6 we saw vibrational properties (and the Eliashberg function) are not significantly affected by the choice of the exchange correlation functional nor anharmonicity. In any case, as we are dealing with a good metal where screening is good and no excitonic effects are present, we consider this combined TDDFT and Eliashberg approach as a good one for obtaining the optical properties of atomic hydrogen at high pressure. In the $Cmca - 4$ structure the calculations were performed in the same way as in the atomic phase. For the TDDFT calculations, we employed the same pseudopotential as the one used for the $I4_1/amd$ structure while the wannierization process has been checked to be converged with the use of the 30 lowest-lying bands. As in the $I4_1/amd$ case, we interpolate the original $20 \times 20 \times 20$ **k**-space mesh into a fine $80 \times 80 \times 80$ mesh for the calculation of the TDDFT dielectric function, where crystal local field effects were taken into account by the use of two reciprocal lattice shells. Even though interband and intraband transitions were closer in energy than in the atomic phase, splitting the two contributions in Im ϵ was still possible. Anharmonic effects were included because, as we saw in Chapter 7, they considerably modify the crystal structure, electronic band-structure and the electron-phonon coupling.

(a)

(b)

Figure 8.3: (a) Re ϵ, Im ϵ and -Im ϵ^{-1} for $I4_1/amd$ hydrogen at 50 K and 500 GPa for $\tau_{imp}^{-1} = 200$ meV in the normal state. The inset shows the same curves zoomed in the interband plasmon region. (b) Real and imaginary parts of the dielectric function of $I4_1/amd$ hydrogen at 50 K and 500 GPa in the IR region for $\tau_{imp}^{-1} = 200$ meV in both the normal and superconducting (SC) states.

8.2 I4$_1$/amd hydrogen

In Fig. 8.4a we show the calculated reflectivity of $I4_1/amd$ hydrogen in vacuum ($n = 1$ in eq. (8.1)) at 50 K and 500 GPa, for both the normal (which can be obtained by setting $\phi_n = 0$ in Eliashberg equations) and superconducting states. We find two different regimes for the optical spectra: the IR regime ($\omega < 1$ eV), where the effects related to scattering with phonons and impurities dominate; and the visible and UV regime ($\omega > 1$ eV) where electronic band structure effects start to play a role.

The inset in Fig. 8.4a shows the reflectivity at 50 K and 500 GPa for IR radiation. As we know from Chapter 6, T_c is above 300 K and therefore a temperature of 50 K can be considered to be in the low temperature limit, as the superconducting gap value remains constant upon reducing the temperature (see Fig. 6.10). Clean hydrogen ($\tau_{imp}^{-1} = 0$) in the normal state reflects all the incoming light until phonons start contributing substantially to $\alpha^2 F(\omega)$ above ~ 100 meV, with the large $\alpha^2 F(\omega)$ values above 250 meV inducing an even greater reduction of reflectance. When impurity scattering is taken into account reflectivity decreases from 1 right from the beginning, reaching a small plateau (~ 0.99 for $\tau_{imp}^{-1} = 200$ meV) until scattering with phonons starts to be relevant. In the superconducting state the reflectivity is equal to unity below $2\Delta_0 = 122$ meV even when impurity scattering is taken into account, as that is the amount of energy required to break a Cooper pair and make electrons contribute to the optical conductivity. This can be clearly seen in Fig. 8.3b, where Im ϵ is strictly zero below $2\Delta_0$ (except the zero frequency contribution coming from the DC conductivity of the Cooper pairs) abruptly increasing at larger energies. While for $\tau_{imp}^{-1} = 200$ meV the gap is clearly observable due to the sudden decrease of R, it is not the same for the clean case; in order to have electrons contributing to the optical conductivity one needs both to break Cooper pairs and scattering with phonons to conserve both energy and momentum. This necessity of impurities for observing the superconducting gap optically is already well-known, and becomes more evident if one plots the ratio between superconducting and normal state reflectance (R_{sc}/R_n) for different τ_{imp}^{-1} values (Fig. 8.4b). This figure clearly shows the emergence of a sharp decrease at $\omega = 2\Delta_0$ only when impurity scattering is included. The gap is observable even in the clean limit ($\tau_{imp}^{-1} = 50$ meV $< 2\Delta_0$), but the drop in R_{sc}/R_n is more notorious as one approaches the dirty limit ($\tau_{imp}^{-1} >> 2\Delta_0$).

The reflectivity above $\omega=1$ eV for normal and superconducting states is almost identical (see Fig. 8.4a). The effect of impurity scattering up to 5 eV only yields quantitative differences keeping the shape of the reflectivity curve unaltered. Moreover, temperature effects are completely negligible in this regime. Actually, for $\omega >$
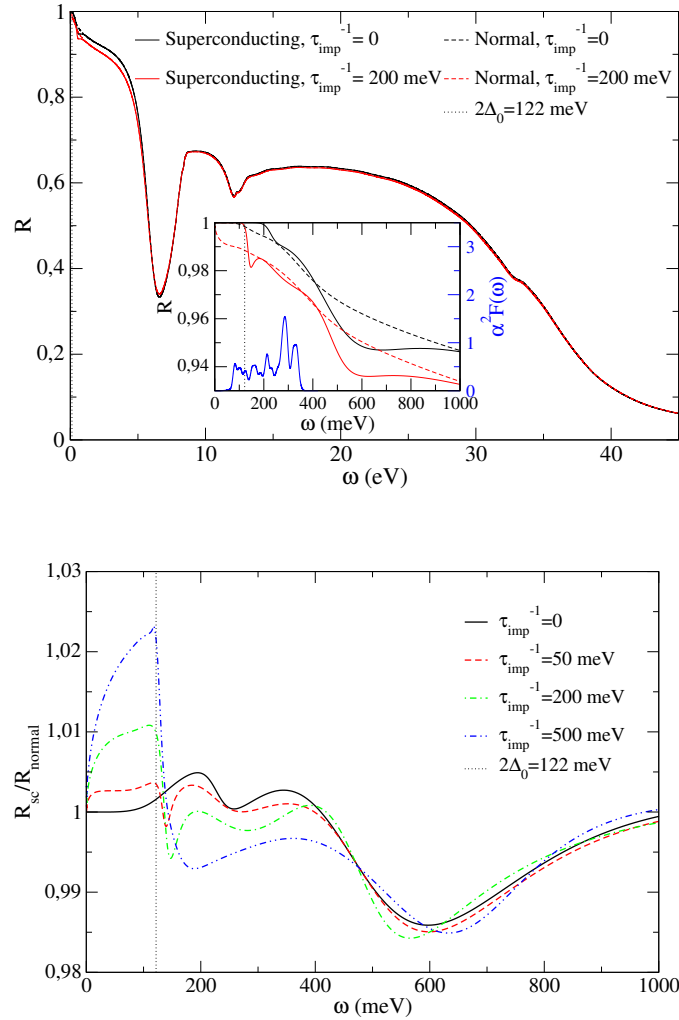
Figure 8.4: (a) Reflectivity of $I4_1/amd$ hydrogen in vacuum at 50 K and 500 GPa for different impurity scattering rates both in the normal and superconducting states. The inset shows the same curves at the low energy regime along with the electron-phonon spectral function $\alpha^2F(\omega)$. (b) Ratio between superconducting and normal state reflectance of $I4_1/amd$ hydrogen in vacuum at 50 K and 500 GPa for different impurity scattering rates.
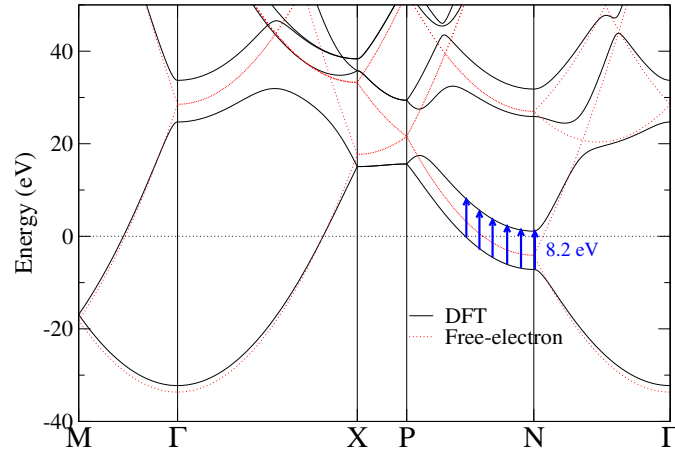
Figure 8.5: Electronic band-structure of $I4_1/amd$ hydrogen at 500 GPa. Interband transitions around the N point that yield a peak in Im ϵ are marked with blue arrows. The DFT bands are compared to the free-electron band structure. The Fermi level is at 0 eV.

5 eV all the curves converge into one, suggesting electronic scattering is dominated by electronic band structure effects rather than phonons and impurities. Remarkably, in this UV regime the reflectivity sharply decreases from a high ~ 0.95 value in the visible range ($\omega = [1.6\text{-}3.3]$ eV) to ~ 0.3 at $\omega = 6.5$ eV. This stark reduction of the reflectance is a consequence of light absorption due to the presence of an interband plasmon not expected *a priori* for a simple free-electron-like alkali metal. This is demonstrated in Fig. 8.3a, where we display the calculated dielectric function. The interband plasmon emerges around the energy where Re ϵ vanishes and Im ϵ remains low. This induces a clear peak in $-$Im ϵ^{-1} at $\omega_{inter} = 6.2$ eV as shown in Fig. 8.3a, which coincides with the drastic drop in the reflectivity. We label this plasmon as interband because it is a consequence of the interband transitions of around 8.2 eV that occur close to the N point (see band structure in Fig. 8.5). Consequently, Im ϵ shows a clear peak at 8.2 eV, which due to Kramers-Kronig relations makes the real part pass through 0 at 6.5 eV and create the interband plasmon. Even if the band structure of $I4_1/amd$ is not far from the free-electron limit as discussed in Chapter 6, the large gap opened by the electron-ion interaction at the N point suffices to induce the presence of an interband plasmon not expected for a free-electron-like metal. Thus, metallic hydrogen in the $I4_1/amd$ phase is another example in which the departure from the free-electron-like character makes interband plasmons emerge and abruptly modify the optical properties, as it occurs in other simple compounds under pressure such as Li [194–196], Ca [184], Na [185, 197], Rb, Cs [198] and AlH₃ [199]. Apart from the interband plasmon, we find that metallic hydrogen shows the expected free-electron plasmon at $\omega_p = 35.7$

Pressure (GPa)	400	500	600
Δ_0 (meV)	64.1	61.0	67.1
ω_0 (eV)	7.6	8.2	8.2
ω_{inter} (eV)	5.5	6.5	6.6
ω_p (eV)	34.2	35.7	36.8

Table 8.1: Superconducting electronic bandgap (Δ_0), interband absorption peak position (ω_0), interband plasmon peak position (ω_{inter}) and total plasma frequency (ω_p) of $I4_1/amd$ hydrogen at different pressures.

eV, which is responsible for the final decrease of the reflectivity at the extreme UV regime. This value is in good agreement with the Drude-model estimate of $\omega_p = \sqrt{4\pi N} = 35.0$ eV, where N is the total electronic density.

The sharp offset of reflectivity due to the superconducting gap lays off the IR absorption range of diamond, and should be measurable in consequence. UV absorption of diamond however would eclipse the minimum of the reflectivity predicted here at 6.5 eV due to the presence of the interband plasmon, since above the indirect electronic bandgap of 5.47 eV (at zero pressure) diamond is no longer transparent. Nevertheless, the sharp decrease associated to such plasmon starts before the absorption onset and should be observable in pure diamond. However, impurities in diamond could be responsible of light absorption at lower energies, even in the visible [182].

Finally, motivated by uncertainties in the reported pressure of the experiment [165–168] we have calculated the optical spectra for $I4_1/amd$ hydrogen at 400 and 600 GPa. As we can see in Fig. 8.7, differences are only quantitative, as the qualitative nature of the curves does not change. The energy of the interband plasmon at 400 GPa is 5.5 eV and 6.6 eV at 600 GPa, and other minor quantitative changes of the main parameters are summarized in Table 8.1.

8.3   Cmca-4 hydrogen

Figure 8.8a shows the reflectivity of this molecular phase at 414 GPa including electron-phonon and band-structure effects. Our results predict light absorption at much lower energies than in the atomic phase due to enhanced interband transitions at lower energies, which are indicated in Fig. 8.8c. Figure 8.8d shows how these transitions induce a clear peak in Im ϵ at 6.7 eV, with a shoulder at around 5 eV. This broad feature is related to available low energy interband transitions
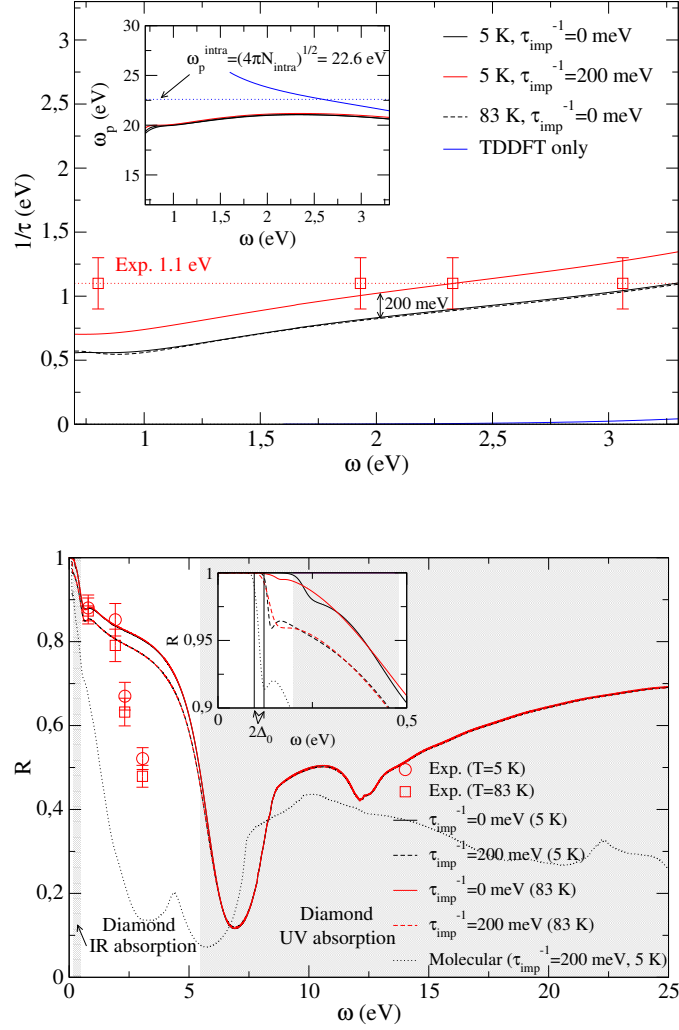
Figure 8.6: (a) Frequency-dependent electronic scattering rate of $I4_1/amd$ hydrogen at 500 GPa for different τ_{imp}^{-1} values and temperatures compared to the experimental value $\tau^{-1} = 1.1 \pm 0.2$ eV [138, 182]. The pure TDDFT calculation is also shown. The inset shows the obtained $\omega_p(\omega)$ in the same energy range, together with the ω_p^{intra} estimate. (b) Reflectivity of a $I4_1/amd$ hydrogen/diamond interface at 5 and 83 K at 500 GPa for different τ_{imp}^{-1} values. Reflectivity of the $Cmca - 4$ structure at 414 GPa is shown for comparison. Diamond IR (0.2-0.47 eV) and UV (5.47 eV electronic bandgap) absorption regions are shown in shaded gray. Experimental raw values [138] are included. The inset shows a zoom into the IR region, with the $2\Delta_0$ values of the molecular and atomic phases indicated with vertical lines at 96 and 122 meV, respectively.
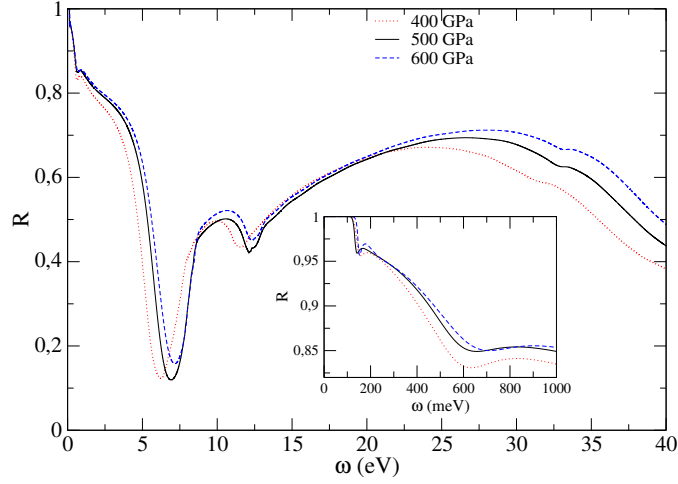
Figure 8.7: Reflectivity of a $I4_1/amd$ hydrogen/diamond interface at 400,500 and 600 GPa at 5 K and $\tau_{imp}^{-1} = 200$ meV in the superconducting state.

as shown in Fig. 8.8c. Accordingly Im ϵ^{-1} shows a broad peak centered at 2.7 eV, close to where the real part of the dielectric function crosses zero, but it decays slowly with increasing energy causing strong light absorption up to 8 eV (see Fig. 8.8a) as interband transitions are still available at those energies. At high energies, the bulk plasmon of the material appears centered at 32.0 eV, close to the free-electron value of $\sqrt{4\pi N} = 33.2$ eV, being N the average electronic density of the material.

Figure 8.8b shows the reflectivity of $Cmca - 4$ hydrogen in the infrared. As this system is also superconducting at low temperatures, it does display the abrupt decrease of reflectivity at $\omega = 2\Delta_0$. However, the bandgap in this phase is considerably smaller ($2\Delta_0 = 96$ meV). Moreover, three IR active lattice vibrations (Γ point) are expected in this structure at around 0.09, 0.14 and 0.31 eV, which would absorb light and consequently further reduce the reflectivity. Note that in the superconducting state the lowest energy IR active mode lays below the $2\Delta_0$ value, meaning it would not affect the reflectivity; it would affect the normal state reflectivity, though.

8.4   Comparison to experiments

In Fig. 8.6b we show how the raw experimental reflectivity values in Ref. [138] compare to our calculations for the $I4_1/amd$ structure at 5 and 83 K, with reflectivity calculated for a hydrogen/diamond interface by using the refractive index of
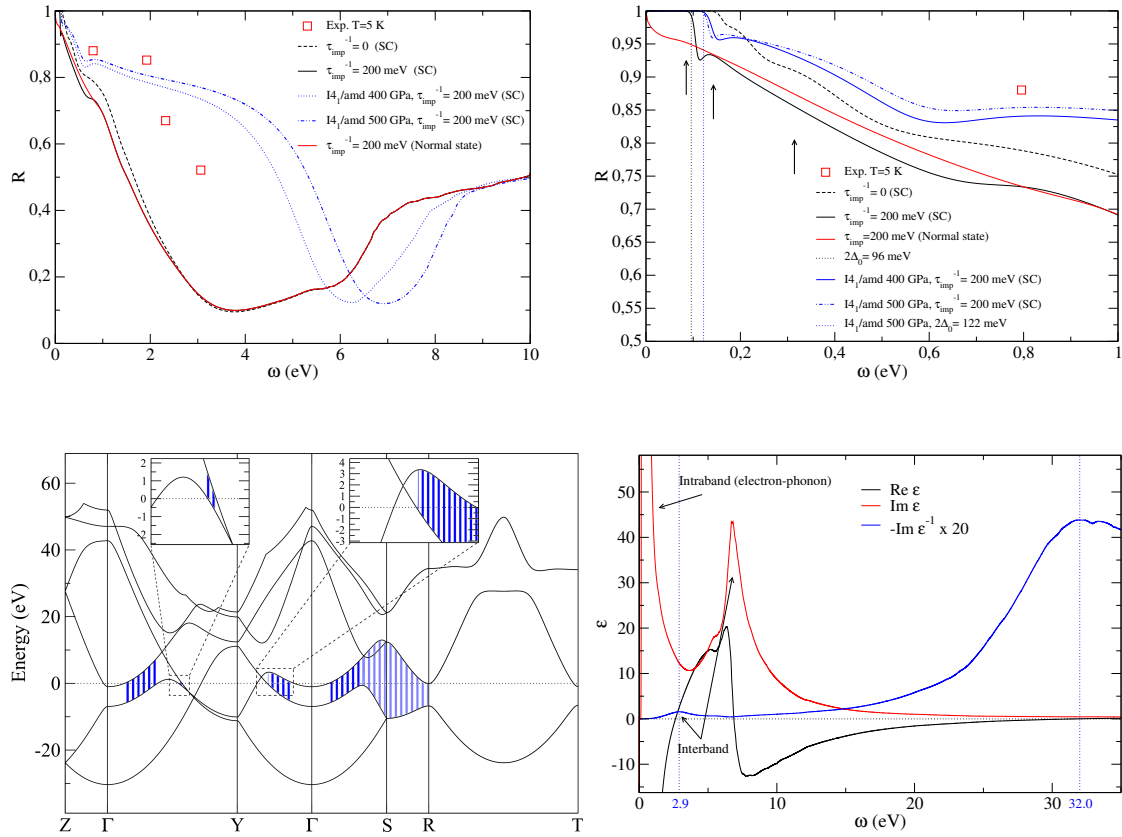
Figure 8.8: (a) Experimental data at 5 K and reflectivity of $Cmca - 4$ hydrogen at 414 GPa in the low temperature limit for different impurity scattering rates in the normal and superconducting (SC) states. Reflectivity of clean superconducting $I4_1/amd$ at 414 and 500 GPa is shown for comparison. (b) IR reflectivity of $Cmca - 4$ hydrogen at 414 GPa in the low temperature limit for different impurity scattering rates in the normal and superconducting (SC) states. Reflectivity of clean superconducting $I4_1/amd$ at 400 and 500 GPa is shown for comparison. Black arrows indicate the presence of IR active vibrational modes that could further reduce the reflectivity around the marked energies. (c) Electronic band structure of $Cmca - 4$ hydrogen at 414 GPa. Interband transitions responsible of light absorption at low energies are shown in blue. Some of the higher energy transitions are shown in pale blue. (d) Dielectric function of clean superconducting $Cmca - 4$ hydrogen at 414 GPa in the low temperature limit. Peaks in the imaginary part of ϵ and $-\epsilon^{-1}$ corresponding to intraband and interband electronic transitions are indicated with arrows.
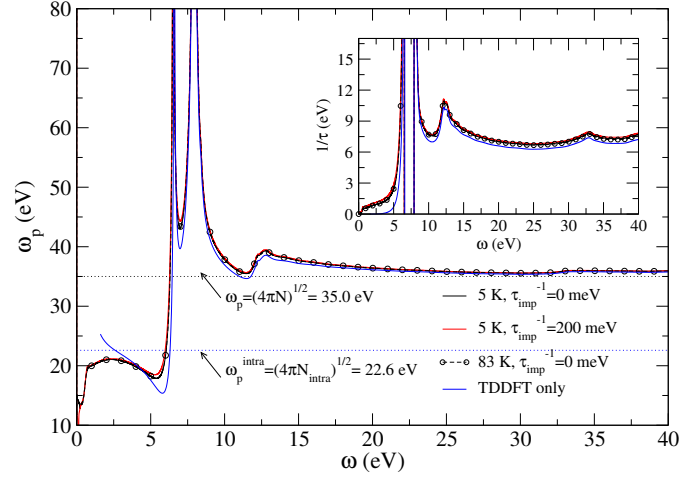
Figure 8.9: Drude model frequency-dependent plasma frequency $\omega_p(\omega)$ of $I4_1/amd$ hydrogen at 500 GPa for different impurity scattering rates and temperatures. The same curve is also obtained for the case in which the Eliashberg formalism is not considered (TDDFT only). The inset shows the frequency-dependent impurity scattering rate $\tau^{-1}(\omega)$.

$n = 2.41$ of diamond instead of $n = 1$ in eq. 8.1. Our results compare well at 5 K to the two lowest frequency experimental data points. Additionally, for comparison we also show the optical spectrum of molecular $Cmca - 4$ hydrogen (see Figs. 8.6b and 8.8a). The calculated reflectivity for $Cmca - 4$ significantly deviates from both the $I4_1/amd$ spectra and the experimental measurements due to the presence of enhanced interband electronic transitions in the molecular structure. Even though the amount of experimental data is insufficient for unequivocal determination, agreement is better with the atomic candidate. Interestingly, the calculated optical spectrum for both structures show very different features, which supports the potential validity of the reflectivity to identify the structure and encourages to extend optical measurements on a wider energy range.

In Ref. [138] the authors fitted the experimental data with the reflectivity formula following the Drude model. According to this model,

$$\epsilon(\omega) = 1 - \frac{\omega_p^2 \tau}{\omega} \frac{1}{i + \omega\tau}. \tag{8.12}$$

The plasma frequency ω_p and the mean scattering time τ are usually defined as fixed parameters, which significantly simplifies the problem yielding good results when the covered energy range is small compared to the plasma frequency of the system. When this is not the case, it can be useful to generalize this formula by making them frequency dependent. This way, for a known $\epsilon(\omega)$, one can define

$\omega_p(\omega)$ and $\tau(\omega)$ as

$$\frac{1}{\tau(\omega)} = \frac{\omega \mathrm{Im}\ \epsilon(\omega)}{1 - \mathrm{Re}\ \epsilon(\omega)} \tag{8.13}$$

and

$$\omega_p^2(\omega) = \omega \tau(\omega) \left(\omega^2 + \frac{1}{\tau(\omega)^2} \right) \mathrm{Im}\ \epsilon(\omega). \tag{8.14}$$

As the atomic candidate fits better to the experiments than the molecular one, we have calculated $\tau^{-1}(\omega)$ and $\omega_p(\omega) \equiv +\sqrt{|\omega_p^2(\omega)|}$ at 500 GPa for the $I4_1/amd$ structure using $\epsilon(\omega)$ values calculated for different impurity scattering rates and temperatures, as well as only considering TDDFT and therefore neglecting phonon and impurity scattering. In Fig. 8.9 we can see that for frequencies larger than 15 eV, all ω_p curves converge in a plateau close to the theoretical $\omega_p = \sqrt{4\pi N} = 35.0$ eV value, while τ^{-1} yields around 7 eV, regardless of whether or not including phonon and impurity scattering. This shows electronic scattering is dominated by electronic band structure effects in this high frequency regime. For frequencies lower than 5 eV but larger than 0.5 eV approximately, ω_p yields values around 21 eV, close to the $\omega_p = \sqrt{4\pi N_{intra}} = 22.6$ eV value, which is expected as the interband transitions onset at higher energies and therefore their corresponding electronic density does not contribute to ϵ. In this energy regime τ^{-1} ranges between 0.7-1.5 eV when phonon and impurity scattering is included in the calculations even if for the TDDFT only calculation yields negligible values. This shows phonon and impurities clearly govern electronic scattering for the photon energies the experiment was performed at. In the 5-15 eV interband plasmon region, ω_p and τ^{-1} take unrealistic (even negative for τ^{-1}) values. This is because the Drude formula is not adequate for modeling the optical conductivity close to interband excitations. In order to take into account the interband transitions and their contribution to ϵ, one should add a Lorentz oscillator. The same holds for the very small energy region ($\omega < 0.5$ eV), as the ω dependence of the electron-phonon and impurity scattering contribution to ϵ is more complex than the one modeled by the Drude formula.

The experimental values obtained by Dias and Silvera by fitting to a Drude model only the two lowest-energy points, which, according to the authors, are not affected by diamond absorption [182], yielded $\omega_p = 33.2 \pm 3.5$ eV and $\tau^{-1} = 1.1 \pm 0.2$ eV at 5 K [182]. In order to shed some light into these experimental values we fit our calculated dielectric function to a Drude model with frequency-dependent $\omega_p(\omega)$ and $\tau^{-1}(\omega)$, which are displayed in Fig. 8.6a. In the $\omega = [0.7 - 3]$ eV range our results yield $\omega_p \sim 21$ eV and $\tau^{-1} \sim 0.6 - 1$ eV at 5 K for a clean sample, with impurities shifting τ^{-1} upwards. Our estimated τ^{-1} in the measured frequency range is in good agreement with the experiment and clearly shows that
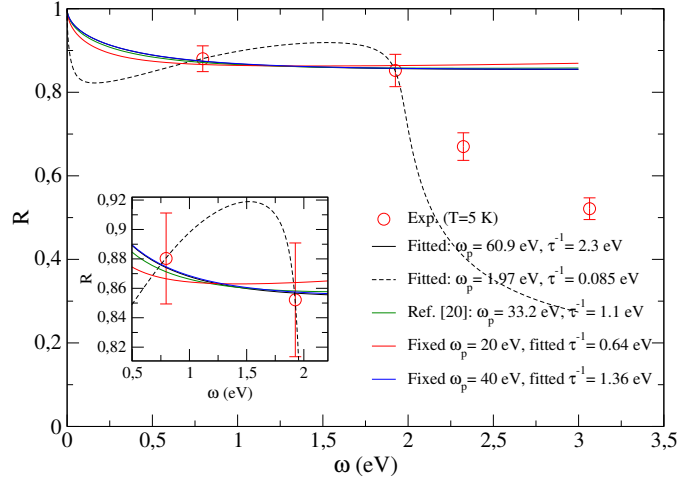
Figure 8.10:   Experimental data at 5 K [138] fitted with the Drude model (only the two lowest energy data points are fitted). Solid and dashed black curves show our two different fitting results, while the green curve shows the fitting by Dias *et al.* [182]. Red and blue curves show the curves obtained by fitting only τ^{-1} for ω_p fixed at 20 and 40 eV respectively.

its large value is mainly due to the strong electron-phonon interaction, which highlights the fact that we are dealing with a superconductor with a very large T_c. On the contrary, the value obtained for ω_p is considerably lower than the one obtained by Silvera and Dias [138, 182]. In fact, our value is consistent with the $\omega_p^{intra} = \sqrt{4\pi N_{intra}} = 22.6$ eV value, where N_{intra} is the electronic density contributing to intraband transitions. Nonetheless, in this low energy ($\omega << \omega_p$) regime very different ω_p values still provide a good fitting to the experimental data, while τ^{-1} remains almost unaltered (see Fig. 8.10). By fitting the first two experimental data points at 5 K to the reflectivity formula we have obtained at least two different results: $\omega_p = 60.91$ eV and 1.98 eV and with $\tau^{-1} = 2.21$ eV and 0.085 eV respectively (see Fig. 8.10). None of the fitted ω_p values are reasonable, either for too high or too low. It is also important to notice we do not obtain the same fitting parameters as in Ref. [182] ($\omega_p = 33.2$ eV and $\tau^{-1} = 1.1$ eV). However, if we set $\omega_p = 33.2$ eV and fit only τ^{-1} we obtain the same 1.1 eV as in Ref. [182]. We have checked that for ω_p values fixed within 20-40 eV (values close to what is expected for a nearly-free-electron-like metal at these densities) and fitted only τ^{-1} to the experimental data, the latter only oscillates within 0.64-1.36 eV yielding a good fitting to the experiments within the error bars. We thus consider the τ^{-1} value obtained experimentally [138, 182] to be more meaningful than the plasma frequency, because indeed it is this parameter what determines how much the reflectivity deviates from one for $\omega << \omega_p$.

In the experimental region our calculated reflectivity and scattering rate values are practically temperature independent (see Fig. 8.6). Our calculations predict temperature only affects the region within some meVs around the superconducting gap. This indicates the temperature dependence shown in the experiments cannot be explained with the increase of phonon occupation in the system.

8.5   Conclusions

We have made an exhaustive analysis of the optical response properties of high pressure metallic hydrogen from the infrared to the extreme ultraviolet. More precisely, we have focused on the $I4_1/amd$ and $Cmca - 4$ structures, which are candidates to model atomic and molecular metallic hydrogen close to its metallization pressure.

Our results show that in the measured energy range [138] the electronic scattering of the $I4_1/amd$ structure is dominated by the huge electron-phonon interaction of the system. Besides, our calculations reveal a sharp onset of the optical conductivity in the infrared region induced by the superconducting gap, which is remarkably large for the atomic structure. The fact that the stark offset of reflectivity produced by this gap lays below the phonon induced IR absorption of diamond makes this feature potentially accessible for optical spectra measurements.

We have also found a pronounced loss of reflectance in the ultraviolet regime due to the presence of a non-free-electron-like plasmon in $I4_1/amd$ hydrogen, similar to others predicted and found in alkalis and hydrides at high pressure [185, 194–199]. In contrast, the molecular candidate $Cmca-4$ shows a considerably different spectrum due to the presence of low energy interband absorption processes, suggesting different phases of hydrogen can potentially be distinguished from their optical spectra.

Finally, the agreement of our calculations with experiments in Ref. [138] is better for the atomic structure even if only at the two lowest energies, where the authors from Ref. [138] claim the data is not affected by diamond absorption. In fact, determining how much of the decrease in the measured reflectance comes from diamond absorption and how much from the hydrogen sample itself, potentially due to the proximity of the interband plasmon, would be very interesting. However, the disagreement on the temperature dependence of the reflectivity and the clear lack of data for a reliable fitting to the Drude formula put the results from Ref. [138] under question. Thus, our work deeply encourages further experimental research in order to not only reproduce the experiments, but also to extend opti-

cal measurements to both the UV and the IR regions. Confirming the predicted interband plasmon and measuring the superconducting gap optically would be not only of tremendous interest by itself, but also a big step towards characterizing this fascinating material.

Part III

Lithium

Lithium, the lightest metal on the periodic table at ambient conditions, is a nearly-free-electron material which adopts a compact bcc structure [200]. One could expect lithium to evolve to an even more free-electron like system with increasing pressure because the kinetic energy of electrons increases faster with pressure than the opposite sign electron-electron repulsion. However, it has been shown that pressure not only induces several structural transformations [17, 26, 201–203], but also gives rise to a plethora of fascinating physical properties [33]. For instance, lithium becomes a semiconductor near 80 GPa [23], it shows a maximum in the melting line [204] and melts below ambient temperature (190 K) at around 50 GPa [26]. It also presents one of the highest T_c for an element [7–12], reaching 20 K at 48 GPa, and it is expected to display a periodic undamped plasmon [194, 196]. Additionally, according to a recent experiment lithium shows quantum and isotope effects in its low temperature and pressure phase transformations [203].

Recently, the strongly anomalous superconducting isotope effect measured in lithium in the 15-25 GPa pressure range [9] brought this element back under the spotlight. The reported superconducting critical temperatures contrast starkly with the BCS theory, where T_c is expected to scale as $\propto 1/m^\alpha$, with m being the isotopic mass and α the isotope coefficient (0.5 within the BCS theory). Actually, for most phonon mediated superconductors, α does not deviate much from 0.5. However, the above mentioned experiment shows a highly erratic behavior of α as a function of pressure, with values ranging from 1 to 4 from 15 to 21 GPa, decreasing sharply between 21 and 25 GPa, where it even becomes negative, with values as low as -2.

Experimental evidence [17, 23, 26, 201–203] shows that in the pressure and temperature ranges where the anomalous isotope effect was measured (15-25 GPa and below 30 K) lithium presents a face centered cubic (fcc) structure. T_c rapidly soars with increasing pressure in the fcc phase, which is adopted by lithium up to 40 GPa, pressure after which it transforms to the rhombohedral $hR1$ phase. This phase is really similar to fcc as it consists of just a distortion along the c axis if one switches to a hexagonal representation. The transformation to the cubic $cI16$ phase occurs shortly after, at around 43 GPa.

Theoretical calculations within the harmonic approximation in fcc lithium show a highly softened transverse acoustic mode in the ΓK high-symmetry line [10, 27, 28, 205, 206]. Around $\mathbf{q}_{inst} = 2\pi/a(2/3, 2/3, 0)$, where a is the lattice parameter, this anomalous mode presents a huge electron-phonon coupling, becoming a key factor to explain the high T_c observed in lithium [27, 205, 206]. This softening is associated to a well defined Fermi surface nesting [10, 27, 28, 205–207] and even yields imaginary phonon frequencies at pressures where fcc is known to be stable. The instability emerges at pressures higher than 30 GPa in the local

density approximation, and at even lower pressures if one uses the generalized gradient approximation. As seen in other systems, such as simple cubic Ca [208], PdH [94], the record superconductor H_3S [103] and $NbSe_2$ [104], anharmonicity could have a significant role stabilizing this structure and, due to phonon frequency renormalization, also determining its superconducting properties.

The origin of the observed unconventional isotope effect in high pressure lithium remains unclear. In this thesis we consider the following two hypotheses to explain this behavior. (i) Phonon frequencies scale with the atomic mass differently as expected within the harmonic approximation. Therefore, while in the harmonic approach the electron phonon coupling constant λ is independent of the isotopic mass, anharmonicity could make it differ from one isotope to the other, as it happens in palladium hydrides [94]. (ii) ^6Li and ^7Li isotopes adopt different crystal structures due to the significant role of the vibrational energy in the phase diagram. Experimental evidence and previous theoretical calculations claim fcc is the most stable structure from zero pressure to 40 GPa [23, 26, 201–203]. However, it has been recently measured at lower pressures that, even if fcc is the most stable structure of lithium, other structures close in energy may be kinetically favored, which is the case of the martensitic phase [203]. Besides, this behavior has been seen to be strongly isotope dependent. Therefore, one cannot discard a similar behavior in the 15-25 GPa pressure range, specially considering the small enthalpy differences between the most competitive candidates [17, 209, 210].

Motivated by the experiment from Ref. [9], our goal is to give an explanation to the measured anomalous isotope effect in terms of phonon anharmonicity and thermodynamical stability. For that purpose we have exhaustively investigated the phonon softening of lithium in its fcc phase at 15-40 GPa, as well as its leading contribution to the electron-phonon coupling and superconductivity. Moreover, we have made precise enthalpy calculations for the competing phases in the pressure range where the experiments were performed, fully including the vibrational energy at the anharmonic level to check whether the phase transition sequence could be isotope dependent. Finally, we have calculated the superconducting T_c of the most competitive phases at several pressures to see if the values are compatible with the experimental anomaly.

In chapter 9 we analyze the phonon softening of fcc ^7Li at 26 GPa and its anharmonic renormalization. While the harmonic phonon analysis relies on DFPT, anharmonicity has been treated by solving the ionic Schrödinger equation numerically with the BOES mapped according to the polarization vector of the anomalous mode. In chapter 10 we show the results of our analysis on the possible sources of the anomalous isotope effect measured on lithium. In this case, the theoretical method of choice for including anharmonicity in the phonon spectra and enthalpy

calculations will be the SSCHA. With that goal in mind, we will extend the analysis on the fcc phase to several pressures and to both isotopes, as well as to different structures which may compete with fcc in terms of thermodynamical stability.

Chapter 9

Stability of fcc lithium at 26 GPa

The phonon softening of fcc lithium at $\mathbf{q}_{inst} = 2\pi/a(2/3, 2/3, 0)$ in the harmonic approximation is extremely important, mostly for two reasons. First, in the harmonic approach it yields imaginary phonon frequencies, which means the system should be dynamically unstable. However, it is well known fcc lithium is stable from even ambient pressure up to 40 GPa [23, 26, 201–203]. Thus, a correct treatment of the lattice dynamics in this system requires going beyond the harmonic approximation with a non-perturbative approach. Second, this anomalous mode presents a huge electron-phonon coupling and it is therefore essential for explaining the high T_c of fcc lithium under pressure.

In this chapter we analyze the anomalous vibrational mode of fcc ^{7}Li at 26 GPa in terms of *ab initio* total energy calculations. In order to deepen the understanding of the nature of this anomaly, we study the convergence of the DFPT harmonic phonon frequency of the unstable mode. We also estimate the impact of anharmonicity by solving the time independent Schrödinger equation for the potential associated to the atomic displacements along the mode of interest, which implies it does not interact with the rest of the modes in the crystal.

9.1   Computational details

Our DFT calculations were done within the Perdew-Burke-Ernzerhof (PBE) parametrization of the GGA [45]. Harmonic phonon frequencies and the electron-phonon deformation potential were calculated within density functional perturbation theory (DFPT) [81] as implemented in Quantum ESPRESSO [61]. The electron-proton interaction was considered making use of an ultrasoft pseudopo-
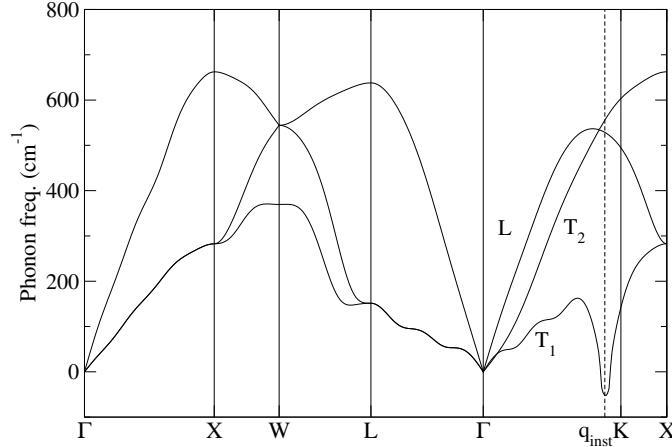
Figure 9.1: DFPT harmonic phonon spectrum of fcc Li at 26 GPa.

tential [60] in which $1s^2$ core electrons were also included. An energy cutoff of 65 Ry was necessary for expanding the wave-functions in the plane-wave basis. Converging the total electronic energy within 0.1 meV required a $30 \times 30 \times 30$ **k**-point mesh and a 0.01 Ry Methfessel-Paxton electronic smearing for electronic integrations in the first BZ.

9.2   Numerical convergence of harmonic phonons

In Fig. 9.1 we show the DFPT harmonic phonon spectrum of fcc lithium at 26 GPa. The dynamical matrices have been explicitly calculated in a $9 \times 9 \times 9$ **q**-point grid and Fourier interpolated afterwards to the chosen path in the first BZ. The transverse acoustic branch T_1 is clearly softened in the ΓK path, displaying even imaginary (shown as negative in the graph) frequencies at $\mathbf{q}_{inst} = 2\pi/a(2/3, 2/3, 0)$ ($a = 6.59\,a_0$ at 26 GPa). This point is part of the $9 \times 9 \times 9$ grid in which an explicit DFPT dynamical matrix calculation was performed, so it is not an artifact of the Fourier interpolation.

In order to better understand the nature of this anomaly, we obtained its associated energy profile by calculating the total electronic energy U for different displacements following the polarization vector of the T_1 mode at $\mathbf{q}_{inst}$. The displacements implied by this mode require a a $3 \times 3 \times 3$ supercell. In Fig. 9.2 we plot the total energy along the path described by the anomalous mode for different choices of **k**-point grids, referred to a unit cell, and smearing widths for electronic integrations. While for displacements larger than 0.05 Å the curves do not vary much among the different calculations, for small displacements the chosen convergence criteria
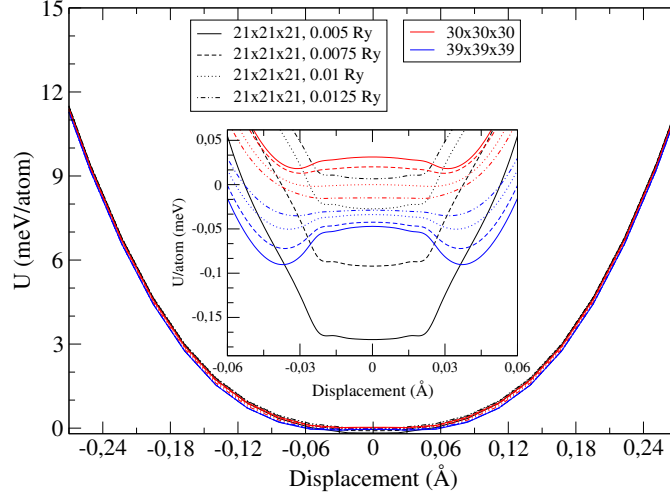
Figure 9.2: Electronic energy vs. displacement along the T_1 mode at $\mathbf{q}_{inst}$ for different choices of $\mathbf{k}$-point grids and smearing width values. In red $(30 \times 30 \times 30)$ and blue $(39 \times 39 \times 39)$ curves the same smearing width values have been chosen as in the black ones $(21 \times 21 \times 21)$. The inset shows a zoomed view of the small displacements region. The origin of energy is set at the zero displacement energy for a $30 \times 30 \times 30$ grid and 0.01 Ry smearing width. b) Convergence analysis of the DFPT harmonic frequency of the three normal modes at $\mathbf{q}_{inst}$

of 0.1 meV is clearly not enough for describing the profile properly. As one increases the BZ sampling and decreases the smearing width, the double-well shape of the energy surface sharpens. As the harmonic phonon frequency is obtained by calculating the second derivative at the equilibrium position, we expect the convergence of this value to be harsh. This is confirmed by DFPT calculations. In Fig. 9.3 we can see that, while the frequency of the L longitudinal and T_2 transverse modes converge within 1 cm^{-1}, the frequency of the T_1 transverse anomalous mode decreases monotonically as smearing values are reduced for the densest samplings of the BZ. A proper convergence would require an even denser grid and a smaller smearing width. However, such small energies and displacements are physically meaningless considering the zero point energy which, as we will see later in section 9.3, is 6.3 meV. Thus, we hold to the choice of a $30 \times 30 \times 30$ $\mathbf{k}$-point mesh and a 0.01 Ry smearing width for the rest of the calculations in this chapter and in the next one.

We estimated the harmonic frequency of the T_1 mode at $\mathbf{q}_{inst}$ by calculating the second derivative of U at the equilibrium position numerically. Performing the numerical second-order derivative using the three data-points closest to the equilibrium position (see Fig. 9.4) we have estimated a phonon frequency of -28.6
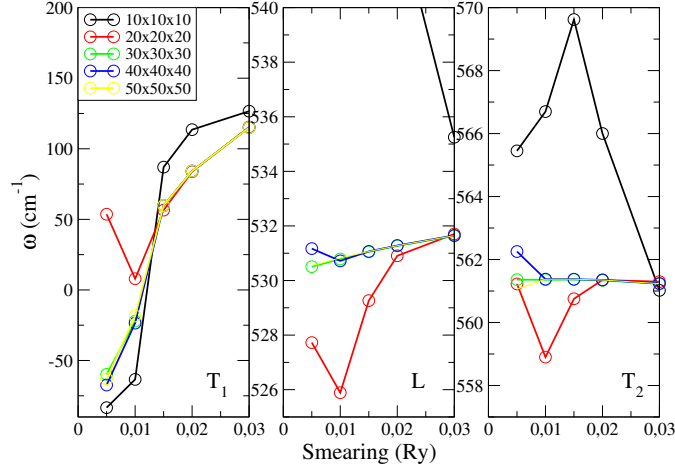
Figure 9.3: Convergence analysis of the DFPT harmonic frequency of the three modes at $\mathbf{q}_{inst}$ as a function of the smearing and $\mathbf{k}$-point mesh.

cm^{-1}. The value obtained within DFPT for the same calculation parameters is $-22.1\ cm^{-1}$, in quite good agreement with the previous finite difference result.

9.3   Solving the ionic equation

Due to the highly anharmonic shape of the energy profile of the mode under analysis, we solved the one-dimensional time-independent Schrödinger equation for the potential associated to the vibrational mode. This way, we are neglecting the interaction of the analyzed mode with the rest of the normal modes of the lattice.

We calculated the total electronic energy of the system for different atomic displacements along the anomalous vibrational mode using its polarization vector. We fitted a 10th degree polynomial to the energy vs. displacement data points and solved the eigenvalue problem using *ParametricNDSolve* in WOLFRAM MATHE-MATICA [211]. We assumed that for displacements larger than 0.7 Å the eigenfunctions vanish, discarding tunneling to adjacent positions.

In Fig. 9.4 we show the electronic energy data points, the fitted polynomial and the obtained three lowest energy eigenfunctions and eigenvalues, with values 6.3, 20.6 and 36.3 meV, respectively. The possible transitions between states yield phonon frequencies of 14.3, 15.7 and 30.0 meV (115.3, 121.8 and 241 cm^{-1}), respectively. If we compare the value of the most probable transition, 115.3 cm^{-1} ,
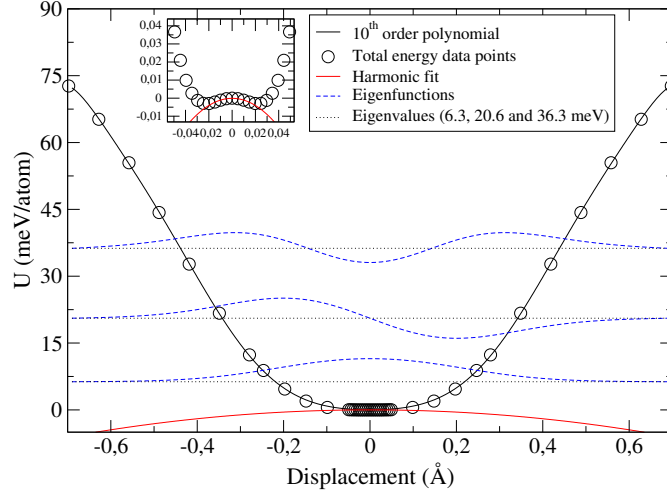
Figure 9.4: Total energy per atom (black circles), the fitted 10th order polynomial (black curve), the parabolic fit at equilibrium position (red), and the eigenfunctions (dashed blue) obtained by solving the Schrödinger equation for the polynomial potential. The amplitude of the eigenfunctions is arbitrary for better visualization, and the respective values are shifted by the corresponding eigenvalues. The inset shows the data points and the parabolic fit at the equilibrium position in the small displacements region.

which is the transition between the ground state and the first excited state, with the harmonic value of -28.6 cm^{-1}, we see a huge difference. First, the magnitude of the anharmonic correction is even larger than the harmonic value itself. Second, the shape and width of the wavefunctions and the magnitude of the eigenvalues confirm not only the lack of physical relevance of the convergence problems observed when computing the second derivative, but also the absolute failure of the harmonic approach for describing this vibrational mode. Finally, anharmonicity changes the sign of the frequency and, thus, guarantees the dynamical stability of the system at least within this frozen-phonon approach.

9.4 Conclusions

In this chapter we have analyzed the anomalous transverse phonon at $\mathbf{q}_{inst} = 2\pi/a(2/3, 2/3, 0)$ in fcc lithium. We have estimated the anharmonic correction of the unstable mode at 26 GPa for ^{7}Li using a frozen-phonon approach by solving the Schrödinger equation. While within the harmonic approach one obtains a frequency of -28.6 cm^{-1}, anharmonicity renormalizes dramatically this value up

to 115.3 cm^{-1}. Thus, it seems that anharmonicity is dynamically stabilizing this system.

This strong phonon renormalization could potentially cause the inverse isotope effect [9] by making the electron-phonon coupling constant different for the two stable lithium isotopes, as it happens in PdH, where anharmonicity explains the inverse isotope effect [94]. Anyway, our frozen-phonon calculations neglect the interaction of the analyzed vibrational mode with the rest of the modes in the crystal. Therefore, a proper quantitative analysis would require a method taking into account the phonon-phonon interaction also among different modes. The SSCHA is the proper framework to address this problem and the results of applying it to this system are shown in the next chapter.

Moreover, according to our calculations, even though it is extremely difficult to converge the harmonic frequency of the anomalous mode, converging the energy profile at relevant energy scales is considerably easier. Convergence problems only occur at very low displacements, which are unphysical, and not in the part of the potential determined by the fluctuations. Therefore, the phonon calculations including anharmonic effects within the SSCHA in the next chapter will not have these convergence issues.

Chapter 10

Superconducting isotope effect

As we mentioned in the introduction of this part, we consider the following two hypotheses to explain the anomaly: (i) λ depends on the isotopic mass due to anharmonic effects and (ii) ^{6}Li and ^{7}Li isotopes adopt different crystal structures.

In the previous chapter our results suggested fcc lithium is stabilized by anharmonic effects, since its phonon softening is hardened if one goes beyond the harmonic approach. Previous works show this soft mode contributes exceptionally to the total electron-phonon coupling constant of the system [27, 205, 206]. Since we have seen anharmonic effects modify considerably the frequency of the softening, we expect big changes in the electron-phonon coupling strength and the superconducting properties of fcc lithium once anharmonicity is considered. Here, apart from extending the analysis to different pressures, we upgrade the theoretical approach as we use the SSCHA method for including the anharmonic renormalization of lattice vibrations, as well as for calculating the electron-phonon coupling and superconducting T_c for each pressure and lithium isotope. This will allow us to check if hypothesis (i) explains the experiment from Ref. [9].

On the other hand, while according to experiments and theoretical calculations lithium adopts the fcc structure in the pressure range where the experiments were performed, the $cI16$ and $hR1$ structures are close both in pressure and enthalpy [17, 203, 209, 210]. In order to account for hypothesis (ii), we have made precise enthalpy calculations for the three competing phases at different pressures and calculated the T_cs for the $cI16$ phase as well. As we will see in section 10.3, we will discard $hR1$ as a competing phase and we will not evaluate its T_c.
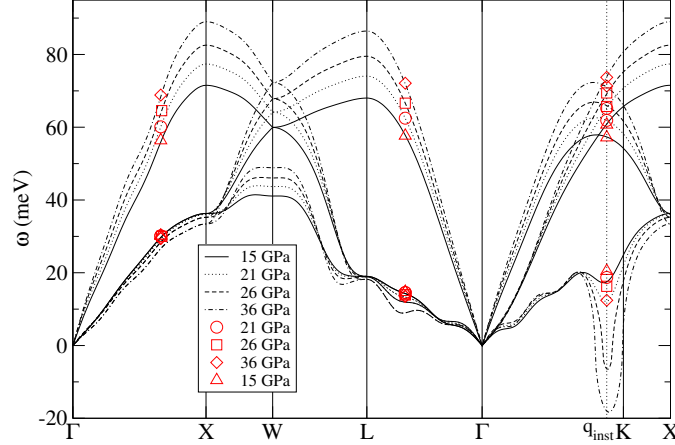
Figure 10.1: Harmonic (black curves) and anharmonic (red symbols) phonon spectra of fcc ^{7}Li at different pressures. Harmonic spectra are obtained by Fourier interpolating the $9 \times 9 \times 9$ **q**-grid data to the desired path. Anharmonic data corresponds to SSCHA calculations in a $3 \times 3 \times 3$ **q**-point grid.

10.1 Anharmonic phonon spectra and electron-phonon coupling

In this chapter we will use the same exchange-correlation functional, pseudopotential and calculation parameters as in chapter 9.

10.1.1 Fcc structure

Harmonic dynamical matrices of fcc Li have been obtained in a $9 \times 9 \times 9$ **q**-grid within DFPT for every analyzed pressure and isotope. In Fig. 10.1 we show the harmonic phonon spectra obtained at 15, 21, 26 and 36 GPa for ^{7}Li after Fourier interpolating the dynamical matrices from the $9 \times 9 \times 9$ grid to the desired path. We do not show the spectra for ^{6}Li since they are essentially the same, except for the larger frequencies due to the lower mass. We can see increasing pressure makes most of the modes increase their frequency, except the low frequency transverse branch, which is softened. This decrease is specially large at $\mathbf{q}_{inst}$, where as shown in Fig. 10.2, it yields negative (imaginary) values above 25 GPa in the harmonic case, a considerably lower pressure than the 30 GPa obtained with the LDA in previous calculations [10, 27, 28, 205–207].

We calculated the anharmonic dynamical matrices in a $3 \times 3 \times 3$ **q**-grid commen-

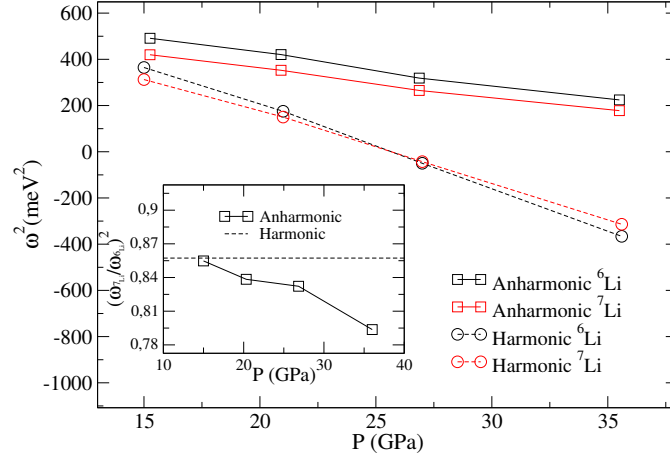Figure 10.2: Squared phonon frequencies of the anomalous transverse acoustic mode at $\mathbf{q}_{inst}$ for ^{6}Li and ^{7}Li isotopes as a function of pressure. The inset shows the ratio of the frequencies for both isotopes at the anharmonic level and the harmonic value obtained from the ratio of the isotopic masses.

surate to the supercell used for our SSCHA calculations, in which we calculate forces acting on atoms. According to our calculations, the anomalous mode gets a strong renormalization due to anharmonic effects. Fig. 10.2 shows the anharmonic frequency of the anomalous mode for different pressures, confirming fcc lithium is dynamically stabilized by anharmonicity above 25 GPa as the frequency takes positive values.

From Fig. 10.1 one can deduce that anharmonicity is primarily localized at the softened mode. In order to analyze this in detail and see how anharmonicity is distributed over the first BZ, we show in Fig. 10.3 the DFPT point-by-point (without Fourier interpolation) harmonic phonon dispersion of fcc ^{7}Li at 26 GPa and the anharmonic corrections calculated within the SSCHA. We performed the SSCHA calculations in $3 \times 3 \times 3$ and $4 \times 4 \times 4$ supercells to obtain anharmonic dynamical matrices in the respective commensurate $\mathbf{q}$-point grids. We can confirm that anharmonicity is localized around the phonon softening at the transverse acoustic T_1 branch at $\mathbf{q}_{inst}$ where, as we saw in the previous chapter, the frequency is strongly shifted up by anharmonic effects. In fact, the SSCHA value of 16.2 meV at 26 GPa is in quite good agreement with the 14.3 meV frozen phonon value from the previous chapter.

Electron-phonon matrix elements were calculated within DFPT in a $9 \times 9 \times 9$ $\mathbf{q}$-grid, where converging the double Dirac delta in the equation for the phonon linewidth required a denser $80 \times 80 \times 80$ $\mathbf{k}$-point mesh. Anharmonic effects were included using
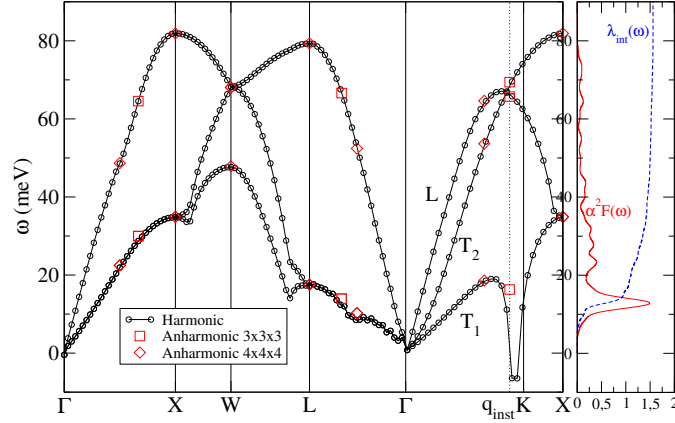
Figure 10.3: Fcc ^{7}Li phonon dispersion at 26 GPa. Anharmonic phonons within the SSCHA are calculated both for a $3 \times 3 \times 3$ and a $4 \times 4 \times 4$ grid of points. The Eliashberg function $\alpha^2 F(\omega)$ and the integrated electron-phonon coupling $\lambda_{int}(\omega)$ is also shown for the anharmonic case.

the same method as in hydrogen, with anharmonic dynamical matrices interpolated to the $9 \times 9 \times 9$ grid with the method explained in Appendix B.

The superconducting T_c was calculated solving the isotropic Eliashberg equations (eq. (4.57)) considering that for large electron-phonon coupling constants McMillan's equation underestimates T_c [172]. We estimate a μ^* value of 0.17 using the Morel-Anderson formula [212]:

$$\mu^* = \frac{\mu}{1 + \ln\left(\frac{\varepsilon_f}{\omega_D}\right)}. \tag{10.1}$$

The average electron-electron Coulomb repulsion term μ was obtained from Thomas-Fermi screening theory, a free-electron Fermi energy ε_f was chosen, and the Debye cutoff phonon frequency ω_D was taken as the highest frequency of the longitudinal acoustic modes [213]. We have also used the McMillan equation (eq. (4.58)) and different μ^* values for testing the convergence of T_c with the **q**-point grid and for comparing our results with other works.

In Fig. 10.4a we can see how converging T_c and λ with the **q**-point grid becomes tedious due to the large contribution of $\mathbf{q}_{inst}$ to the total electron-phonon coupling. Our chosen $9\times9\times9$ grid overestimates T_c by 2.5 K comparing to the $12\times12\times12$ case while λ is 0.2 larger. However, increasing the grid size would make the calculation really demanding. Moreover, as our goal is to check whether anharmonicity can explain the anomalous isotope effect, this overestimation only makes anharmonic effects more visible as it gives more weight to $\mathbf{q}_{inst}$ in our estimations. Moreover, we clearly see grids not containing $\mathbf{q}_{inst}$ (dimensions not multiple of 3) yield smaller
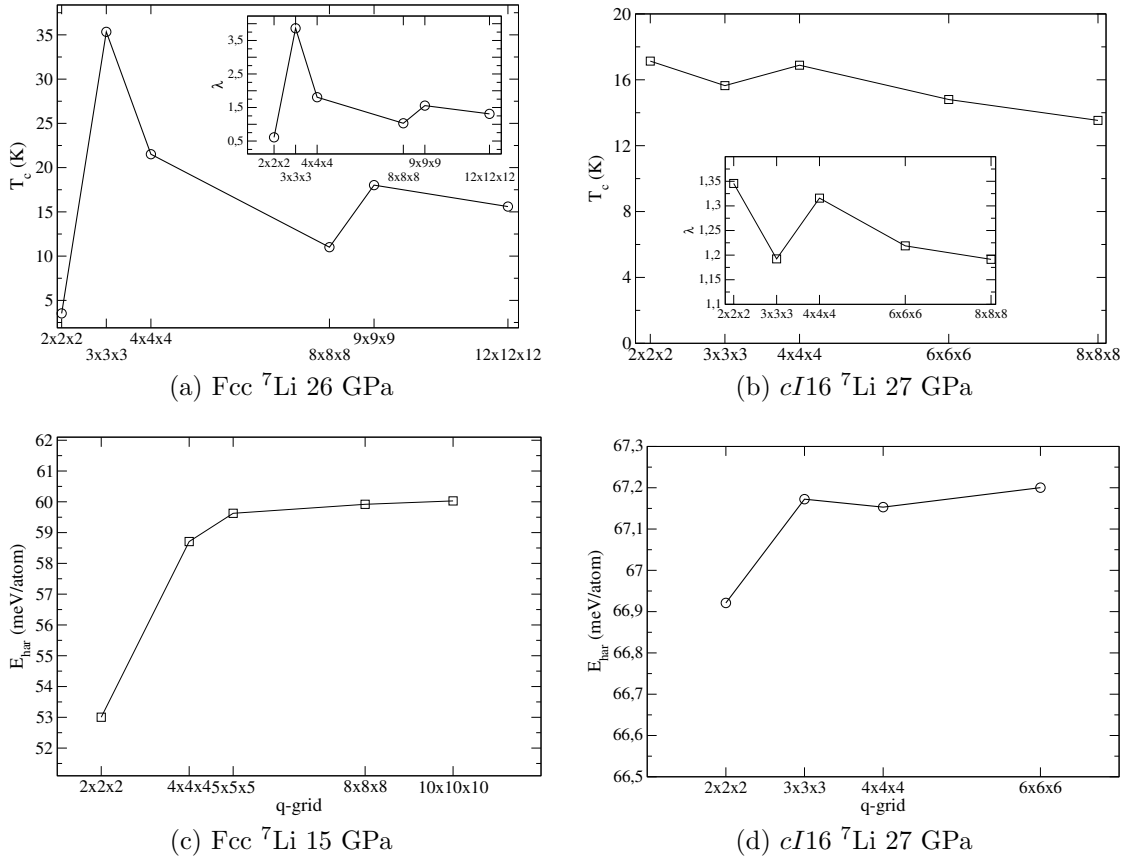
Figure 10.4: Convergence of T_c and λ with the $\mathbf{q}$-grid for (a) fcc and (b) $cI16$ ^{7}Li, using McMillan equation and $\mu^* = 0.17$ and convergence of E_{har} with the $\mathbf{q}$-grid for (c) fcc and and (d) $cI16$ ^{7}Li.
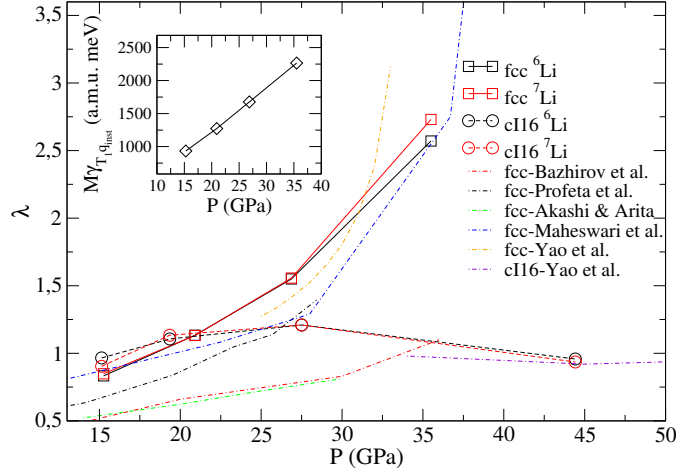
Figure 10.5: Total electron-phonon coupling constant λ of fcc and $cI16$ lithium calculated for its two isotopes at different pressures. The inset shows the phonon linewidth of the T_1 mode of fcc Li at $\mathbf{q}_{inst}$ multiplied by the atomic mass, the product being independent of the phonon frequency and the isotopic mass. The calculated λ is compared to previous calculations [10, 27, 205, 206, 210].

T_c and λ values that the ones they do, and using such grids would obviously neglect how anharmonicity affects the electron-phonon coupling and superconductivity.

Our combined SSCHA and DFPT electron-phonon coupling calculations displayed in Fig. 10.5 show the total coupling constant λ rises abruptly with increasing pressure in the fcc phase. Starting from an already high value of 0.85 at 15 GPa it reaches a value as high as 2.6 at 36 GPa. This dramatic growth is directly related to the rapid increase of the electron-phonon linewidth γ of the T_1 mode at $\mathbf{q}_{inst}$, which doubles its value in the mentioned pressure range (see inset of Fig. 10.5). The remarkable peak in the Eliashberg function $\alpha^2 F(\omega)$ and the associated abrupt growth of the integrated electron-phonon coupling constant $\lambda_{int}(\omega)$ around the frequency of the anomaly (see Fig. 10.3) is another fingerprint of how relevant this softening is in the superconducting properties of fcc lithium.

Our λ values, which do not almost differ from one isotope to the other, are slightly larger than the ones by Maheswari *et al.* [206] and Profeta *et al.* [27] and quite larger than the ones by Akashi *et al.* [205] and Bazhirov *et al.* [10]. We attribute these disagreements to the large dependence of λ with the $\mathbf{q}$-point grid. While we use a $9 \times 9 \times 9$ sampling of the BZ for the electron-phonon and lattice dynamics calculations, where $\mathbf{q}_{inst}$ is explicitly taken into account, the mentioned works use $8 \times 8 \times 8$ grids ($7 \times 7 \times 7$ in the case of Maheswari *et al.*), where it is not. According to our convergence tests described previously (see Fig. 10.4a), those grids clearly
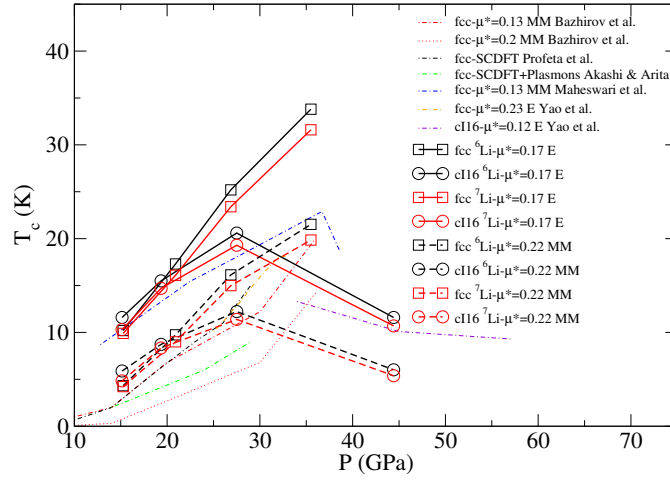
(a) Estimated T_c of fcc and $cI16$ lithium for its two stable isotopes at different pressures (lines with symbols) calculated solving Eliashberg equations (E) or using the McMillan equation (MM). The results are compared to other theoretical estimations (dashed and dotted curves) [10, 27, 205, 206, 210] within E, MM or superconducting DFT (SCDFT).
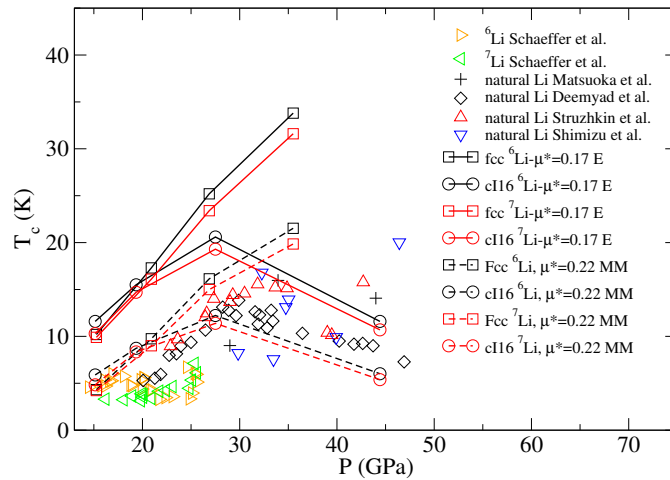
(b) Estimated T_c of fcc and $cI16$ lithium for its two stable isotopes at different pressures (lines with symbols) and comparison with experimental values (characters) [7–9, 11, 201].

Figure 10.6: T_c estimations and comparison with (a) previous theoretical and (b) experimental results.

underestimate λ due to the absence of $\mathbf{q}_{inst}$ in the grid. Including this extremely anharmonic point is crucial for estimating the impact of anharmonicity in the electron-phonon coupling and, as a consequence, the superconducting T_c. Fig. 10.6 shows the superconducting critical temperature of fcc lithium for both isotopes at 15, 20, 26 and 36 GPa. We find T_c increases monotonically with pressure the same way λ does, ranging from 11.2 K (10.7 K) at 15 GPa to 34.8 K (32.5 K) at 36 GPa for ^{6}Li (^{7}Li). Our T_c values are larger than in previous works as in the case of λ. However, they compare better to literature and experiments if we use McMillan's formula with $\mu^* =$0.22.

10.1.2   cI16 structure

Harmonic dynamical matrices have been obtained in a $6 \times 6 \times 6$ $\mathbf{q}$-grid for every analyzed pressure and isotope. For this crystal structure, a proper convergence of phonon frequencies required a $16 \times 16 \times 16$ $\mathbf{k}$-point grid and Methfessel-Paxton smearing width of 0.01 Ry for electronic integrations in the first BZ. An energy cutoff of 65 Ry was necessary for expanding the wave-functions in the plane-wave basis. In Fig. 10.7 we show the phonon spectra obtained at 15,19, 27 and 44 GPa for ^{6}Li after Fourier interpolating the dynamical matrices from the $6 \times 6 \times 6$ grid to the desired path. We can see that phonons do not show any remarkable feature, as they are positive and well-behaved all over the BZ.

Anharmonic dynamical matrices were obtained in a $2 \times 2 \times 2$ $\mathbf{q}$-grid, commensurate to the supercell in which the SSCHA was performed. We interpolated the results to the finer $6 \times 6 \times 6$ grid with the same method as in the fcc case. In this case anharmonicity has practically no influence on phonon frequencies at 27 and 44 GPa, while at 15 and 19 GPa low frequency modes are more noticeably affected. We can see this in Fig. 10.7 for ^{6}Li (we do not show the result for ^{7}Li as they are practically identical).

Converging the double Dirac delta in the equation for the phonon linewidth required a $32 \times 32 \times 32$ $\mathbf{k}$-point mesh. The superconducting T_c was calculated solving isotropic Eliashberg equations. Converging T_c within 1 K required to calculate the electron-phonon matrix elements in a $6 \times 6 \times 6$ $\mathbf{q}$-point grid (see Fig. 10.4b).

The cI16 structure (space group $I\bar{4}3d$) has all the Li atoms placed in the Wyckoff 16c positions (conventional coordinates (x, x, x) and all symmetry equivalent), which has a free parameter x. As the SSCHA minimization of the free energy is also performed with respect to x, final average atomic positions are different from the harmonic or static ones. In principle, one should perform the electron-phonon coupling calculations in the new anharmonic atomic positions for each isotope and
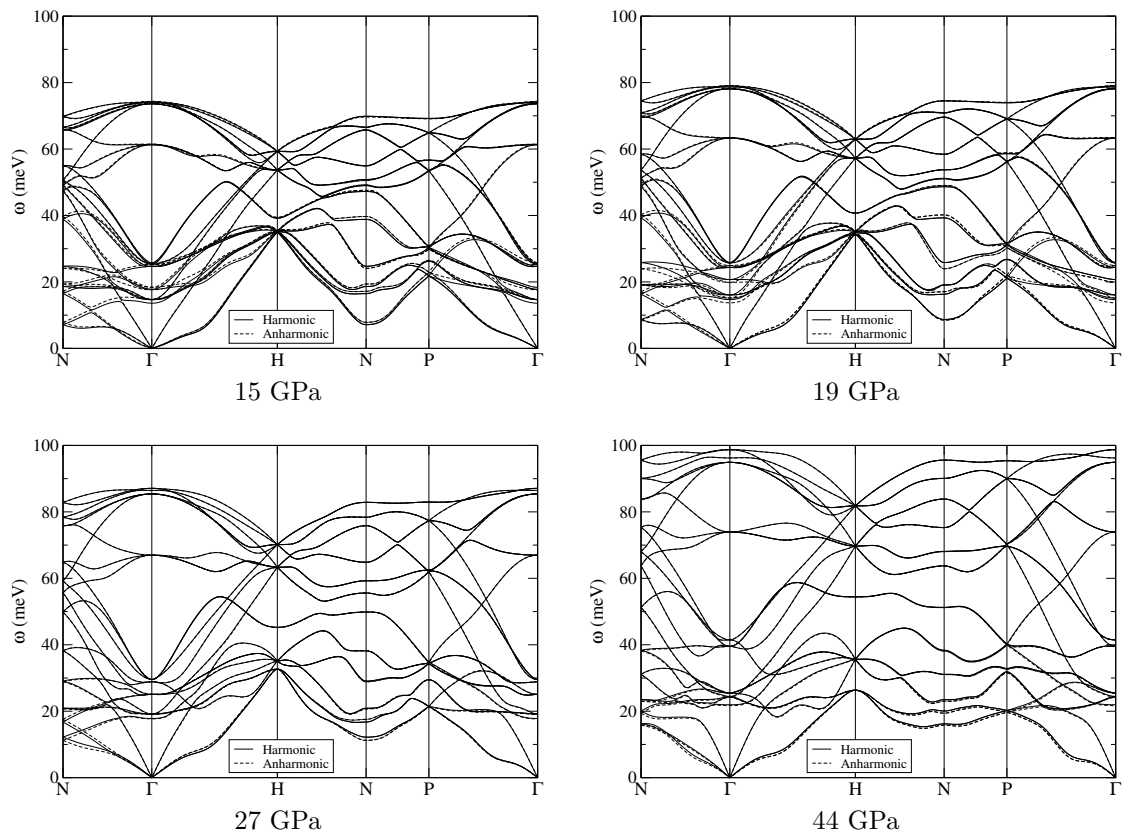
Figure 10.7: Phonon spectra of *cI*16 ^{6}Li at different pressures.

pressure. However, we checked that the impact on λ and T_c for ^{6}Li at 19 GPa, where the change in x due to anharmonic effect is the greatest ($\Delta x =0.004$) is within the convergence criteria. Therefore, we use the electron-phonon coupling calculation calculated at the static equilibrium positions at each pressure for both isotopes.

In Fig. 10.5 we show the total electron-phonon coupling λ for cI16 Li at 15, 19, 27 and 44 GPa. λ does not vary with pressure as much as it does in the fcc phase, as it varies only between 0.9 and 1.2 in the 15-44 GPa pressure range. λ is fairly similar for both isotopes, so anharmonicity does not have almost any impact. Still, at the lowest pressures, cI16 values differ more than the fcc ones from one isotope to the other. This is due to the fact that, while the overall phonon spectrum is very slightly modified by anharmonicity in the cI16 phase, anharmonic corrections occur mostly at the lowest frequencies, which are the ones that contribute the most to the total electron-phonon coupling. In fact, our λ and T_c estimations with μ^*=0.17 shown in Figs. 10.5 and 10.6 yield values higher than in fcc below 20 GPa, being the opposite at higher pressures.

10.2   Enthalpy calculations

Since the temperature of the systems under analysis is below 30 K (2.5 meV), which is the maximum estimated T_c, and the typical phonon frequencies are of the order of tens of meVs, the phonon occupation of the system will always be negligible and so will be the entropic contribution to the vibrational free energy. The same holds for the electronic entropy, even in a more obvious way, with typical electronic energies being of the order of eVs. Therefore, all our calculations will be at zero temperature and, therefore, the thermodynamically stable structure at each pressure will be the one that minimizes the total enthalpy of the system

$$H = E_T + PV. \tag{10.2}$$

where V is the volume of the system, $E_T = U_0 + E_v$ is the total energy and $U_0 = U(\tilde{\mathbf{R}}^0)$ and E_v are the electronic and vibrational energies, respectively. The pressure of the system is defined as

$$P = -\frac{\partial E_T}{\partial V}. \tag{10.3}$$

We calculated each contribution to the total energy $E_T = U_0 + E_v$ at several unit-cell volumes and fitted them separately, due to the fact that the computational

cost of a data point differs significantly from one contribution to another, as U_0 is faster to compute than E_v, which is calculated within the SSCHA as it is the $T = 0$ limit of Eq. (3.48).

We calculated U_0 for fcc and $cI16$ Li for volumes ranging from 50 to 100 a_0^3/atom with a step size of approximately 1.5 a_0^3/atom. We fitted the data using a Birch-Murnaghan equation of state [214]. Due to the different properties of the phonon spectra, the vibrational contribution required a different treatment for each crystal structure. Taking the $T = 0$ limit of Eq. (3.48) we write the vibrational contribution to the energy as $E_v = E_{freq}+ < U - \mathcal{U} >$ [93], where E_{freq} comes from the sum of the SSCHA frequencies over all the modes of the crystal and $< U - \mathcal{U} >$ comes from the difference of the actual anharmonic energy surface and the SSCHA harmonic one. E_{freq} can be further splitted into the harmonic contribution and the anharmonic correction, $E_{freq} = E_{har} + E_{anh}$, where E_{har} is the energy coming from the harmonic frequencies and E_{anh} is their anharmonic correction.

For $cI16$ calculating harmonic dynamical matrices in a $2 \times 2 \times 2$ **q**-grid was enough to converge E_{har} within 0.5 meV/atom (see Fig. 10.4d). We calculated E_{har} at seven different volumes, from 50 to 100 a_0^3/atom, and fitted a fourth order polynomial to the data points. We calculated E_{anh} and $< U - \mathcal{U} >$ at four different volumes (60,70,80 and 84 a_0^3/atom) by performing SSCHA calculations in $2 \times 2 \times 2$ supercells, and fitted the data with a second order polynomial.

Fcc Li presents a more complex situation due to the anomaly in the ΓK path. We computed E_{har} using a $8 \times 8 \times 8$ grid, which does not show any imaginary frequency down to at least 65 a_0^3/atom (which corresponds to around 35 GPa), and converges E_{har} within 0.2 meV/atom (see Fig. 10.4c). We calculated E_{har} at seven different volumes, from 50 to 100 a_0^3/atom, and fitted a fourth order polynomial to the data points. To estimate the anharmonic contribution, we performed SSCHA calculations to obtain anharmonic dynamical matrices and $< U - \mathcal{U} >$ in a $3 \times 3 \times 3$ grid for four different volumes (66,72,77 and 84 a_0^3/atom). To overcome the situation of using different grids for each contribution of the vibrational energy, we needed to treat E_{anh} carefully. We interpolated our anharmonic dynamical matrices from the $3 \times 3 \times 3$ grid to a finer $9 \times 9 \times 9$ to obtain E_{freq}, and subtracted the harmonic contribution in a $8 \times 8 \times 8$ grid as $E_{anh} = E_{freq} - E_{har}$, as imaginary frequencies prevent us obtaining E_{har} in a $9 \times 9 \times 9$ grid. Finally, we fitted these four data points with a second order polynomial.

For $hR1$ we have proceeded in a different way due to the fact that it shows plenty of imaginary frequencies in the harmonic phonon spectra (see Fig. 10.8). These imaginary frequencies are strongly renormalized by anharmonicity and become real after applying the SSCHA in a $2 \times 2 \times 2$ **q**-grid. However, the interpolation
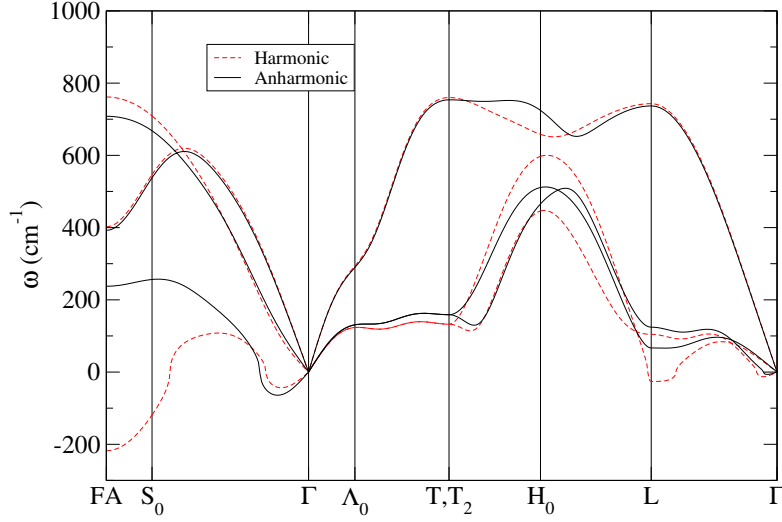
Figure 10.8: Phonon spectra of $hR1$ ^{7}Li at around 40 GPa. Harmonic dynamical matrices have been explicitly calculated in a $6 \times 6 \times 6$ **q**-grid, while the anharmonic ones have been calculated in a $2 \times 2 \times 2$ grid and interpolated to the finer $6 \times 6 \times 6$ grid afterwards. The harmonic spectrum shows phonon instabilities in large regions of the BZ. Anharmonicity renormalizes strongly those instabilities, yielding real frequencies for every **q**-point in the $2 \times 2 \times 2$ grid. However, after interpolating to the $6 \times 6 \times 6$ grid some modes remain unstable.

method was not useful in this case as some of the interpolated anharmonic matrices in a $6 \times 6 \times 6$ remained yielding imaginary frequencies. We overcame this situation making use of the similarity of $hR1$ with the fcc phase. If one chooses a rhombohedral unit cell, $hR1$ differs from fcc only by the rhombohedral angle θ. Thus, taking θ and the unit cell volume V as variables, we can focus our attention to their associated potential energy surface. We define the total energy as $E_T(\theta, V) = E_{T,fcc}(V) + \Delta E(\theta, V)$, where $E_{T,fcc}(V)$ is the total energy of the fcc phase ($\theta =60^\circ$) and $\Delta E(\theta, V)$ is the difference in energy due to the change in the rhombohedral angle. We only need to calculate $\Delta E(\theta, V)$ in this case as we had previously calculated $E_{T,fcc}(V)$. $\Delta E(\theta, V)$ is the sum of electronic and vibrational contributions. The electronic contribution $\Delta U_0(\theta, V)$ is easily obtained by DFT total energy calculations. For obtaining the vibrational contribution $\Delta E_v(\theta)$ we assumed that it is independent of the unit cell volume. This way, we performed SSCHA calculations in $2 \times 2 \times 2$ supercells at four different $\cos(\theta)$ values $(0.25, 0.35, 0.412$ and $0.5)$ for a single volume $(60 \ a_0^3/\text{atom})$ and fitted it with a 3rd order polynomial. In Fig. 10.9 we show $\Delta E(V, \theta)$ against θ for different choices of the unit cell volume V, which is kept constant in each curve. Two relative minima can be distinguished below 70 a_0^3/atom: one at $\cos \theta = 0.5$, which corresponds to
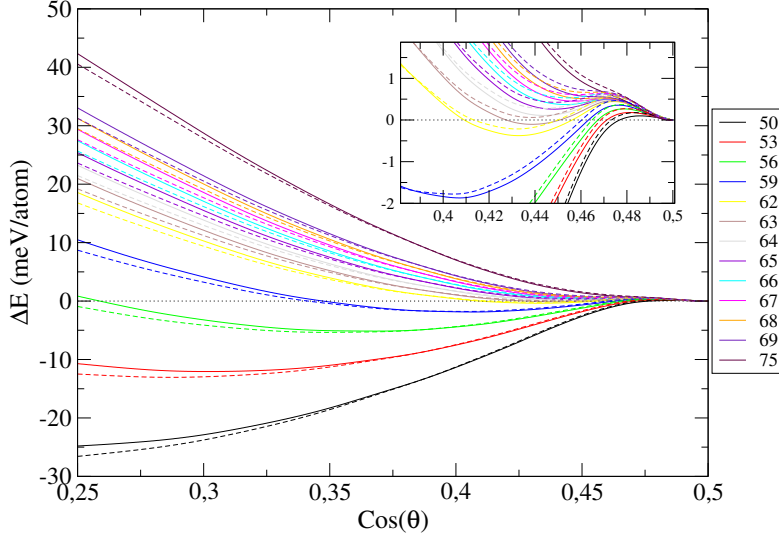
Figure 10.9: $\Delta E(\theta, V)$ against $\cos(\theta)$ for different unit-cell volumes (in a_0^3/atom). In the dashed curves vibrational energy is not included.

the fcc structure, and another one corresponding to the $hR1$ phase, which even has a lower energy than the previous one for volumes smaller than 63 a_0^3/atom. Plus, the angle at which this minimum occurs increases with decreasing volume. Above 70 a_0^3/atom, which corresponds to pressures below 28 GPa, $hR1$ could not exist as it lacks of a local energy minimum.

In Fig. 10.10 we show the pressure vs. volume curves for each isotope and structure, obtained by taking the first derivative of E_T with respect to the volume. According to the graph, our relative enthalpy calculations should be trustworthy at least between 15 and 50 GPa.

Fig. 10.11 shows the enthalpies of the competing phases $cI16$ and $hR1$ relative to their respective fcc ones for the two isotopes. Our static calculations, *i.e.* not including E_v (which at $T = 0$ is the ZPE), compare well with literature (there are no previous works including ZPE) [209] and just show the fcc to $cI16$ transition. No important changes are shown for both isotopes when anharmonic ZPE is included and, although in the pressure range where this phase transition happens the enthalpy difference with the $hR1$ is less than 1 meV/atom, that is, roughly the same as the error one assumes when converging total energy calculations within DFT, it remains metastable. Therefore, small changes in the calculation parameters or the choice of exchange and correlation potential might cause modifications in the transition pressures and phase sequence. Accordingly, when ZPE is included the fcc to $cI16$ transition pressure shifts from 37 GPa to 33 GPa for both isotopes,
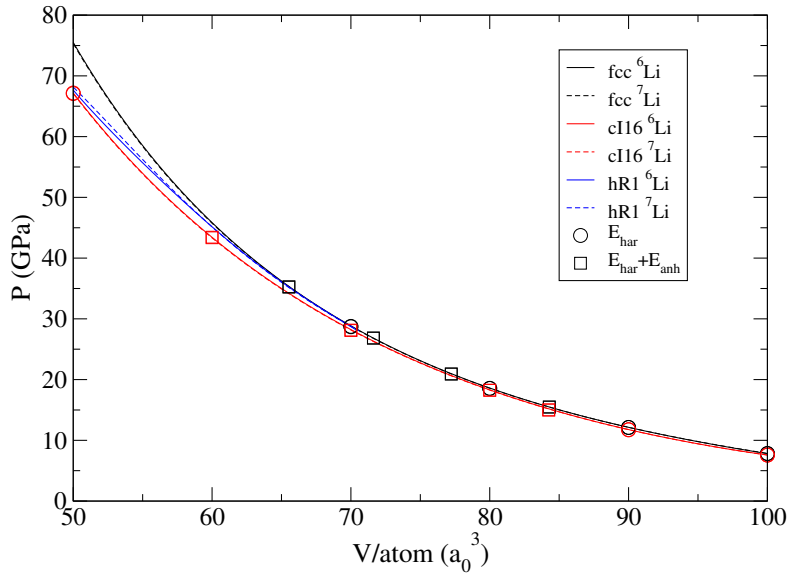
Figure 10.10: Pressure of fcc, $cI16$ and $hR1$ Li for both isotopes. The symbols show data points in which harmonic (E_{har}) and anharmonic (E_{anh}) vibrational data has been explicitly calculated.

as the enthalpy difference is reduced by around 3 meV due to lattice vibrations. Additionally, in the 21-25 GPa pressure range, where the inverse isotope effect was observed, the enthalpy difference between $cI16$ and fcc structures is really small (around 4-6 meV/atom).

10.3   Discussion on the isotope effect

First of all, we discarded an isotope dependent μ^* as the source of the anomalous isotope effect. Changes in phonon frequencies and electronic density for different pressures and isotopes only alter the fourth significant digit of μ^*, so that differences in μ^* cannot explain the isotope effect anomalies and we assume the same value for every isotope and pressure.

In Fig. 10.12 we show our calculated α values against pressure using our T_c estimations of fcc Li. We do not see any anomalous scaling of the superconducting temperature with the isotopic mass, as α is close to the conventional harmonic BCS value of 0.5 within almost the entire pressure range. It is true that at 15 GPa it shows a lower value. However, it does not, in any case, explain the experimentally observed anomalous isotope effect. The reason for a normal isotope
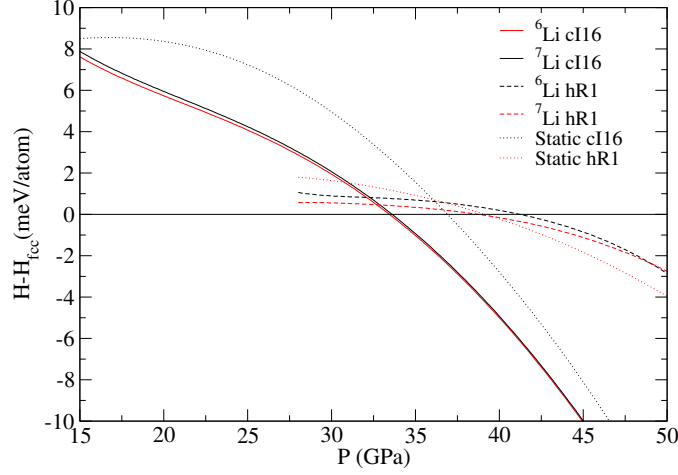
Figure 10.11: Relative enthalpies of $cI16$ and $hR1$ ^{6}Li and ^{7}Li isotopes with respect to their fcc counterparts. In solid and dashed lines E_v has been included, while in dotted curves only electronic energy has been considered. The low pressure limit for the $hR1$ curves has been set at the pressure which corresponds, in each case, to the maximum volume at which the phase shows a local minimum in the total energy surface (see Fig. 10.9).

effect in our calculation is the way the anomalous phonon frequency scales with isotopic mass. As it is shown in the inset of Fig. 10.2, even though this soft mode shows huge anharmonic effects, its frequency scales practically as in the harmonic case ($\omega \propto \sqrt{1/M}$). This makes λ nearly identical for both isotopes at every pressure except at 36 GPa, where the difference is just 7% even if anharmonicity is already really strong as shown in Fig. 10.2. A similar harmonic mass scaling was previously calculated for high pressure simple cubic calcium despite being strongly anharmonic [208].

As using McMillan's formula with μ^* =0.22 T_c compares better with literature and experiments, we show the corresponding α values in Fig. 10.12 as well. In any case, α does not almost change, and the conclusion remains unaltered. The overestimation of T_c in our calculations could also indicate that vertex corrections in the electron-phonon coupling and anisotropic effects in the Eliashberg equations might be important. However, anisotropic effects should not be isotope dependent and, due to the harmonic scaling of phonon frequencies, we do not expect vertex corrections to yield any anomalous isotope effect either. Therefore, we discard hypothesis (i).

After discarding that the anomalous isotope effect comes from strong anharmonicity in the fcc phase, we analyze the possibility of the two isotopes showing different
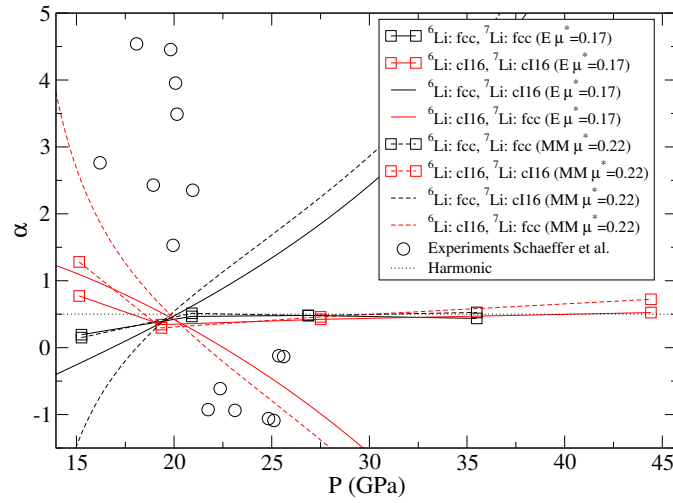
Figure 10.12: The isotope coefficient α against pressure. Lines with symbols show the coefficients obtained for the cases in which the two isotopes adopt the same crystal structure (either $cI16$ or fcc). Curves without symbols show the coefficients for the cases in which the isotopes adopt different structures. Circles show the experimental results from Ref. [9].

structures at the same pressure in a thermodynamically stable way. As we saw in section 10.2, our results do not support hypothesis (ii) as ^{6}Li and ^{7}Li isotopes are not expected to adopt different stable crystal structures in the pressure range of interest.

However, due to the extremely small enthalpy differences metastability of phases cannot be discarded as it happens at ambient pressure for its martensitic transition [203]. In order to see if ^{6}Li and ^{7}Li adopting different structures could lead to the observed anomalous isotope effect, we have also made lattice dynamics and electron-phonon coupling calculations in the $cI16$ structure. We do not further consider $hR1$ as a candidate because, as we saw in section 10.2, the local minimum in the total energy surface associated to $hR1$ disappears for pressures lower than 28 GPa.

In Fig. 10.12 we can see the isotope effect coefficient against pressure in the case both isotopes adopt the $cI16$ structure. The values are close to the harmonic value at 27 and 44 GPa, with α =0.42 and 0.57, respectively. However, they deviate considerably from 0.5 at 15 and 19 GPa as α yields 0.77 and 0.34, respectively, due to the higher anharmonicity we found at lower pressures. Nevertheless, this scenario does not still give an explanation to the experiments.

Finally, we have also analyzed this metastability driven hypothetical scenario: ^{6}Li

stabilizing in the fcc phase and ^{7}Li in the $cI16$, and vice versa. In these cases T_c vs. P data points have been obtained at different pressures for each isotope. Thus, we have fitted second order polynomials to overcome this situation. As shown in Fig. 10.12, in the pressure range where the inverse isotope effect was experimentally observed (21-25 GPa), experimental values would only be qualitatively reproduced if ^{6}Li adopted the $cI16$ structure while ^{7}Li were in the fcc phase. This qualitative picture does not vary much if one uses the McMillan formula with $\mu^* = 0.22$, but it could notably change if we used different μ^* values for the different phases.

10.4   Conclusions

According to our calculations, even though anharmonicity is crucial to stabilize the fcc phase in lithium under pressure, its λ remains almost the same for both isotopes and yields a conventional scaling of T_c with isotopic mass. Therefore, it does not explain the experimentally observed anomalous isotope effect.

On the other hand, including anharmonic ZPE in the enthalpy curve does not modify the phase diagram of lithium in the pressure range of interest, so that it is unexpected to have both isotopes in different structures in a stable regime. The anomalous isotope effect could only be qualitatively explained if ^{7}Li adopted the fcc structure while ^{6}Li adopted the $cI16$ one in a metastable way.

All this, added to the large error bars and quite chaotic behavior of T_c with pressure in Ref. [9]–with considerably different temperature values for the same pressure– puts in question the experimental observation of an anomalous isotope effect in lithium at high pressure. This way, our work encourages further experimental research to determine the phase sequence and superconducting properties of the two stable isotopes of lithium.

Conclusions

The main goal of this thesis was to provide an accurate theoretical description of lithium and hydrogen at high pressures focusing on the regions of their respective phase diagrams where the superconducting properties, which are still potential in the case of hydrogen, emerge. With this in mind, we have presented electronic and vibrational spectra along with the coupling between the electronic and nuclear sub-systems in order to obtain the superconducting properties of the analyzed materials. While our calculations rely on the DFT framework, we have accurately included the quantum behavior of the nuclei and anharmonic effects arising due to the lightness of the elements. For that purpose, we have used the SSCHA [93, 94], which accounts for quantum nuclear and anharmonic effects in a non-perturvative variational way.

Even though this thesis has mostly revolved around superconductivity and the effects of pressure in this fascinating property, we have seen pressure alters many other properties of high pressure hydrogen and lithium. Despite some of these effects were expected prior to performing the calculations, others took us by surprise and required a careful analysis. Given that we have already drawn conclusions for each of the systems we have analyzed at the end of their corresponding chapters, here we will give some remarks about what we consider relevant, expected or unexpected, phenomena emerging under pressure.

From a purely uniform electron gas approximation, metals are expected to become more free-electron-like as the pressure is increased. This is because the kinetic energy of electrons increases faster with pressure than the opposite sign electron-electron repulsion. In fact, this is what we saw in the case of atomic $I4_1/amd$ hydrogen, where the band-structure is properly represented if one neglects the electron-electron interaction. However, due to the lack of core-electrons in hydrogen the electron-nuclei interaction is particularly strong and must therefore be included, as it induces large band-gaps wherever the Fermi sphere touches the BZ boundaries. In fact, the lack of core electrons has crucial effects on the electronic screening as well, which we did not expect *a priori*, making the RPA fail due to the large self-interaction error of the Hartree term. These deviations from the free-electron model are more evident in the molecular $Cmca - 4$ phase, where the Fermi surface complexity is strongly pressure dependent. The reason is that electron and hole pockets are created as the hydrogen molecules stretch with increasing pressure.

In principle, phonon frequencies are expected to rise as the pressure is increased. This can be expected since, as the interatomic distance is reduced, the forces acting on atoms get stronger. However, we have seen that lithium, in its simple fcc structure, clearly deviates from this picture. Its phonon softening, even if strongly renormalized by anharmonic effects, reduces its frequency as the applied pressure

is increased. Lattice dynamics and anharmonicity have strong implications on the phonon frequencies of molecular hydrogen too, but the effects are specially relevant in its crystal structure. As pressure stretches the hydrogen molecules, vibronic frequencies are expected to get lower, and the $Cmca - 4$ structure is not an exception. On top of that, anharmonic effects stretch the molecules even further. This reduces significantly the pressure needed for filling the electron and hole pockets in the Fermi surface which are responsible of the high superconducting T_c. In fact, these strong anharmonic effects were expected considering lithium and hydrogen are extremely light elements. However, we did not expect the very little impact of anharmonicity in atomic hydrogen. Even though it is true that the phonon spectrum was significantly affected by anharmonic effects, the changes inflicted in the physical properties of atomic hydrogen are merely quantitative.

According to our results, hydrogen and lithium are great examples of pressure enhanced superconductivity. However, it is the impact of anharmonicity in the superconducting T_cs of atomic and molecular hydrogen which draws our attention. While the general trend in hydrides is to reduce or even suppress superconductivity, anharmonicity even increases T_c in $Cmca - 4$ hydrogen thanks to the electron and hole pockets created at the Fermi level as the molecules are stretched. On the other hand, the reduction of T_c in the $I4_1/amd$ atomic phase due to anharmonic effects is negligible. When anharmonicity is related to soft modes, as it is the case of lithium and of many hydrides [93, 94, 102, 157, 158], the general trend is that anharmonicity hardens these modes and therefore it reduces the T_c. However, in the absence of soft modes, as in atomic hydrogen, or in molecular systems where anharmonicity may stretch the molecules and soften the vibrons, a different behavior should be expected. The fact that anharmonicity does not necessarily handicap superconductivity is great news, indeed.

The electronic, vibrational and superconducting features of the systems analyzed in this thesis lead to interesting and useful fingerprints on their optical spectra. The presence of non-free-electron-like plasmons in lithium and in other alkali metals was already known [185, 194–198]. Our results show hydrogen, once metallized under pressure, would have a similar behavior to the rest of the alkalis in that sense. Furthermore, its huge electron-phonon coupling and high temperature superconductivity would also have notorious implications in its optical response, which would help in characterizing this material.

This thesis has been strongly influenced by two experimental papers, one for each of the elements under analysis. In this aspect, our objective was to give some answers to the hypotheses presented in these works. In "*High-pressure superconducting phase diagram of 6 Li: Isotope effects in dense lithium*" [9], Schaeffer *et al.* claimed they have measured an anomalous, even inverse at some pressures,

isotope effect in lithium in the 15-26 GPa range. Their main hypothesis is that anharmonic lattice vibrations cause this anomaly as it is the case in PdH [94]. They also suggest an isotope dependent crystal structure could be the origin of the anomaly, even though they do not show any structural characterization measurement. Our results clearly discard the first hypothesis, and do not support the latter either. Though metastability of phases could be behind what it was seen in the experiments, our calculations put in doubt the experimental results and, therefore, encourage their reproduction and further diffraction experiments in order to confirm the crystal structure of lithium in the pressure range of interest. The paper "*Observation of the Wigner-Huntington transition to metallic hydrogen*" by Dias and Silvera [138] has been one of the most important but controversial scientific publications in recent years. The claim of having produced a metallic hydrogen sample sparked strong criticism regarding how pressure was determined in the experiment and the lack of sophistication of the used optical characterization technique [165–168]. According to our calculations, pressure, while extremely important as it determines the crystal structure, does not modify the optical properties of metallic hydrogen within each of the most probable phases. Moreover, the experimental electronic scattering rates are not far from our estimated values, supporting that the $I4_1/amd$ atomic phase could be behind the measurements. However, the temperature dependence of the measurements cannot be explained by our calculations and we show the amount of experimental points presented by Dias and Silvera are clearly not enough. Moreover, using the Drude model for characterization is probably a too simple theoretical approach. In any case, it seems that experimentalists are already able to obtain the pressures necessary to metallize hydrogen and the confirmation of metallization of hydrogen looks closer than ever. Hopefully, our contribution will be helpful to guide present and future experiments.

Appendices

Appendix A

Components of the dynamical matrix

The dynamics of a crystal lattice in the harmonic approximation are solved by diagonalizing the dynamical matrix of the system. According to Eq. (3.25) the force constant matrix is splitted into the nuclei-nuclei (the last term) and nuclei-electron contributions (the first two terms). The dynamical matrix can therefore be splitted accordingly:

$$D(\mathbf{q}) = D_p(\mathbf{q}) + D_e(\mathbf{q}), \tag{A.1}$$

where D_p accounts for the nuclei-nuclei contribution and D_e for the nuclei-electron contribution. The electronic part can be computed within the RPA using the Lindhard formula in which, assuming a constant free electron density, after Fourier transforming Eq. (3.25) and dividing it by $\sqrt{m_s m_{s'}}$, one obtains

$$
\begin{aligned}
D_{e\,ss'}^{ll'}(\mathbf{q}) &= \frac{1}{\sqrt{m_s m_{s'}}\Omega_{cell}} \sum_{\mathbf{kG}} (\delta_{\mathbf{k},\mathbf{q}+\mathbf{G}} - \delta_{s,s'}\delta_{\mathbf{k},\mathbf{G}}) \frac{\chi_0(\mathbf{k})}{1 - \frac{4\pi}{k^2}\chi_0(\mathbf{k})} \\
&\times\ V_c^s(\mathbf{k}) V_c^{s'}(\mathbf{k}) k^l k^{l'} e^{i\mathbf{k}\cdot(\boldsymbol{\tau}_s - \boldsymbol{\tau}_{s'})},
\end{aligned}
\tag{A.2}
$$

where the index s holds for the atoms in the unit cell and l for the three cartesian axes. $V_c^s(\mathbf{k}) = -4\pi Z_s/|\mathbf{k}|^2$ is the Coulomb potential in momentum space created by a nuclei with index s and charge Z_s.

The ionic part is always analytic, and one needs to use the Ewald summation method to deal with the convergence issues emerging from the long range behaviour of the Coulomb interaction [215]. If the ionic total energy is split into short and long range contributions, the ionic contribution to the dynamical matrix will

consist of

$$D_{p\,ss'}^{ll'}(\mathbf{q}) = D_p^{long\,ll'}{}_{ss'}(\mathbf{q}) + D_p^{short\,ll'}{}_{ss'}(\mathbf{q}), \tag{A.3}$$

where

$$D_p^{long\,ll'}{}_{ss'}(\mathbf{q}) \;=\; \frac{1}{\sqrt{m_s m_{s'}}} \sum_m e^{-i\mathbf{q}\cdot\mathbf{T}_m} \frac{\partial^2 V_{I,I}^{long}(\mathbf{R})}{\partial u_{ms}^l \partial u_{0s'}^{l'}}\bigg|_{\mathbf{R}^0} \tag{A.4}$$

$$D_p^{short\,ll'}{}_{ss'}(\mathbf{q}) \;=\; \frac{1}{\sqrt{m_s m_{s'}}} \sum_m e^{-i\mathbf{q}\cdot\mathbf{T}_m} \frac{\partial^2 V_{I,I}^{short}(\mathbf{R})}{\partial u_{ms}^l \partial u_{0s'}^{l'}}\bigg|_{\mathbf{R}^0}. \tag{A.5}$$

The long range contribution is computed in momentum space and reads as

$$D_p^{long\,ll'}{}_{ss'}(\mathbf{q}) \;=\; \frac{1}{\sqrt{m_s m_{s'}}\,\Omega_{cell}} \sum_{\mathbf{G}} \sum_{\mathbf{k}} (\delta_{\mathbf{k},\mathbf{q}+\mathbf{G}} - \delta_{s,s'}\delta_{\mathbf{k},\mathbf{G}}) \frac{4\pi Z_s Z_{s'}}{|\mathbf{k}|^2} k^l k^{l'} \times$$

$$\times\; e^{i\mathbf{k}\cdot(\boldsymbol{\tau}_s - \boldsymbol{\tau}_{s'})} e^{-\mathbf{k}^2/4\gamma}. \tag{A.6}$$

The short-range contribution is computed in real space as

$$\frac{\partial^2 V_{I,I}^{short}(\mathbf{R})}{\partial u_{ms}^l \partial u_{0s'}^{l'}}\bigg|_{\mathbf{R}^0} = -Z_s Z_{s'} \frac{\partial^2 \phi^{short}(\mathbf{x})}{\partial x^l \partial x^{l'}}\bigg|_{\mathbf{x}^0}, \tag{A.7}$$

where

$$\phi^{short}(\mathbf{x}) = \frac{\mathrm{erfc}(\sqrt{\gamma}|\mathbf{x}|)}{|\mathbf{x}|} \tag{A.8}$$

and the second derivatives have to be evaluated at

$$\mathbf{x}_{mss'}^0 = \mathbf{T}_m + \boldsymbol{\tau}_{s'} - \boldsymbol{\tau}_s. \tag{A.9}$$

Making use of the properties of the complementary error function it can be shown that the derivatives of the potential look like

$$\frac{\partial^2 \phi^{short}}{\partial x^l \partial x^{l'}}(\mathbf{x}) \;=\; Z_s Z_s' \frac{x^l x^{l'}}{|\mathbf{x}|^2} \left[\left(4\gamma + \frac{6}{|\mathbf{x}|^2} \right) \sqrt{\frac{\gamma}{\pi}} e^{-\gamma|\mathbf{x}|^2} + \frac{3\,\mathrm{erfc}(\sqrt{\gamma}|\mathbf{x}|)}{|\mathbf{x}|^3} \right]$$

$$-Z_i Z_j \frac{\delta_{ll'}}{|\mathbf{x}|^2} \left[2\sqrt{\frac{\gamma}{\pi}} e^{-\gamma|\mathbf{x}|^2} + \frac{\mathrm{erfc}(\sqrt{\gamma}|\mathbf{x}|)}{|\mathbf{x}|} \right]. \tag{A.10}$$

The γ parameter can help to speed up the convergence and, obviously, the final result must be independent of the chosen value.

Appendix B

Interpolation of SSCHA dynamical matrices

In the SSCHA forces are calculated in supercells and, therefore, anharmonic dynamical matrices are obtained in a commensurate $\mathbf{q}$-point grid. Computational costs increase enormously with the supercell size making dense sampling calculations extremely time-demanding. Therefore, whenever a fine sampling of the BZ is required, we have used the following interpolation scheme.

Let us call the anharmonic dynamical matrices obtained in the output of the SSCHA calculation in a coarse $\mathbf{q}$-point grid (small supercell) $D^{coarse}_{SSCHA}(\mathbf{q})$. We will name the harmonic dynamical matrices obtained in the same grid as $D^{coarse}_{har}(\mathbf{q})$. Our goal is to obtain anharmonic dynamical matrices in a finer grid, written as $D^{fine}_{SSCHA}(\mathbf{q})$, by taking advantage of having the fine grid harmonic dynamical matrices $D^{fine}_{har}(\mathbf{q})$ already computed (which are faster to obtain than the anharmonic ones). Assuming that

$$\widetilde{D}^{coarse}(\mathbf{q}) \equiv D^{coarse}_{SSCHA}(\mathbf{q}) - D^{coarse}_{har}(\mathbf{q}) \tag{B.1}$$

is slowly varying in the reciprocal space (*i.e.* the differences between the SSCHA and the harmonic force constant matrices are more localized in real space than the harmonic force constant matrices) we can interpolate $\widetilde{D}^{coarse}(\mathbf{q})$ using Fourier interpolation to the fine grid of our choice to obtain $\widetilde{D}^{fine}(\mathbf{q})$. Now, it is straightforward to obtain

$$D^{fine}_{SSCHA}(\mathbf{q}) = D^{fine}_{har}(\mathbf{q}) + \widetilde{D}^{fine}(\mathbf{q}). \tag{B.2}$$

Laburpena

Laburpena (summary in Basque)

Hidrogenoa eta litioa taula periodikoko elementu sinpleak dira, euren propietateak giro presio eta tenperaturan oso ezagunak direlarik. Hidrogenoa gas diatomiko molekularra da eta litioa elektroi askeen ereduarekin erraz azal daitekeen metal arrunta. Muturreko baldintzatan, ordea, ustekabeko portaera agertzen dute. Material hauek presio oso altuetan daukaten portaera aztertzea da, hain zuzen, doktoretza tesi honen helburua. Horretarako dentsitatearen funtzionalen teoria (DFT) erabili dugu.

Presioak eta tenperaturak materian duten eragina egunerokotasunean ikus daiteke, eta ura da horren adibide on bat. Urak giro presioan 100 ºC-tan irakiten du, lurrun bilakatuz. Presioa igoz gero, ordea, tenperatura altuagoa behar du irakiteko. Hau da, hain zuzen, presio-eltzearen oinarria, tenperatura altuago honi esker egosten baita bertan sartzen dugun janaria azkarrago. Beste muturrean, presioa asko jaitsiz gero ura lurrun bihur daiteke tenperatura baxuetan ere. Logika berdina jarraituz, izotza sortzeko ere bi aukera daude: ohiko modua, ura zero gradura hoztea, eta ez-ohiko modua, presioa izugarri handitzea, 10000 atmosfera ingurura.

Presio eta tenperatura oso altuetan materialen egitura eta propietateak zehazten dituzten lotura kimikoak ere alda daitezke, askotan aurresan ezin daitezkeen ondorioekin. Honela, presioa eta tenperatura materialen propietateak aldatzeko eta material berriak sortzeko tresna gisa ikus daitezke. Egoera solidoaren fisikan propietate aldaketak kristal-egitura aldaketekin batera agertzen dira maiz. Batzuetan, litioaren trantsizio martensitikoan kasu [1], tenperatura da aldaketaren eragilea. Bilatzen ari garen propietatea tenperatura baxukoa denean, ordea, presioa da aldaketak eragiteko egokiena.

Presiopean ezustean agertzen den propietateetako bat supereroankortasuna da. Elektroientzat Hartree-Fock eredua eta kristal sarearen bibrazioentzat (fonoi-entzat) eredu kuasi-harmonikoa onartuz gero, presioak supereroankortasunaren kontra egin beharko luke [2, 3]. Izatez, hori da supereroale konbentzional sinpleetan behatzen dena [4, 5]. Ostera, badira lege hau apurtzen duten material asko eta

asko, baita oso sinpleak direnak ere. Honela, giro presioan taula periodikoko 29 elementu badira supereroaleak, presiopean zenbakiak 54 arte egiten du gora [13]. Litioa, kasu, giro presioan supereroalea bada ere, oso tenperatura baxura hoztu beharra dago, bere supereroankortasun tenperatura kritikoa (T_c) 0.4 mK eskasekoa baita [6]. Presiopean, ordea, T_c-k bost magnitude orden egiten du gora, 20 K-era helduz 48 GPa-tan [7–12]. Hidrogenoa, oraindik esperimentu bidez konfirmatu ez bada ere, 55. elementua izan liteke. Wigner-ek 1935ean presiopean solido bihurtzeaz gain metal bihurtuko litzatekeela [14] aurresan eta urte batzuetara, Ashcroft-ek oso tenperatura altuko supereroalea ere izango litzatekeela iragarri zuen [15]. Duela gutxi sufre eta hidrogeno konposatu batean 150 GPa-tan 203 K-tako T_c-a neurtu izanak [16] Ashcroft-en ideiari berebiziko sinesgarritasuna eman zion.

Supereroankortasuna ez da, noski, presiopean ager daitekeen propietate bakarra. Adibidez, presioa igo ahala kristal egitura gero eta trinkoagoak espero badira ere, material batzuek kontrako joera agertzen dute, litioa adibide ona izanik [17–22]. Fase trantsizio horiei lotuta metaletik isolatzailerako trantsizioak edota tenperatura baxuko urtze prozesuak agertzen dira [23–26]. Egitura aldaketa horiek askotan fonoi ezegonkortasunei lotuta ageri dira, aldi berean supereroankortasuna bultzatu edo areagotzen dutenak [27–33].

Presio altuko materialen fisikan propietate aldaketak, normalean, gigapascal (GPa) eskalan ematen dira. Esperimentalki presio horiek lortzeko *diamond anvil cell* (DAC) izeneko gailuak erabiltzen dira, aztertu beharreko lagina bi diamanteren artean zapaltzen dutenak. Teknika oso garesti eta konplexua da eta, ondorioz, kalkulu teorikoek bereziko garrantzia daukate zientziaren arlo honetan. Zorionez, DFT kalkuluetan presioa erraz simulatu daiteke inongo kostu gaingarririk gabe, kristala definitzen duen gelaxka unitatearen bolumena nahieran aukera baitaiteke.

Tesia hiru ataletan banatuta dago. Lehenengo atalean kalkuluak burutzeko beharrezkoak izan diren oinarri teorikoak laburtu ditugu. Bigarren atala hidrogeno solidoari buruzko analisiari eskaini diogu. Azkenik, litioari buruzkoa hirugarren atalean bildu dugu.

Lehenengo atala, *Theoretical Background* izenekoa, bost kapituluz osaturik dago. Lehenengo kapituluan materiaren propietateak fisikaren ikuspuntutik aztertzeko beharrezkoa den gorputz anitzeko Hamiltondarra eta Schrödinger ekuazioaren formalismoa aurkeztu dugu, Born-Oppenheimer hurbilketaren bidez elektroi eta nukleo atomikoen azpisistemak bananduz. Bigarren kapituluan sistema elektronikoa ebazteko erabili dugun metodologia aurkeztu dugu, DFT-ren oinarriak azalduz. Hirugarren kapitulua sistema nuklearrari eskaini diogu, sare kristalinoaren bibrazioei hain zuzen. Hurbilketa harmonikoa aurkeztu dugu mekanika kuantikoaren

ikuspuntutik, fonoi kontzeptua sareen bibrazioen kuantu gisa definituz. Fonoiak kalkulatzeko dentsitatearen funtzionalen perturbazio teoria (DFPT) azaldu dugu, eta baita efektu anharmonikoak zer diren eta hauek nola kalkulatu hurbilketa harmoniko auto-bateragarri estokastikoa (SSCHA) deituriko metodoaren bitartez. Laugarren kapituluan elektroi eta fonoi azpisistemen elkarrekintza aztertu dugu, supereroankortasun konbentzionalaren oinarria dena, Migdal eta Eliashberg teoriak aurkeztuz. Azkenik, bosgarren kapituluan propietate elektronikoen denborarekiko menpekotasuna kontuan hartzen duen denboraren menpeko DFT (TDDFT) teoria azaldu dugu, metalen propietate optikoak aztertzeko erabilgarria dena.

Bigarren atala, *Solid Metallic Hydrogen* izenekoa, hidrogeno metalikoari buruzkoa da. Presio altuko hidrogenoak komunitate zientifikoaren interesa betidanik piztu badu ere, Ashcroft-en 1968ko iragarpenak nabarmen handitu zuen elementu honekiko arreta [15]. Ordutik zientzialari esperimentalek gero eta presio altuagoak lortu dituzte, hidrogeno solidoaren bost fase molekular eta isolatzaile topatuz 400 GPa-tik behera. Azken urteotan, ordea, presioa are gehiago igotzea lortu dute, metalizaziotik are eta gertuago egon litezkeen faseak topatuz [162–164]. Azkenik, pasa den urteko hasieran Dias eta Silverak hidrogeno metalikoa lortu eta neurtu zutela adierazi zuten Science aldizkarian argitaraturiko artikulu batean [138]. Hala ere, artikuluak kritika sakonak jaso zituen [165–168], presioa neurtzeko moduaz gain, lagina karakterizatzeko erabilitako teknika zalantzan jarriz.

Materialen kristal-egitura karakterizatzea ezinbestekoa da, propietate fisikoek egituraren menpekotasun handia baitaukate. Hidrogenoaren kasuan are gehiago, ez baitago batere argi metalizazioa egitura molekular batean edo molekula apurtu ondoren emango den, gainontzeko metal alkalinoen itxurako metal monoatomiko bat sortuz. Tamalez, hidrogenoan hain presio altuetan karakterizazio neurketak egitea oso zaila da neutroi eta X-izpien esperimentuak orokorrean ezin baitira burutu. Hortaz, hidrogenoaren fase ezberdinak determinatzeko kalkulu teorikoak ezinbestekoak dira. Fase gehienak infragorri (IR) xurgapen eta Raman esperimentuen bitartez detektatu dira eta fisikari teorikoek proposatutako hainbat kristal egituretan kalkulaturiko espektroekin konparatu dira ondoren. Dias eta Silveraren azken esperimentuan, ordea, espektro optikoa (islapena, konkretuki) neurtu dute, eta Drude eredu sinplearekin konparatu.

Hortaz, atal honetako gure helburua hidrogeno solidoaren propietate elektroniko, bibrazional eta optikoak metalizazio presio inguruan aztertzea izan da, hots, 400-600 GPa tartean. Konkretuki, bibliografiaren arabera egitura atomiko eta molekular probableenak aztertu ditugu, $I4_1/amd$ eta $Cmca - 4$, hurrenez hurren. Atalak hiru kapitulu dauzka, tesiko seigarrenetik zortzigarrenera bilduta.

Seigarren kapituluan $I4_1/amd$ egituraren propietate elektroniko eta bibrazionalak

aztertu ditugu 400-600 GPa tartean. Gure emaitzen arabera $I4_1/amd$ egituran elektroiek eredu asketik gertuko portaera dute, elektroi-elektroi elkarrekintzak ez baitauka banda egituran eraginik. Hala ere, elektroi-protoi elkarrekintza oso bortitza da, elektroiak partzialki lokalizatuz protoien inguruan. Lokalizazio honen ondorioz erantzun elektronikoa eta fonoiak kalkulatzean RPA ereduak kale egiten du. Arrazoia, Hartree eredua erabiltzean elektroi bakoitzak bere buruarekin daukan ekarpenaren errorea handia dela. Hortaz, truke eta korrelazio energia kontuan hartzea ezinbestekoa da fonoiak kalkulatzeko. Gainera, azken gai honi esker dira soilik fonoiak egonkorrak. Gure elektroi-fonoi kalkuluen arabera elektroien eta bibrazioen arteko elkarrekintza oso bortitza da, eredu harmonikoa erabiliz 320 K-eko T_c-a lortzen dugularik. Azkenik, SSCHA kalkuluen arabera efektu anharmonikoek ez daukate eragin handirik fonoietan ez baitute kualitatiboki ezer aldatzen eta T_c 300 K-era jaisten delako soilik. Aldaketa hau oso txikia da beste hidruro batzuekin konparatuz [93, 94, 102, 157, 158].

Zazpigarren kapituluan $Cmca-4$ egitura molekularra izan da aztertutakoa. Kasu honetan efektu kuantiko eta anharmonikoek propietate elektroniko eta bibrazionaletan eta supereroankortasunean daukaten eragina aztertu dugu 414 GPa eta 450 GPa-tan. Gure kalkuluetatik efektu anharmonikoek kristal egitura nabarmen aldatzen duela ondorioztatu daiteke, hidrogeno molekula %6 bat luzatzen delarik. Honek, aldi berean, ondorio azpimarragarriak dakartza banda egituran, Fermi gainazalean elektroi eta zulo poltsa berriak sortuz. Poltsa hauek elektroi-fonoi elkarrekintza indartzen dute eta, hori dela eta, T_c ia bikoiztu egiten da. Hurbilketa harmonikoarekin lortzen diren 100 K-etik gertuko balioetatik 200-K-etik gorako tenperaturetara igotzen da efektu kuantiko eta anharmonikoak kontuan hartu ondoren. Efektu hauek kontuan hartzen ez badira, propietate berdinak lortzeko presioa nabarmen igo behar da, presioa igotzeak hidrogeno molekulak luzatzeko joera baitauka ere. Ondorioz, $Cmca-4$ egitura molekularrean efektu anharmonikoek tenperatura altuko supereroankortasuna lortzeko beharrezko presioa txikitzen dutela esan daiteke.

Zortzigarren kapituluan aurreko bi kapituluetan aztertutako egituren propietate optikoak aztertu ditugu, hidrogeno metalikoaren karakterizazioan laguntzeko asmoz. Horretarako, bi fase hauek IR-tik ultramore (UV) espektrorainoko erradiazioa nola islatuko duten kalkulatu dugu TDDFT eta Eliashberg formalismoa konbinatuz. Gure emaitzen arabera, $I4_1/amd$ egituraren islapena elektroi-fonoi elkarrekintzak gobernatzen du Dias eta Silveraren esperimentuak buruturiko argi maiztasunetan. Guk kalkulatutako elektroien sakabanatze balioak bateragarriak dira esperimentuetan neurtutakoekin. Bestalde infragorrian tarte debekatu supereroalearen presentzia nabarmena da 120 meV inguruan. Honez gain, ultramorean elektroi askeen ohiko plasmoiaz gain 35 eV inguruan, beste plasmoi bat ere topatu

dugu 6 eV inguruan, interbanda izaera duena eta beste metal alkalino batzuetan eta zenbait hidrurotan ere agertzen dena Bestalde, $Cmca-4$ egituran oso emaitza ezberdinak lortu ditugu, batez ere argi ikuskor eta ultramorean. Bertan, elektroien energia baxuko kitzikapen prozesuek islapena nabarmen murrizten dute 1 eV-tik gora. Ondorioz, islapen esperimentuen bidez bi egitura hauek bereiztea posible litzateke. Dias eta Silveraren emaitzekin hobeto bat datozen kalkuluak $I4_1/amd$ egiturarenak dira, esperimentuan datu nahikoa bildu ez badute ere ondorio zehatzik ateratzeko. Edozein modutan, gure emaitzek esperimentu gehiago egitera bultzatzea espero dugu, neurtutakoa berretsi eta infragorri eta ultramorean iragarritako ezaugarriak bilatzeko.

Hirugarren atala, *Lithium* izenekoa, litioaren analisiari eskaini diogu. Duela urte gutxi batzuk Schaeffer eta egilekideek litioan supereroankortasun isotopo efektu anomaloa neurtu zuten 15-25 GPa tartean [9]. BCS (Bardeen Cooper Schrieffer) teoriaren eta eredu harmonikoaren arabera, elementu supereroale bateko T_c-ak isotopoen masaren arabera $\propto 1/M^\alpha$ bezala eskalatu beharko luke, $\alpha = 0.5$ izanik. Azken esperimentu honetan, ordea, ^{6}Li eta ^{7}Li-ren T_c-ak neurtu eta gero, 0.5 baliotik oso urrun dauden α balioak lortu dituzte, 21 GPa-tik gora α-k balio negatiboak hartzeraino. Anomalia hau azaltzeko, bi hipotesi planteatu ditugu. Lehenengoa, efektu anharmonikoen ondorioz fonoi maiztasunek ez dutela ohiko $\propto 1/M^{0.5}$ modu harmonikoan eskalatzen, eta ondorioz, λ elektroi-fonoi koefizienteak masarekiko menpekotasuna duela. Bigarrena, bi isotopoek kristal egitura ezberdina dutela eta, ondorioz, propietate ezberdinak. Lehenengo hipotesiaren oinarria fcc egiturak, esperimentuan neurturiko presioetan esperotakoa, hurbilketa harmonikoan egiten kalkuluetan agertzen duen fonoi biguna da, agian efektu anharmoniko bortitzak agertzen dituena [10, 27, 28, 205, 206]. Bigarren hipotesia planteatzeko arrazoiak, alde batetik, aurreko kalkulu batzuen araberako kristal egituren arteko entalpia diferentzia txikiak dira [17, 209, 210]. Bestetik, presio eta tenperatura baxuetako esperimentuetan agertutako meta-egonkortasunak dira, litioaren isotopo bien fase diagrama ezberdina izanik [203].

Bederatzigarren kapituluan fcc egituraren $\mathbf{q}_{inst} = 2\pi/a(2/3, 2/3, 0)$ puntuko modu biguna aztertu dugu. Konkretuki, ^{7}Li-an efektu anharmonikoen ondoriozko fonoi maiztasunaren zuzenketa kalkulatu dugu 26 GPa-tan. Horretako, atomoak modu normal anomaloaren arabera desplazatu, energia profila kalkulatu eta ondoren Schrödinger ekuazioa ebatzi dugu. Eredu harmonikoaren arabera, oreka posizioko energiaren bigarren deribatua numerikoki kalkulatuz, -28.6 cm^{-1}-ko maiztasuna lortu dugun bitartean, efektu anharmonikoek 115.3 cm^{-1}-ra igotzen dute maiztasuna. Maiztasuna negatibotik (irudikaria, izatez) positibora pasatzen denez, badirudi efektu anharmonikoek egonkortzen dutela litioa presio honetan. Efektu anharmonikoak, hortaz, oso handiak dira fcc litioan. Modu anomalo honek

ekarpen handia daukanez supereroankortasunean, baliteke efektu anharmonikoek eragin handia izatea ere propietate honetan.

Bukatzeko, hamargarren kapituluan litioan neurtutako supereroankortasun isotopo efektu anomaloaren arrazoiak bilatzen saiatu gara. Alde batetik, lehenengo hipotesia, hots, isotopo efektua fcc egituran efektu anharmonikoen ondorioz agertzen den, konprobatu dugu, horretarako SSCHA erabiliz. Gure emaitzen arabera, efektu anharmonikoen eragina fonoi anomaloan oso nabaria bada ere, bere maiztasunak eredu harmonikoaren arabera eskalatzen du masarekin. Hortaz, λ-k ez du apenas bere balioa aldatzen isotopo batetik bestera eta T_c-k isotopo efektu arrunta agertzen du. Beste aldetik, bigarren hipotesia konprobatu dugu, hau da, bi isotopoek kristal egitura ezberdina izatearen ondorioz gertatzen den isotopo efektuaren anomalia. Horretarako 10-50 GPa inguruan hiru fase lehiakorrenen entalpia kalkulatu dugu (fcc, $cI16$ eta $hR1$ egiturak), bibrazioen energia SSCHA-rekin kontuan hartuz. Gure emaitzen arabera ez da espero bi isotopoek egoera egonkorrean kristal egitura ezberdina izatea. Hala ere, ezin dira meta-egonkortasunak baztertu, entalpia ezberdintasunak meV gutxi batzuetakoak baitira. Meta-egonkortasunak posible balira, esperimentuetako emaitzak kualitatiboki azalduko lirateke ^{6}Li-k $cI16$ egitura eta ^{7}Li-k fcc egitura balute. Edozein modutan, esperimentuetako erroreak handiak dira eta, askotan, presio oso antzekoetarako T_c oso ezberdinak lortzen dituzte. Ondorioz, esperimentuen fidagarritasuna zalantzan jartzen du gure lanak. Hortaz, esperimentuak berriz burutzeko gomendatzen dugu, emaitzak berresteko eta egituren karakterizazio zehatza egiteko.

List of Publications

List of Publications

Part of the work presented here has been published in the following references:

1. *Anharmonic effects in atomic hydrogen: Superconductivity and lattice dynamical stability,*
   Miguel Borinaga, Ion Errea, Matteo Calandra, Francesco Mauri and Aitor Bergara,
   Physical Review B 93 174308 (2016)

2. *Anharmonic enhancement of superconductivity in metallic molecular Cmca-4 hydrogen at high pressure: A first-principles study,*
   Miguel Borinaga, Patricia Riego, Aritz Leonardo, Matteo Calandra, Francesco Mauri, Aitor Bergara and Ion Errea,
   Journal of Physics Condensed Matter 28(49) 494001 (2016)

3. *Dynamical stability of face centered cubic lithium at 25 GPa,*
   Miguel Borinaga, Unai Aseginolaza, Ion Errea and Aitor Bergara,
   JJAP Conference Proceedings 6 011103 (2017)

4. *Anharmonicity and the isotope effect in superconducting lithium at high pressures: A first-principles approach,*
   Miguel Borinaga, Unai Aseginolaza, Ion Errea, Matteo Calandra, Francesco Mauri and Aitor Bergara,
   Physical Review B 96 184505 (2017)

5. *Strong Electron-Phonon and Band Structure Effects in the Optical Properties of High Pressure Metallic Hydrogen,*
   Miguel Borinaga, Julen Ibañez-Azpiroz, Aitor Bergara and Ion Errea,
   Physical Review Letters 120 057402 (2018)

Acknowledgements

Acknowledgements

I have always wanted a job that let me keep learning interesting things while getting paid for it. Working for almost four years in my Ph.D. thesis has more than satisfied my needs and, of course, I can only be grateful for it. That is why now, when I am closing this stage of my life, I feel the need to look backwards and thank all the people that made this possible.

First of all, I would like to thank Aitor Bergara for many reasons. First, for showing me the beauty of quantum and condensed matter physics during my bachelor studies in Leioa and, then, for giving me the chance to do my Bachelor's thesis with him. That Bachelor's thesis lead to a Master's thesis and, finally, to this Ph.D. thesis. Here, I would also like to thank Ion Errea, since he has been my co-supervisor in both the Master's and Ph.D. theses. Needless to say that it has been an absolute pleasure to be directed by both of you. You really are great role models to follow. I hope you have learned with me at least a small portion of all that I have learned from and with you.

I would like to acknowledge my current institute Centro de Física de Materiales and all the people working in it. I would also like to thank the Donostia International Physics Center (DIPC) and its computing center service, as most of the computational work presented in this thesis was done on the DIPC supercomputers. I also want to thank HPSTAR Shanghai and Duckyoung Kim for giving me the opportunity to stay three months with them in an outstanding research environment.

As many of my friends and my family did not fully understand how this "getting paid for studying" worked, I had to convince them that I was an actual worker, with an actual salary. Thus, I have to acknowledge that I have been financially supported with a Predoctoral Grant (PRE-2017-2-0236) from the the Department of Education of the Basque Government. Thank you very much to them as well.

I cannot forget about all the friends I have made during my almost five years at the CFM. They will clearly help in retaining a good memory from my Ph.D. student

time in the years to come. The list of people is too long to write it entirely but, knowing I will miss important people, I will try to write a few of them: Unai, Jose, Moritz, Fede, Marc, Pedro, Mads, Nestor, Iker, Julen, Gari, Alvaro, Antton, Mikel, Tineke, Tomaš (two of them), Alba, Dario, Mikołai, Berni, Andrea, Nieves, Donaldi, Dino, Ivor... They have been either officemates at some point during these five years or part of any of the coffee break/lunch/pintxopote/pizzapote/padel groups, where we talked even about physics. Thanks to all of you on the list and also to the ones that are not but should be there as well.

Finally, I would like to thank all my friends and family from Soraluze. Koadrilakoei, asteburuetan deskonektatzen laguntzeagatik, soziedadeko afariengatik eta noizean behin "nanomobidena" zermoduz zihoan galdetzeagatik. Familiakoei, txiki-txikitatik nire jakinmina asetzen lagundu eta beti gauzen zergatia jakiteko nahia izatera motibatzeagatik. Eta zuri, Ainhoa, azken urte guzti hauetan nirekin pasatako denbora ordainezinagatik momentu onetan eta, batez ere, txarretan. Konturatu barik elkarrekin egin gara heldu eta bagara biok doktore, ezberdinak bada ere.

Bibliography

[1] G. Ernst, C. Artner, O. Blaschko, and G. Krexner, Phys. Rev. B **33**, 6465 (1986).

[2] J. L. Olsen, E. Bucher, M. Levy, J. Muller, E. Corenzwit, and T. Geballe, Rev. Mod. Phys. **36**, 168 (1964).

[3] R. E. Hodder, Phys. Rev. **180**, 530 (1969).

[4] T. F. Smith and C. W. Chu, Phys. Rev. **159**, 353 (1967).

[5] M. Levy and J. Olsen, Solid State Communications **2**, 137 (1964).

[6] J. Tuoriniemi, K. Juntunen-Nurmilaukas, J. Uusvuori, E. Pentti, A. Salmela, and A. Sebedash, Nature **447**, 187 (2007).

[7] S. Deemyad and J. S. Schilling, Phys. Rev. Lett. **91**, 167001 (2003).

[8] V. V. Struzhkin, M. I. Eremets, W. Gan, H.-k. Mao, and R. J. Hemley, Science **298**, 1213 (2002).

[9] A. M. Schaeffer, S. R. Temple, J. K. Bishop, and S. Deemyad, Proceedings of the National Academy of Sciences **112**, 60 (2015).

[10] T. Bazhirov, J. Noffsinger, and M. L. Cohen, Phys. Rev. B **82**, 184509 (2010).

[11] K. Shimizu, H. Ishikawa, D. Takao, T. Yagi, and K. Amaya, Nature **419**, 597 (2002).

[12] N. W. Ashcroft, Nature **419**, 569 (2002).

[13] B. Lorenz and C. Chu, "High pressure effects on superconductivity," in *Frontiers in Superconducting Materials*, edited by A. V. Narlikar (Springer Berlin Heidelberg, Berlin, Heidelberg, 2005) pp. 459–497.

[14] E. Wigner and H. B. Huntington, The Journal of Chemical Physics **3**, 764 (1935).

[15] N. W. Ashcroft, Phys. Rev. Lett. **21**, 1748 (1968).

[16] A. P. Drozdov, M. I. Eremets, I. A. Troyan, V. Ksenofontov, and S. I. Shylin, Nature **525**, 73 (2015).

[17] M. Hanfland, K. Syassen, N. E. Christensen, and D. L. Novikov, Nature **408**, 174 (2000).

[18] E. Gregoryanz, L. F. Lundegaard, M. I. McMahon, C. Guillaume, R. J. Nelmes, and M. Mezouar, Science **320**, 1054 (2008).

[19] H. Olijnyk and W. B. Holzapfel, Phys. Lett. A **100**, 191 (1984).

[20] T. Yabuuchi, Y. Nakamoto, K. Shimizu, and T. Kikegawa, J. Phys. Soc. Jpn. **74**, 2391 (2005).

[21] H. Fujihisa, Y. Nakamoto, K. Shimizu, T. Yabuuchi, and Y. Gotoh, Phys. Rev. Lett. **101**, 095503 (2008).

[22] Y. Nakamoto, M. Sakata, K. Shimizu, H. Fujihisa, T. Matsuoka, Y. Ohishi, and T. Kikegawa, Phys. Rev. B **81**, 140106 (2010).

[23] T. Matsuoka and K. Shimizu, Nature **458**, 186 (2009).

[24] Y. Ma, M. I. Eremets, A. R. Oganov, Y. Xie, I. Trojan, S. Medvedev, A. O. Lyakhov, M. Valle, and V. Prakapenka, Nature **458**, 182 (2009).

[25] E. Gregoryanz, O. Degtyareva, M. Somayazulu, R. J. Hemley, and H.-k. Mao, Phys. Rev. Lett. **94**, 185502 (2005).

[26] C. L. Guillaume, E. Gregoryanz, O. Degtyareva, M. I. McMahon, M. Hanfland, S. Evans, M. Guthrie, S. V. Sinogeikin, and H.-K. Mao, Nature Physics **7**, 211 (2011).

[27] G. Profeta, C. Franchini, N. N. Lathiotakis, A. Floris, A. Sanna, M. A. L. Marques, M. Lüders, S. Massidda, E. K. U. Gross, and A. Continenza, Phys. Rev. Lett. **96**, 047003 (2006).

[28] A. Rodriguez-Prieto, A. Bergara, V. M. Silkin, and P. M. Echenique, Phys. Rev. B **74**, 172104 (2006).

[29] I. Loa, M. I. McMahon, and A. Bosak, Phys. Rev. Lett. **102**, 035501 (2009).

[30] F. Mauri, O. Zakharov, S. de Gironcoli, S. G. Louie, and M. L. Cohen, Phys. Rev. Lett. **77**, 1151 (1996).

[31] O. Degtyareva, M. V. Magnitskaya, J. Kohanoff, G. Profeta, S. Scandolo, M. Hanfland, M. I. McMahon, and E. Gregoryanz, Phys. Rev. Lett. **99**, 155505 (2007).

[32] Z. P. Yin, S. Y. Savrasov, and W. E. Pickett, Phys. Rev. B **74**, 094519 (2006).

[33] B. Rousseau, Y. Xie, Y. Ma, and A. Bergara, Eur. Phys. J. B **81**, 1 (2011).

[34] L. Dubrovinsky, N. Dubrovinskaia, V. B. Prakapenka, and A. M. Abakumov, Nat Commun **3**, 1163 (2012).

[35] B. Winkler and V. Milman, Zeitschrift für Kristallographie – Crystalline Materials **229**, 112 (2014).

[36] H.-K. Mao, B. Chen, J. Chen, K. Li, J.-F. Lin, W. Yang, and H. Zheng, Matter and Radiation at Extremes **1**, 59 (2016).

[37] M. J. Gillan, D. Alfè, J. Brodholt, L. Vočadlo, and G. D. Price, Reports on Progress in Physics **69**, 2365 (2006).

[38] Y. Li, J. Hao, H. Liu, Y. Li, and Y. Ma, The Journal of Chemical Physics **140**, 174712 (2014).

[39] D. Duan, Y. Liu, F. Tian, D. Li, X. Huang, Z. Zhao, H. Yu, B. Liu, W. Tian, and T. Cui, Scientific Reports **4**, 6968 (2015).

[40] J. C. Slater, Phys. Rev. **35**, 210 (1930).

[41] P. Hohenberg and W. Kohn, Phys. Rev. **136**, B864 (1964).

[42] W. Kohn and L. J. Sham, Phys. Rev. **140**, A1133 (1965).

[43] D. M. Ceperley and B. J. Alder, Phys. Rev. Lett. **45**, 566 (1980).

[44] S. Lehtola, C. Steigemann, M. J. Oliveira, and M. A. Marques, SoftwareX **7**, 1 (2018).

[45] J. P. Perdew, K. Burke, and M. Ernzerhof, Phys. Rev. Lett. **77**, 3865 (1996).

[46] C. Lee, W. Yang, and R. G. Parr, Phys. Rev. B **37**, 785 (1988).

[47] M. C. Payne, M. P. Teter, D. C. Allan, T. A. Arias, and J. D. Joannopoulos, Rev. Mod. Phys. **64**, 1045 (1992).

[48] N. W. Ashcroft and N. D. Mermin, *Solid State Physics* (Thomson Learning Inc., 1976).

[49] E. Wigner, Trans. Faraday Soc. **34**, 678 (1938).

[50] L. Hedin and B. I. Lundqvist, J. Phys. C: Solid State Phys. **4**, 2064 (1971).

[51] S. H. Vosko, L. Wilk, and M. Nusair, Can. J. Phys. **58**, 1200 (1980).

[52] J. P. Perdew and A. Zunger, Phys. Rev. B **23**, 5048 (1981).

[53] J. P. Perdew and Y. Wang, Phys. Rev. B **45**, 13244 (1992).

[54] J. P. Perdew, K. Burke, and Y. Wang, Phys. Rev. B **54**, 16533 (1996).

[55] M. Gell-Mann and K. A. Brueckner, Phys. Rev. **106**, 364 (1957).

[56] F. Herman, J. P. Van Dyke, and I. B. Ortenburger, Phys. Rev. Lett. **22**, 807 (1969).

[57] R. M. Martin, *Electronic structure: basic theory and practical methods* (Cambridge University Press, 2004).

[58] D. R. Hamann, M. Schlüter, and C. Chiang, Phys. Rev. Lett. **43**, 1494 (1979).

[59] N. Troullier and J. L. Martins, Phys. Rev. B **43**, 1993 (1991).

[60] D. Vanderbilt, Phys. Rev. B **41**, 7892 (1990).

[61] P. Giannozzi *et al.*, J. Phys. Condens. Matter **21**, 395502 (2009).

[62] H. J. Monkhorst and J. D. Pack, Phys. Rev. B **13**, 5188 (1976).

[63] M. Methfessel and A. T. Paxton, Phys. Rev. B **40**, 3616 (1989).

[64] P. Brüesch, *Phonons: Theory and Experiments I: Lattice Dynamics and Models of Interatomic Forces* (Springer-Verlag, 1982).

[65] G. D. Mahan, *Many-Particle Physics* (Springer, 2000).

[66] M. Born and K. Huang, *Dynamical Theory of Crystal Lattices* (Oxford University Press, Oxford, 1954).

[67] H. Hellmann, *Einfürung in die Quantumchemie* (Deuticke, 1937).

[68] R. P. Feynman, Phys. Rev. **56**, 340 (1939).

[69] R. M. Pick, M. H. Cohen, and R. M. Martin, Phys. Rev. B **1**, 910 (1970).

[70] A. G. Eguiluz and A. A. Quong, in *Phonon Physics The Cutting Edge*, Dynamical Properties of Solids, Vol. 7, edited by G. Horton and A. Maradudin (North-Holland, 1995) pp. 425 – 507.

[71] D. Pines and P. Nozières, *The Theory of Quantum Liquids*, Vol. 1 (Benjamin, New York, 1966).

[72] A. A. Quong, A. A. Maradudin, R. F. Wallis, J. A. Gaspar, A. G. Eguiluz, and G. P. Alldredge, Phys. Rev. Lett. **66**, 743 (1991).

[73] A. A. Quong and B. M. Klein, Phys. Rev. B **46**, 10734 (1992).

[74] R. F. Wallis, A. A. Maradudin, V. Bortolani, A. G. Eguiluz, A. A. Quong, A. Franchini, and G. Santoro, Phys. Rev. B **48**, 6043 (1993).

[75] A. A. Quong, Phys. Rev. B **49**, 3226 (1994).

[76] M. Calandra, G. Profeta, and F. Mauri, Phys. Rev. B **82**, 165111 (2010).

[77] B. Rousseau, I. Errea, and A. Bergara, Journal of Physics and Chemistry of Solids **71**, 1159 (2010).

[78] K. Nagao, S. A. Bonev, A. Bergara, and N. W. Ashcroft, Phys. Rev. Lett. **90**, 035501 (2003).

[79] S. Baroni, P. Giannozzi, and A. Testa, Phys. Rev. Lett. **58**, 1861 (1987).

[80] X. Gonze, Phys. Rev. A **52**, 1096 (1995).

[81] S. Baroni, S. de Gironcoli, A. Dal Corso, and P. Giannozzi, Rev. Mod. Phys. **73**, 515 (2001).

[82] R. M. Sternheimer, Phys. Rev. **96**, 951 (1954).

[83] E. A. Hylleraas, Zeitschrift für Physik **65**, 209 (1930).

[84] O. Hellman, P. Steneteg, I. A. Abrikosov, and S. I. Simak, Phys. Rev. B **87**, 104111 (2013).

[85] O. Hellman and I. A. Abrikosov, Phys. Rev. B **88**, 144301 (2013).

[86] O. Hellman, I. A. Abrikosov, and S. I. Simak, Phys. Rev. B **84**, 180301 (2011).

[87] M. P. Ljungberg and J. Íñiguez, Phys. Rev. Lett. **110**, 105503 (2013).

[88] I. B. Magdau and G. J. Ackland, Phys. Rev. B **87**, 174110 (2013).

[89] C. Z. Wang, C. T. Chan, and K. M. Ho, Phys. Rev. B **42**, 11276 (1990).

[90] D.-B. Zhang, T. Sun, and R. M. Wentzcovitch, Phys. Rev. Lett. **112**, 058501 (2014).

[91] N. de Koker, Phys. Rev. Lett. **103**, 125902 (2009).

[92] D. M. Ceperley, Rev. Mod. Phys. **67**, 279 (1995).

[93] I. Errea, M. Calandra, and F. Mauri, Phys. Rev. B **89**, 064302 (2014).

[94] I. Errea, M. Calandra, and F. Mauri, Phys. Rev. Lett. **111**, 177002 (2013).

[95] I. Errea, B. Rousseau, and A. Bergara, Phys. Rev. Lett. **106**, 165501 (2011).

[96] B. Monserrat, N. D. Drummond, and R. J. Needs, Phys. Rev. B **87**, 144302 (2013).

[97] T. Tadano and S. Tsuneyuki, Phys. Rev. B **92**, 054301 (2015).

[98] I. Georgescu and V. A. Mandelshtam, The Journal of Chemical Physics **137**, 144106 (2012).

[99] S. E. Brown, I. Georgescu, and V. A. Mandelshtam, The Journal of Chemical Physics **138**, 044317 (2013).

[100] C. E. Patrick, K. W. Jacobsen, and K. S. Thygesen, Phys. Rev. B **92**, 201205 (2015).

[101] D. Hooton, Philosophical Magazine Series 7 **46**, 422 (1955).

[102] I. Errea, M. Calandra, C. J. Pickard, J. Nelson, R. J. Needs, Y. Li, H. Liu, Y. Zhang, Y. Ma, and F. Mauri, Phys. Rev. Lett. **114**, 157004 (2015).

[103] I. Errea, M. Calandra, C. J. Pickard, J. R. Nelson, R. J. Needs, Y. Li, H. Liu, Y. Zhang, Y. Ma, and F. Mauri, Nature **532**, 81 (2016).

[104] M. Leroux, I. Errea, M. Le Tacon, S.-M. Souliou, G. Garbarino, L. Cario, A. Bosak, F. Mauri, M. Calandra, and P. Rodière, Phys. Rev. B **92**, 140303 (2015).

[105] G. A. S. Ribeiro, L. Paulatto, R. Bianco, I. Errea, F. Mauri, and M. Calandra, Phys. Rev. B **97**, 014306 (2018).

[106] A. L. Fetter and J. D. Walecka, *Quantum theory of many-particle systems* (McGraw-Hill, 1971).

[107] A. B. Migdal, Sov. Phys. JETP **7**, 996 (1958).

[108] G. M. Eliashberg, Sov. Phys. JETP **11**, 696 (1960).

[109] P. B. Allen and B. Mitrovic, "Solid state physics," (Academic, New York, 1982) pp. 1–92.

[110] J. Bardeen, L. N. Cooper, and J. R. Schrieffer, Phys. Rev. **108**, 1175 (1957).

[111] Y. Nambu, Phys. Rev. **117**, 648 (1960).

[112] P. Anderson, Journal of Physics and Chemistry of Solids **11**, 26 (1959).

[113] J. P. Carbotte, Rev. Mod. Phys. **62**, 1027 (1990).

[114] W. L. McMillan, Phys. Rev. **167**, 331 (1968).

[115] R. Dynes, Solid State Communications **10**, 615 (1972).

[116] J. Kortus, I. I. Mazin, K. D. Belashchenko, V. P. Antropov, and L. L. Boyer, Phys. Rev. Lett. **86**, 4656 (2001).

[117] M. Calandra and F. Mauri, Phys. Rev. Lett. **95**, 237002 (2005).

[118] E. Runge and E. K. U. Gross, Phys. Rev. Lett. **52**, 997 (1984).

[119] M. Petersilka, U. J. Gossmann, and E. K. U. Gross, Phys. Rev. Lett. **76**, 1212 (1996).

[120] R. van Leeuwen, Phys. Rev. Lett. **82**, 3863 (1999).

[121] S. L. Adler, Phys. Rev. **126**, 413 (1962).

[122] W. M. Saslow and G. F. Reiter, Phys. Rev. B **7**, 2995 (1973).

[123] G. Onida, L. Reining, and A. Rubio, Rev. Mod. Phys. **74**, 601 (2002).

[124] V. I. Gavrilenko and F. Bechstedt, Phys. Rev. B **54**, 13416 (1996).

[125] J. Dewar, Ann. Chim. Phys. **18**, 145 (1899).

[126] M. I. Eremets and I. A. Troyan, Nat Mater **10**, 927 (2011).

[127] P. Loubeyre, R. LeToullec, D. Hausermann, M. Hanfland, R. J. Hemley, H. K. Mao, and L. W. Finger, Nature **383**, 702 (1996).

[128] S. Deemyad and I. F. Silvera, Phys. Rev. Lett. **100**, 155701 (2008).

[129] A. B. Stanimir, E. Schwegler, T. Ogitsu, and G. Galli, Nature **431**, 669 (2004).

[130] H.-k. Mao and R. J. Hemley, Rev. Mod. Phys. **66**, 671 (1994).

[131] C.-S. Zha, Z. Liu, and R. J. Hemley, Phys. Rev. Lett. **108**, 146402 (2012).

[132] A. F. Goncharov, E. Gregoryanz, R. J. Hemley, and H.-k. Mao, Proceedings of the National Academy of Sciences **98**, 14234 (2001).

[133] R. T. Howie, C. L. Guillaume, T. Scheler, A. F. Goncharov, and E. Gregoryanz, Phys. Rev. Lett. **108**, 125501 (2012).

[134] C.-s. Zha, Z. Liu, M. Ahart, R. Boehler, and R. J. Hemley, Phys. Rev. Lett. **110**, 217402 (2013).

[135] R. T. Howie, P. Dalladay-Simpson, and E. Gregoryanz, Nat Mater **14**, 495 (2015).

[136] P. Loubeyre, F. Occelli, and R. LeToullec, Nature **416**, 613 (2002).

[137] P. Dalladay-Simpson, R. T. Howie, and E. Gregoryanz, Nature **529**, 63 (2016).

[138] R. P. Dias and I. F. Silvera, Science **355**, 715 (2017).

[139] D. Saumon and G. Chabrier, Phys. Rev. Lett. **62**, 2397 (1989).

[140] S. Scandolo, Proceedings of the National Academy of Sciences **100**, 3051 (2003).

[141] W. Lorenzen, B. Holst, and R. Redmer, Phys. Rev. B **82**, 195107 (2010).

[142] M. A. Morales, J. M. McMahon, C. Pierleoni, and D. M. Ceperley, Phys. Rev. Lett. **110**, 065702 (2013).

[143] M. Zaghoo, A. Salamat, and I. F. Silvera, Phys. Rev. B **93**, 155128 (2016).

[144] V. Dzyabura, M. Zaghoo, and I. F. Silvera, Proceedings of the National Academy of Sciences **110**, 8040 (2013).

[145] S. T. Weir, A. C. Mitchell, and W. J. Nellis, Phys. Rev. Lett. **76**, 1860 (1996).

[146] V. E. Fortov, R. I. Ilkaev, V. A. Arinin, V. V. Burtzev, V. A. Golubev, I. L. Iosilevskiy, V. V. Khrustalev, A. L. Mikhailov, M. A. Mochalov, V. Y. Ternovoi, and M. V. Zhernokletov, Phys. Rev. Lett. **99**, 185001 (2007).

[147] P. Cudazzo, G. Profeta, A. Sanna, A. Floris, A. Continenza, S. Massidda, and E. K. U. Gross, Phys. Rev. Lett. **100**, 257001 (2008).

[148] J. M. McMahon and D. M. Ceperley, Phys. Rev. B **84**, 144515 (2011).

[149] Y. Yan, J. Gong, and Y. Liu, Physics Letters A **375**, 1264 (2011).

[150] E. Maksimov and D. Savrasov, Solid State Communications **119**, 569 (2001).

[151] N. W. Ashcroft, Phys. Rev. Lett. **92**, 187002 (2004).

[152] N. W. Ashcroft, Journal of Physics A: Mathematical and General **36**, 6137 (2003).

[153] S. A. Bonev and N. W. Ashcroft, Phys. Rev. B **64**, 224112 (2001).

[154] L. Zhang, Y. Niu, Q. Li, T. Cui, Y. Wang, Y. Ma, Z. He, and G. Zou, Solid State Communications **141**, 610 (2007).

[155] P. Cudazzo, G. Profeta, A. Sanna, A. Floris, A. Continenza, S. Massidda, and E. K. U. Gross, Phys. Rev. B **81**, 134505 (2010).

[156] P. Cudazzo, G. Profeta, A. Sanna, A. Floris, A. Continenza, S. Massidda, and E. K. U. Gross, Phys. Rev. B **81**, 134506 (2010).

[157] B. Rousseau and A. Bergara, High Pressure Research **31**, 30 (2011).

[158] B. Rousseau and A. Bergara, Phys. Rev. B **82**, 104504 (2010).

[159] I. Goncharenko and P. Loubeyre, Nature **435**, 1206 (2005).

[160] C. J. Pickard and R. J. Needs, Nat. Phys. **3**, 473 (2007).

[161] C. J. Pickard, M. Martinez-Canales, and R. J. Needs, Phys. Rev. B **85**, 214114 (2012).

[162] M. I. Eremets, I. A. Troyan, and A. P. Drozdov, (2016), arXiv:1601.04479 .

[163] M. I. Eremets, A. Drozdov, P. Kong, and H. Wang, (2017), arXiv:1708.05217 .

[164] R. P. Dias, O. Noked, and I. F. Silvera, (2016), arXiv:1603.02162 .

[165] M. I. Eremets and A. P. Drozdov, (2017), arXiv:1702.05125 .

[166] P. Loubeyre, F. Occelli, and P. Dumas, (2017), arXiv:1702.07192 .

[167] X.-D. Liu, P. Dalladay-Simpson, R. T. Howie, B. Li, and E. Gregoryanz, (2017), arXiv:1704.07601 .

[168] A. F. Goncharov and V. V. Struzhkin, (2017), arXiv:1702.04246 .

[169] S. Azadi, B. Monserrat, W. M. C. Foulkes, and R. J. Needs, Phys. Rev. Lett. **112**, 165501 (2014).

[170] J. M. McMahon and D. M. Ceperley, Phys. Rev. Lett. **106**, 165302 (2011).

[171] C.-s. Zha, H. Liu, J. S. Tse, and R. J. Hemley, Phys. Rev. Lett. **119**, 075302 (2017).

[172] P. B. Allen and R. C. Dynes, Phys. Rev. B **12**, 905 (1975).

[173] C. Bowen, G. Sugiyama, and B. J. Alder, Phys. Rev. B **50**, 14838 (1994).

[174] S. Azadi and W. M. C. Foulkes, Phys. Rev. B **88**, 014115 (2013).

[175] C. A. Burns and E. D. Isaacs, Phys. Rev. B **55**, 5767 (1997).

[176] W. Heitler and F. London, Zeitschrift für Physik **44**, 455 (1927).

[177] B. Monserrat and R. J. Needs, Phys. Rev. B **89**, 214304 (2014).

[178] F. Giustino, S. G. Louie, and M. L. Cohen, Phys. Rev. Lett. **105**, 265501 (2010).

[179] X. Gonze, P. Boulanger, and M. Côté, Annalen der Physik **523**, 168 (2011).

[180] W. J. Nellis, A. L. Ruoff, and I. F. Silvera, , 1 (2012), arXiv:1201.0407 .

[181] I. Amato, Nature **486**, 174 (2012).

[182] I. Silvera and R. Dias, (2017), arXiv:1703.03064 .

[183] B. Rousseau, A. Eiguren, and A. Bergara, Phys. Rev. B **85**, 054305 (2012).

[184] I. Errea, B. Rousseau, A. Eiguren, and A. Bergara, Phys. Rev. B **86**, 085106 (2012).

[185] J. Ibañez-Azpiroz, B. Rousseau, A. Eiguren, and A. Bergara, Phys. Rev. B **89**, 085102 (2014).

[186] N. Marzari and D. Vanderbilt, Phys. Rev. B **56**, 12847 (1997).

[187] N. Marzari, A. A. Mostofi, J. R. Yates, I. Souza, and D. Vanderbilt, Rev. Mod. Phys. **84**, 1419 (2012).

[188] Z. Schlesinger, R. T. Collins, D. L. Kaiser, and F. Holtzberg, Phys. Rev. Lett. **59**, 1958 (1987).

[189] L. D. Rotter, Z. Schlesinger, J. P. McCauley, N. Coustel, J. E. Fischer, and A. B. Smith, Nature **355**, 532 (1992).

[190] F. Capitani, B. Langerome, J.-B. Brubach, P. Roy, A. Drozdov, M. I. Eremets, E. J. Nicol, J. P. Carbotte, and T. Timusk, Nature Physics **13**, 859 (2017).

[191] N. E. Bickers, D. J. Scalapino, R. T. Collins, and Z. Schlesinger, Phys. Rev. B **42**, 67 (1990).

[192] H. J. Vidberg and J. W. Serene, Journal of Low Temperature Physics **29**, 179 (1977).

[193] A. A. Mostofi, J. R. Yates, G. Pizzi, Y.-S. Lee, I. Souza, D. Vanderbilt, and N. Marzari, Computer Physics Communications **185**, 2309 (2014).

[194] V. M. Silkin, A. Rodriguez-Prieto, A. Bergara, E. V. Chulkov, and P. M. Echenique, Phys. Rev. B **75**, 172102 (2007).

[195] A. Rodriguez-Prieto, V. M. Silkin, A. Bergara, and P. M. Echenique, New J. Phys. **10**, 053035 (2008).

[196] I. Errea, A. Rodriguez-Prieto, B. Rousseau, V. M. Silkin, and A. Bergara, Phys. Rev. B **81**, 205105 (2010).

[197] H.-K. Mao, Y. Ding, Y. Xiao, P. Chow, J. Shu, S. Lebègue, A. Lazicki, and R. Ahuja, Proc. Natl. Acad. Sci. USA **108**, 20434 (2011).

[198] N. V. Smith, Phys. Rev. B **2**, 2840 (1970).

[199] I. G. Gurtubay, B. Rousseau, and A. Bergara, Phys. Rev. B **82**, 085113 (2010).

[200] F. Seitz, Physical Review **47**, 400 (1935).

[201] T. Matsuoka, S. Onoda, M. Kaneshige, Y. Nakamoto, K. Shimizu, T. Kagayama, and Y. Ohishi, Journal of Physics: Conference Series **121**, 052003 (2008).

[202] A. M. Schaeffer, W. Cai, E. Olejnik, J. J. Molaison, S. Sinogeikin, A. M. dos Santos, and S. Deemyad, Nature Communications **6**, 8030 (2015).

[203] G. J. Ackland, M. Dunuwille, M. Martinez-Canales, I. Loa, R. Zhang, S. Sinogeikin, W. Cai, and S. Deemyad, Science **356**, 1254 (2017).

[204] E. R. Hernández, A. Rodriguez-Prieto, A. Bergara, and D. Alfè, Phys. Rev. Lett. **104**, 185701 (2010).

[205] R. Akashi and R. Arita, Phys. Rev. Lett. **111**, 057006 (2013).

[206] S. U. Maheswari, H. Nagara, K. Kusakabe, and N. Suzuki, Journal of the Physical Society of Japan **74**, 3227 (2005).

[207] A. Rodriguez-Prieto and A. Bergara, Phys. Rev. B **72**, 125406 (2005).

[208] I. Errea, B. Rousseau, and A. Bergara, Journal of Applied Physics **111**, 112604 (2012).

[209] Y. Ma, A. R. Oganov, and Y. Xie, Phys. Rev. B **78**, 014102 (2008).

[210] Y. Yao, J. S. Tse, K. Tanaka, F. Marsiglio, and Y. Ma, Phys. Rev. B **79**, 054524 (2009).

[211] W. R. Inc., "Mathematica, Version 10.0," Champaign, IL, 2014.

[212] P. Morel and P. W. Anderson, Phys. Rev. **125**, 1263 (1962).

[213] K. J. Chang, M. M. Dacorogna, M. L. Cohen, J. M. Mignot, G. Chouteau, and G. Martinez, Phys. Rev. Lett. **54**, 2375 (1985).

[214] F. Birch, Phys. Rev. **71**, 809 (1947).

[215] X. Gonze and C. Lee, Phys. Rev. B **55**, 10355 (1997).